University of Nottingham
UK | CHINA | MALAYSIA

The Far-Reaching Impact of Cluster Environments on the Nuclear Activity and Star Formation of Galaxies

Kellie de Vos

Thesis submitted to the University of Nottingham
for the degree of Doctor of Philosophy

I learned a lot, by the end of everything. The past is past, now, but that's... you know, that's okay! It's never really gone completely. The future is always built on the past, even if we won't get to see it. Still, it's um, time for something new, now.

– Riebeck, Outer Wilds

Supervisors:	Prof. Nina Hatch	
	Prof. Michael Merrifield	
Examiners:	Prof. Judith Croston	(The Open University)
	Prof. Simon Dye	(University of Nottingham)
Submitted:	23 January 2025	
Examined:	11 February 2025	
Final version:	TBD	

Image credit: M. Gendron-Marsolais et al.; S. Dagnello, NRAO/AUI/NSF; Sloan Digital Sky Survey.

Contents

Abstract

This thesis presents interlinked studies on radio and optical observational data, with the aim of understanding environmental effects on the star formation and nuclear activity of galaxies. These studies have been facilitated by the recent availability of large, deep radio surveys, enabling detailed investigations of galaxy properties across diverse environments. By combining these datasets with optical observations, this work explores how local and global environmental processes, such as ram pressure, galaxy density, and cluster-centric distance, influence the evolution of galaxies.

In Chapter 3, we investigate where, how, and why star formation quenching begins in the outskirts of galaxy clusters. Using the Low-Frequency Array (LOFAR) Two-metre Sky Survey, we analyse the de-projected radial distribution of star-forming galaxies (SFGs) out to $30R_{500}$, where R_{500} is the radius within which the average cluster density is 500 times the critical density of the Universe. We find that the SFG fraction begins to decline from the field fraction at $10R_{500}$, well beyond the cluster's virial radius. This decline is influenced by both large-scale (cluster-centric distance) and local (nearest-neighbour density) environments. Galaxies in high-density local environments show lower SFG fractions, but for high-mass galaxies – and to a lesser extent, low-mass ones – such environments can also shield SFGs from external quenching mechanisms in cluster outskirts. For galaxies in low-density local environments, quenching due to global environment dominates and acts independent of stellar mass. These results reveal a complex interplay between galaxy mass, local density, and global cluster-centric distance in regulating star formation.

In Chapter 4, we examine how the fraction of LOFAR-identified radio active galactic nuclei (AGN) varies with cluster-centric radius, analysing their projected and de-projected distributions out to $30R_{500}$. The AGN fraction shows distinct trends: a $\sim 25\%$ increase above the field fraction in the outskirts ($\sim 10R_{500}$), a $\sim 20\%$ suppression near $\sim 0.5R_{500}$, and a sharp rise to over three times the field fraction in the cluster core. These regions reveal differences in host galaxy stellar mass and AGN radio luminosity. In the core, AGN preferentially reside in massive galaxies, while regions with higher AGN fractions generally host more luminous radio AGN. These findings highlight a dynamic relationship between environmental mechanisms and intrinsic galaxy properties in driving AGN activity.

In Chapter 5, we investigate the details of the interactions between radio galaxies and both the intracluster medium (ICM) and the intergalactic medium (IGM) by analysing 208 narrow-angle tail (NAT) radio sources detected by the LOFAR Two-metre Sky Survey. Within $7R_{500}$ of the cluster centre, NAT tails show a strongly anisotropic distribution, predominantly bending radially away, consistent with galaxies on inbound orbits. Closer to the cluster core ($< 0.5R_{500}$), we observe an excess of NATs with jets bent toward the centre, suggesting these sources fade after passing pericentre. For NATs with spectroscopic redshifts, this radial alignment persists out to $10R_{500}$, well beyond the virial radius. The presence of aligned NATs at such large distances implies significant deceleration of the inflowing intergalactic medium, sufficient to produce ram pressure capable of bending jets and potentially triggering radio emission.

In Chapter 6, we investigate the presence and effects of ram pressure on star formation outside galaxy clusters, through analysis of Hα emission in galaxies in the cluster Abell 1682 and its surrounding environment. Utilising data we obtained using the Wide Field Camera at the Isaac Newton Telescope, we identify and characterise 39 Hα-emitting sources across a field of view spanning $\sim 7.4 \times 7.4$ Mpc. By comparing the spatial offsets between Hα and i-band emission, we detect a statistically significant preference for enhanced Hα emission on the leading edges of galaxies, consistent with a scenario that suggests enhanced star-formation due to gas compression by ram pressure. Surprisingly, these effects are observed not only in the expected filamentary regions but throughout the cluster outskirts, as far as 7.7 Mpc from the cluster centre. These tentative findings challenge current models of gas density in cluster environments and suggest that the intracluster medium may extend further than previously thought, or that multiple filaments may contribute to the observed effects.

Acknowledgements

Firstly, I would like to thank my supervisors, Nina Hatch and Mike Merrifield. From unprecedented beginnings in the height of Covid-19, to the far reaches of Spanish tropical islands, you've been with me through thick and thin, and I simply could not have done this PhD without you. Mike, thank you for always being patient with my persistent pestering when you were just a corridor away - you were always happy to answer my questions no matter how simple or silly. You taught me that science shouldn't be written in the style of cold, hard facts, and is actually much better understood as a story. I'm certain that my grammar and use of "this" as a noun will be much improved because of you. Nina, thank you for always greeting me with a smile and enthusiasm when I would show up at your office door. Your words of encouragement and support when morale was low were absolutely invaluable, and your sheer determination and success as a woman in STEM have inspired me to become as independent as I am in my research. Truly, thank you, to both of you.

I would also like to thank some of the lovely colleagues in CAPT I've had the honour of working with during my time here. Thank you Phil for your endless and truly incomprehensible tech knowledge, and Ella for being the most organised, kind and helpful administrator I have ever had the pleasure of knowing – if either of you ever leave I'm certain that CAPT will fall apart. To my Inflativerse crew – Amy, Roan, CB, Lizzie, Jimi, Jen and Fiona: you guys are the best and I will always have fond memories of our time shared answering crazy questions from children, training keen new volunteers, and troubleshooting endless dome issues.

To those I had the pleasure of spending 9 months with working at the INT on the gorgeous tropical island of La Palma – Judy, Freya, Ki, Ross and Jacco: thank you for all of the support and words of encouragement during the long nights up the mountain, and for all of the laughter and fun during the trips around the island(s) together. To my hilarious and ridiculous "colleagues" – Jacob, Mick, Roan, Sukhi, Tomáš, CB, Karel, Lizzie, Dan, Matt, Charutha, Shaun, Molly, Sophie and James: thank you for the silly camping trips, ridiculous parties and general encouragement to have fun outside of the PhD. To my main gals – CB, Karel and Lizzie: you three are my rocks, and I don't know what I'd do without you. Thank you for your constant support and love, from chatting about our silly little plots to cosy nights with video games and wine.

To Jacob: my partner in crime, adventure and everything in between. Thank you for your constant patience and support despite my endless silly questions. You've picked me up when I've been at my lowest, and never ceased to look after me with your incredible cooking and surprise sweet treats. You're my best friend, and I will be grateful for you always.

To my family: thank you for your endless encouragement, and for trying your best to understand my research even when you didn't have to. And finally, to my mum: you have been my cheerleader and my inspiration my whole life, and I truly mean it when I say I would be lost without you. You've never failed to be the voice of reason, comfort and support when I need it most, and more than anything you have always encouraged me with unwavering enthusiasm to pursue my dreams. Thank you for everything. I couldn't have done this without you.

Published works

The majority of the material presented in this thesis has already been published in the following three works:

i **de Vos, K.**, Hatch, N., Merrifield, M., Mingo, B., *Clusters' far-reaching influence on narrow-angle tail radio galaxies*, Monthly Notices of the Royal Astronomical Society, Volume 506, Issue 1, Sep 2021, Pages L55-L58.

ii **de Vos, K.**, Merrifield, M., Hatch, N., *Local versus global environment: the suppression of star formation in the vicinity of galaxy clusters*, Monthly Notices of the Royal Astronomical Society, Volume 531, Issue 4 , Jul 2024, Pages 4383-4390.

iii **de Vos, K.**, Hatch, N., Merrifield, M., *From outskirts to core: the suppression and activation of radio AGN around galaxy clusters*, Monthly Notices of the Royal Astronomical Society, Volume 535, Issue 1, Nov 2024, Pages 217-222.

Chapter 3 is based on material published in Paper ii, Chapter 4 is based on material published in Paper iii, and Chapter 5 is based on material published in Paper i.

All work presented in this thesis was carried out by the author, with supplementary advice from the paper co-authors listed above.

Chapter 1

Introduction

1.1 Galaxy Evolution

Since astronomers started observing galaxies, it has been noticed that their features consist of differences and similarities that allow them to be classified into groups. Be it colour, shape or size, these characteristics have led astronomers to notice correlations between intrinsic galaxy properties, with the first major realisation of this concept being the publication of the Hubble Sequence by Hubble (1926), who presented a morphological classification scheme that presents a non-temporal sequence of galaxy morphology.

Hubble proposed that galaxy morphologies can be split into two main categories: ellipticals – or early-type galaxies, and spirals – or late-type galaxies, and from that, spirals can be split into barred or non-barred. Elliptical galaxies are smooth and featureless – containing little to no observable structure, whilst being very red in colour; spiral galaxies however are much bluer, with intricate gas and dust substructures visible within their larger spiral shape. However, there were evident sub-classifications within these two categories that resulted in the creation of the Hubble Tuning Fork structure, which is shown in Figure 1.1. It was this structure that led Hubble to adopt the nomenclature of referring to ellipticals as "early-type" galaxies and spirals as "late-type" galaxies. This terminology has since had a habit of confusing young (and old) astronomers (myself included), but was intended to

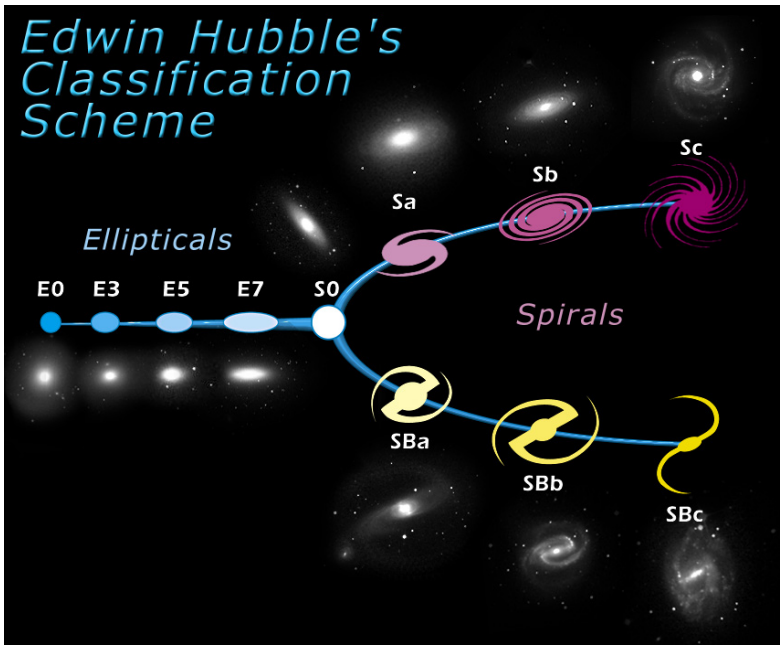

Figure 1.1: The Hubble Tuning Fork, or Hubble Sequence, as described in Hubble (1926). The sequence shows a continuous scale of galaxy morphology complexity, from smooth, featureless, circular E0 type galaxies on the left, through to the split of spirals into barred (SB) and non-barred (S), with the most detailed structures on the right. *Image credit: NASA & ESA*

be purely in reference to the location within the Hubble Tuning Fork, as opposed to any temporal connotations.

Upon further investigation into these classifications, it was found that elliptical galaxies are redder in colour due to their stellar population, which consists primarily of old, low-mass stars that live much longer lives than their more massive counterparts. Spiral galaxies on the other hand appear bluer due to their younger stellar population, which they are actively forming due to their higher star-formation rates (SFRs) (Kennicutt, 1998). Many of the young, blue stars found in star-forming galaxies (SFGs) are much more massive than the old, red stars found in elliptical galaxy counterparts, and as such live much shorter, more explosive lives.

These observations implied that there was an evolution from the younger, bluer spiral galaxies to the older, redder elliptical galaxies (Sandage et al., 1970), during which the spiral structure became smoother and the younger stars died out, leaving only the older, redder stars behind. This finding suggested that SFGs and elliptical

galaxies were not entirely different species, but were in fact just the same galaxy at different points in its life. However, this discovery left even more questions in its wake: What causes this evolution? Is it purely temporal, or are there other influences at play? Why do galaxies become "red and dead" rather than continuously forming new stars? As such, the field of galaxy evolution was not solved with the finding of the dichotomy of galaxy morphology, but rather it was just beginning, and astronomers set out to answer the exponentiating number of questions that arose with every new discovery.

Around 1980, Dressler set out to answer one of these new questions by investigating the relationship between morphology and environmental density, resulting in the production of some of his most influential work. Dressler (1980) found that galaxy morphology is directly linked to environment through what he termed the *Morphology–Density Relation* (see Figure 1.2), which quantifies how galaxies in high density environments are more likely to be elliptical, red and dead, and galaxies in lower density environments are more likely to be blue, spiral-structured, star-forming galaxies. This relationship implies that there is a strong correlation between galaxy evolution and environment, and suggests that perhaps star formation in late-type structures is cut off, or "quenched", during gravitational infall into larger, denser structures such as galaxy clusters.

With his work, Dressler had begun to address one of the biggest questions still underpinning the field of galaxy evolution today: Are galaxies influenced more by nature or nurture? Is a galaxy's evolution predetermined by its intrinsic properties, or can it be altered by its surroundings? In this thesis, we will attempt to contribute to this ever-growing field of research by answering three questions regarding the relationship between a galaxy's evolution and its surroundings. Firstly, how does the number density of SFGs change with cluster proximity? Secondly, does proximity to the cluster environment also have an effect on the activity of a galaxy's nucleus? And finally, can galaxy properties such as the orientation of an active galactic nucleus' jet, or the location of enhanced star formation, be used to investigate the nature of the local environment? In order to address these questions, we must first have a better understanding of the current astronomical background that underpins them, starting with environment.

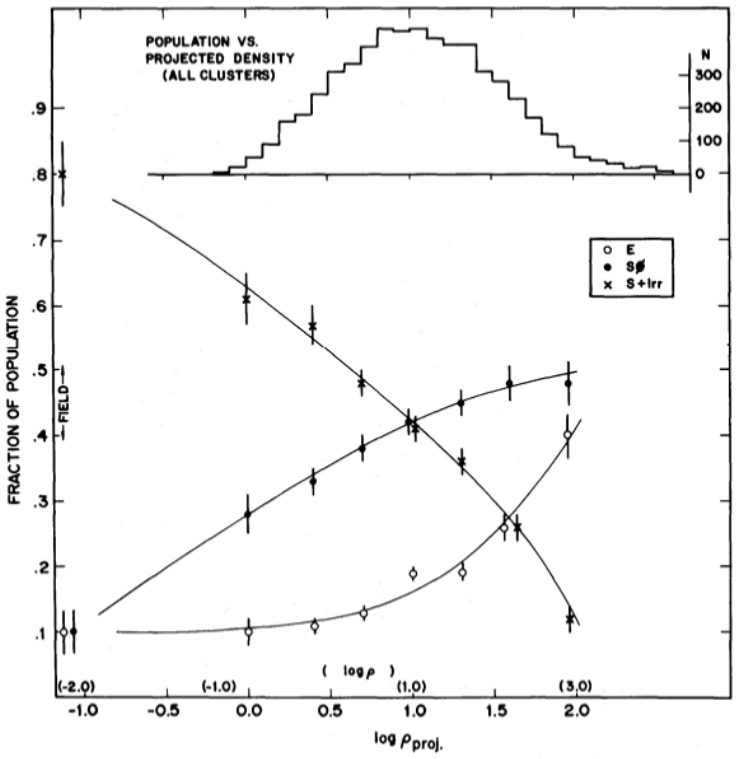

Figure 1.2: The morphology-density relation, as presented in Dressler (1980). This illustration shows the first published evidence of how the fraction of E, S0, and S+I galaxies vary with density.

1.2 Global Environment

The global environment refers to the primary features of the large-scale structure of the Universe, or the "cosmic web" (Arnold et al., 1982; Bond et al., 1996; Springel et al., 2006), which consists of large, dense nodes of galaxies in groups and clusters (Aragón-Calvo et al., 2010), connected by a web-like structure of filaments and sheets, and between them large, empty voids with very little matter at all (see Figure 1.3). The large-scale structure, and all other objects in the Universe, appear to obey hierarchical structure formation which began in the very early Universe. At such times, everything was nearly homogeneous except for small fluctuations (Mukhanov & Chibisov, 1981), which eventually caused over- and under-density perturbations in the matter distribution of the Universe. Evidence for these perturbations can be seen in the small temperature fluctuations of the cosmic microwave background (Penzias & Wilson, 1965) – relic radiation consisting of the first photons that were able to stream freely through the Universe. Over time, the small matter overdensities at the beginning of the Universe grew due to the accretion of matter through gravity (Springel et al., 2006), resulting in the "bottom-up" process by which smaller objects merge to form larger ones, from molecular gas forming stars, all the way up to the formation of the largest gravitationally bound structures in the universe – galaxy clusters (Gunn & Gott, 1972).

1.2.1 Clusters

With masses of more than $\sim 10^{14} M_{\odot}$, galaxy clusters are referred to as the "largest gravitationally bound structures in the Universe" because they are mostly virialised within a certain radius, meaning that the kinetic energy and the gravitational potential energy of the constituents of the system are in equilibrium. As there is no hard boundary that dictates the edge of a galaxy cluster, astronomers usually refer to clusters in terms of their virial radius, which is the radius within which most mass has been virialised. One can define this and similar units of radial measurement based on a chosen overdensity value for a given cluster, using the

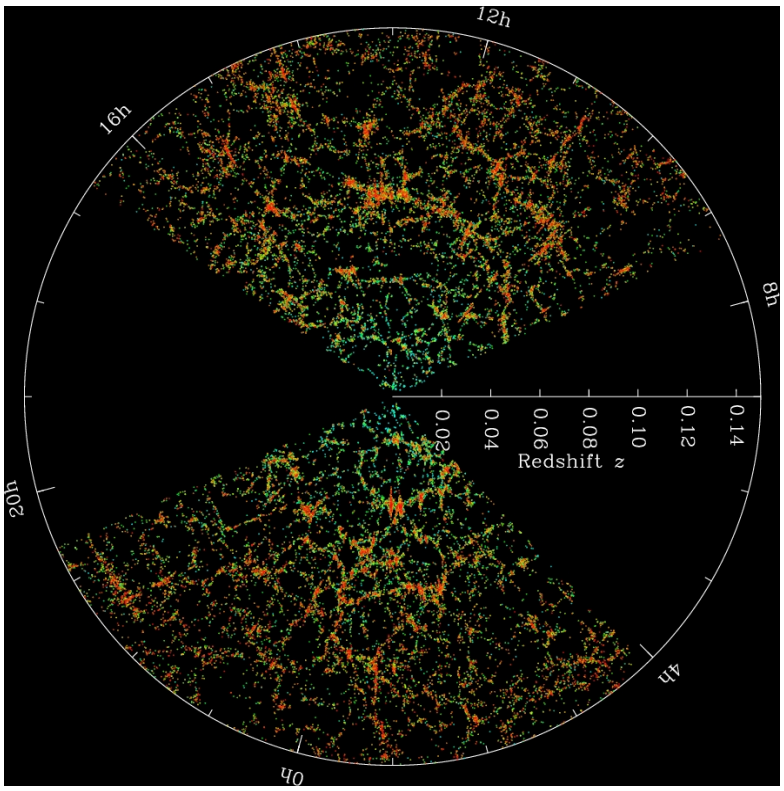

Figure 1.3: A slice through the SDSS 3-dimensional map of the distribution of galaxies with redshift. This image presents observational evidence of the cosmic web and large-scale structure of the Universe. *Image credit: M. Blanton and the Sloan Digital Sky Survey.*

formula

$$r_\Delta = \left(\frac{3M_\Delta}{4\pi\Delta\rho_c} \right)^{1/3}, \tag{1.1}$$

where Δ is the chosen overdensity constant, M_Δ is the mass within r_Δ, and ρ_c is the critical density of the Universe. For example, throughout this thesis we commonly use R_{500}, which is the radius within which the average density is 500 times that of the critical density of the Universe. R_{200} is also a common choice when analysing and comparing galaxy clusters, where $R_{500} \sim 0.7R_{200}$, as the virial radius, $R_{vir} \sim R_{200}$.

Despite hosting between hundreds and thousands of galaxies, galaxy clusters consist primarily of dark matter, with the mass from a cluster's dark matter halo comprising $\sim$ 90% of its mass (Gonzalez et al., 2013). Of the remaining 10%, $\sim$ 9% consists of the intracluster medium (ICM) (Lau et al., 2009), which is a hot (10^7 K), low-density (10^{-3}cm^{-3}) plasma. Finally, the remaining $\sim$ 1% of the mass of the cluster is made up of galaxies, with the most massive often being the brightest cluster galaxy (BCG). This large, bright, often quiescent galaxy forms via hierarchical growth, both from the merger of larger galaxies and from the eventual cannibalism of satellite galaxies that fall towards the cluster's gravitational potential well (Ostriker & Hausman, 1977; Merritt, 1984) due to dynamical friction. Consequently, this galaxy's position is a good estimate for the centre of its host cluster.

1.2.2 Groups

After clusters, galaxy groups have the next largest dark matter halos in the Universe. The definition of the mass or number of galaxies within a galaxy group is still in contention, but a review of the literature by Lovisari et al. (2021) suggests that a reasonable interval is somewhere between 3 and 50 galaxies, with some larger galaxy groups being massive enough to hold onto an intragroup medium (IGM, Mulchaey et al., 1996; Helsdon & Ponman, 2000; Oppenheimer et al., 2021). This local environment can have its own effects on its group's members (Jaffé et al., 2016; Bianconi et al., 2018; Haines et al., 2018; Benavides et al., 2020; Lopes et al., 2024) that differ from those seen by the larger global environment - a concept that we explore in more detail later in this thesis.

1.2.3 Filaments

Local environment is not just restricted to galaxy groups - it can also be seen in filaments between clusters too, which contain a hot plasma known as the warm hot intergalactic medium (WHIM, Aragón-Calvo et al., 2010; Cautun et al., 2014; Martizzi et al., 2019). Filaments can span up to tens of megaparsecs in length (Finoguenov et al., 2003; Tanimura et al., 2020), and have thickness radii ranging between 0.7 and 5 Mpc (Dolag et al., 2006; Kuchner et al., 2020). These bridges in the large-scale structure act as galactic highways, funnelling galaxies and galaxy groups in channels towards galaxy clusters.

With all of these distinctive and varied types of environment, it is no surprise that galaxies residing in different neighbourhoods across the large-scale structure experience, much like us, innumerable different influencing effects throughout their lifetimes. In order to gain an understanding of these influencing effects, one must investigate the processes that underpin star-formation within a galaxy, and how they might be disrupted, by means of the Baryon Cycle.

1.3 The Baryon Cycle

Star-forming galaxies represent one of the first phases of a galaxy's evolution, and they often have to start contending with the plethora of different environmental quenching mechanisms that can affect a galaxy throughout its lifetime, all of which depend largely on the disruption of the Baryon Cycle; that is, the cycle by which gas is moved between the interstellar medium (ISM), circumgalactic medium (CGM), and the outer environment, by various heating and cooling processes that can lead to increased or decreased star formation [see Péroux & Howk (2020) or Donahue & Voit (2022) for a review on the Baryon Cycle].

In SFGs unaffected by external quenching mechanisms, gas from the outer environment becomes gravitationally bound to the galaxy halo, forming the CGM. Gas in the CGM then gets transported to the ISM via cooling flows, where it forms into molecular clouds before eventually collapsing into young, new stars. The formation of new stars along with the explosive power of both supernovae

and active galactic nuclei (AGN) expel surrounding gas from the ISM out of the galaxy in outflows, starting the cycle anew. However, this cycle can be interrupted by a variety of external mechanisms that have the resulting effect of quenching star formation.

1.3.1 Environmental Interactions

1.3.1.1 Ram Pressure Stripping

Ram pressure stripping (RPS) is the process by which the velocity differential between a moving galaxy and the cluster-virialised, hot ICM causes any gas which is less gravitationally bound than the strength of the ram pressure to be pushed out of the galaxy. Ram pressure strength is proportional to both the density of the ICM and the square of the galaxy velocity relative to the ICM (Gunn & Gott, 1972), making ram pressure effects more significant in denser, more dynamically excited environments.

Strong enough ram pressure is capable of stripping both the CGM and parts of the ISM from a galaxy [see Cortese et al. (2021) or Boselli et al. (2022) for a review on RPS as a quenching mechanism]. Although this process does result in rather sudden quenching within the galaxy due to the removal of the star-forming cold gas reservoirs, it is also possible for the turbulence of the cold, molecular gas due to the RPS to induce star formation in a long tail trailing behind the galaxy along the direction of infall (Ebeling et al., 2014; Jaffé et al., 2018; Roberts et al., 2021a). These rare structures are called jellyfish galaxies due to their long, blue, tendril-like tails.

Weaker ram pressure, either due to a slower-moving galaxy or a less-dense ICM, might only be capable of stripping the CGM from a galaxy, therefore inducing "strangulation" or "starvation".

1.3.1.2 Strangulation / Starvation

"Strangulation" is the process by which the CGM is stripped from a galaxy, cutting off the cooling flows which replenish the ISM cold gas supply (Balogh et al., 2000), whilst "starvation" is the prevention of accretion of any more cold gas (Larson et al., 1980), both of which combine to ultimately have the effect of halting the galaxy from forming any new stars. These processes are gradual quenching mechanisms, as the galaxy still has cold gas reservoirs within the ISM, which will be slowly depleted as the galaxy's final stars are formed. The CGM can be stripped by either RPS or by tidal effects due to other nearby galaxies, which pull the less-gravitationally bound CGM away from its host galaxy.

1.3.1.3 Harassment and Galaxy Mergers

Tidal effects that cause galaxy quenching are often referred to as "harassment", and occur in high density environments where fast-moving galaxies are more likely to experience high-speed "fly-bys". This combination of velocity and the gravitational pull of other galactic halos is capable of disrupting and pulling away not just gas reservoirs within the ISM and CGM, but stars themselves as well (Farouki & Shapiro, 1981; Moore et al., 1996). The extent to which a galaxy's structure and stellar material is disrupted is dependent on its mass, due to the fact that lower mass galaxies are less gravitationally bound and therefore more easily disturbed.

In lower-density environments, galaxies have much lower relative velocities and are therefore more likely to interact by merging, as the impulse of the gravitational pull between the objects has a longer timescale over which to act, ultimately winning out over their relative velocities (van Dokkum et al., 1999; Ellison et al., 2010). Depending on the content of the galaxies at the time of merging, it is possible for the interaction to either cause quenching due to the expulsion of star-forming gas (Makino & Hut, 1997; Angulo et al., 2009; Wetzel et al., 2009a,b; White et al., 2010; Cohn, 2012), or to cause increased star-formation as cold molecular clouds of gas collide and cause starbursts (Mihos & Hernquist, 1994; Di Matteo et al., 2007; Cox et al., 2008; Hopkins et al., 2013).

1.3.1.4 Pre-processing

All of the above-mentioned mechanisms can be seen both within clusters themselves, and in high-density environments outside of clusters, such as filaments and groups. Quenching that occurs outside of clusters is referred to as pre-processing, and is thought to be part of the reason why there is such a high quiescent fraction seen in clusters (Fujita, 2004; Hou et al., 2014; Roberts & Parker, 2017; Bianconi et al., 2018). If quenching were to solely occur within clusters, there would be a higher proportion of SFGs seen in cluster environments which had recently entered but not yet been quenched. Instead, studies find that the SFG fraction decreases gradually with radius, implying that quenching starts to occur before cluster infall (Haines et al., 2015; Lopes et al., 2024).

1.3.2 Internal Processes

1.3.2.1 Outflows

As well as external mechanisms that cause quenching, there are also internal galaxy properties that are capable of ending star-formation as well. Although outflows due to stellar formation and supernovae explosions are part of the Baryon Cycle, it is also possible for these outflows to be strong enough to heat or expel the reservoirs of cold, star-forming molecular gas from the ISM (Larson, 1974; Dekel & Silk, 1986; Mac Low & Ferrara, 1999; Christensen et al., 2016), thus reducing star formation.

However, star-formation and supernovae are not the strongest sources of outflows responsible for gas expulsion and stellar quenching. Even stronger outflows are generated by active galactic nuclei, which we will discuss in the next section.

1.4 Active Galactic Nuclei

As most, if not all, massive galaxies have a supermassive black hole (SMBH) at their centres (Kormendy & Richstone, 1995), these galaxies are capable of having

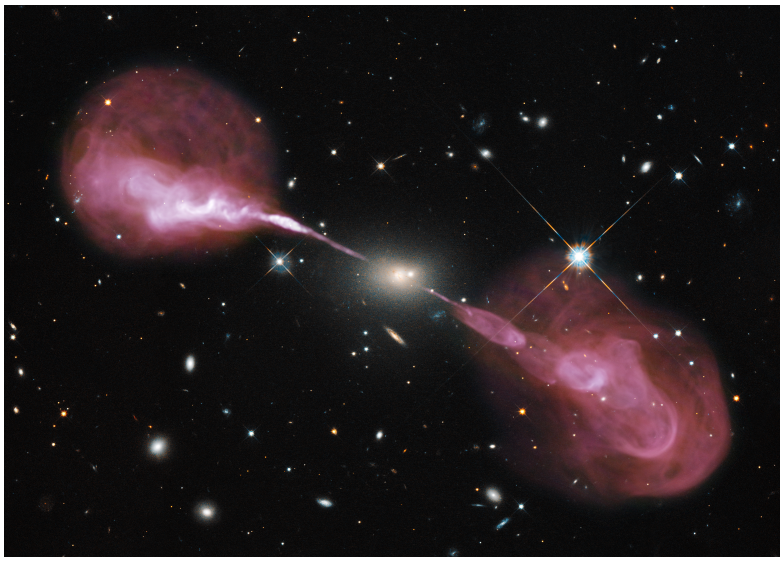

Figure 1.4: Hercules A: An optical image of the galaxy 3C 348 taken by the Hubble Space Telescope, superimposed with a radio image of its jets in pink. *Image credit: NASA & ESA*

an active galactic nucleus – a SMBH with enough fuel feeding its accretion disk to induce the emission of electromagnetic radiation across the entire spectrum. AGN can broadly be classified into radio-loud and radio-quiet categories, depending on the strength of their radio emission.

Radio-loud AGN exhibit powerful relativistic jets that can extend for hundreds of kiloparsecs, often significantly larger than their host galaxies. These jets, composed of highly collimated plasma, emit across all wavelengths via synchrotron radiation and inverse-Compton scattering. Radio-quiet AGN, on the other hand, lack these powerful jets but can still be highly luminous, with their emission dominated by the accretion disk rather than extended radio structures. Seyfert galaxies, for example, are a well-known class of radio-quiet AGN that are typically found in star-forming spiral galaxies.

The jets of radio-loud AGN are among the most impressive structures in the Universe. They can span hundreds of kiloparsecs in length – often significantly larger than their host galaxies – dispersing into large, cloud-like lobes (see Figure 1.4). These jets consist of relativistic, highly collimated plasma that emits in all wavelengths via the processes of synchrotron radiation and inverse-Compton scattering.

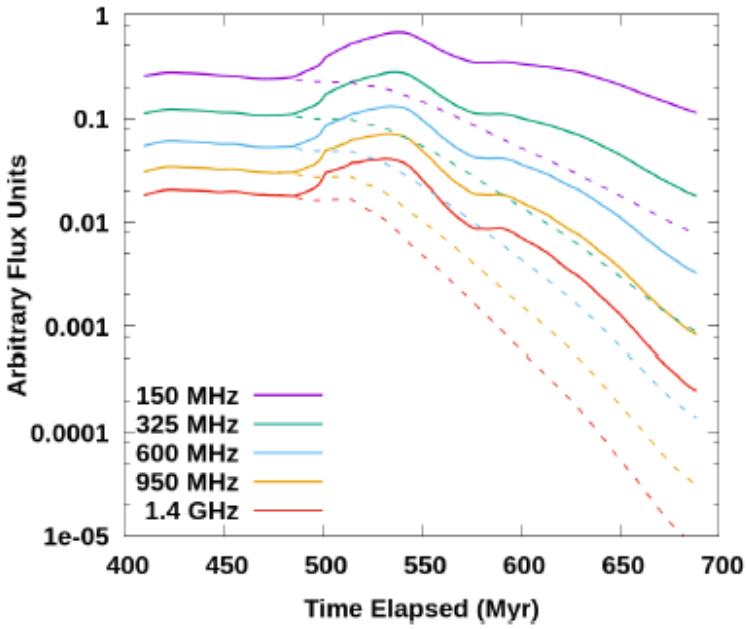

Figure 1.5: From O'Neill et al. (2019a), the time evolution of integrated fluxes from a simulated radio tail, at varying radio frequencies. Higher fluxes are seen for lower frequency radio emissions across the whole time period, whereas the flux strength of higher frequency emissions drops off rapidly with time evolution. Solid lines show fluxes for a shocked source, whereas dashed lines show fluxes for an unshocked source.

Synchrotron emission occurs when a relativistic, charged particle is subject to an acceleration perpendicular to its velocity. In the case of AGN jets and lobes, the charged particles in the emitted plasma travel in spiral-shaped paths around the varied magnetic fields in the jet/lobe structure, emitting photons as they go. As the charged particles travel further away from their emission source and become older, they lose energy due to the emission of synchrotron radiation, resulting in the wavelengths of the photons they emit getting longer and longer, into the low-frequency radio range. As such, these wavelengths are the only part of the EM spectrum at which the full structure of an AGN's jets and lobes can be determined (Feretti et al., 1998; O'Neill et al., 2019a; Lusetti et al., 2024; Bruno et al., 2024), as can be seen in Figure 1.5.

Similarly to how the gas associated with a SFG can experience ram pressure stripping from the ICM, AGN jets can also experience ram pressure. However, instead of stripping all of the plasma from the jet, the ram pressure causes the jet to bend

(Cowie & McKee, 1975; Begelman et al., 1979; O'Dea, 1985; Roberts et al., 2021b). Extended AGN that have experienced bending are either classified as wide-angle tail (WAT) sources or narrow-angle tail (NAT) sources (see Figure 1.6), depending on the severity of their tail bending. Although there is some uncertainty within the radio astronomy community as to the exact definition of what constitutes a NAT or WAT (O'Dea, 1985; Terni de Gregory et al., 2017), it is reasonably accepted to define WATs as having an obtuse bending angle of $> 90°$ between their tails, and for NATs to have an acute bending angle of $< 90°$ between their tails (Mingo et al., 2019). Here, the angle between the tails of an extended radio source is assumed to be the convex angle between the two vectors taken from the galaxy centroid to the individual tail centroids. The level of bending seen can give an indication as to the strength of the ram pressure experienced, and therefore the velocity of the galaxy and the density of the ICM in the local environment. Furthermore, the orientation of the jet bending can provide information about the angular direction the galaxy is travelling on the plane of the sky, which is often quite difficult to determine for regular galaxies.

1.4.1 The Duality of AGN Triggering & SFG Quenching

Although every galaxy with a SMBH is capable of hosting an AGN, not every galaxy does, because specific conditions must be met in order to induce nuclear activity. One of these conditions is the amount of fuel required to trigger an AGN, which can be met via ram pressure. In the process of pushing gas out of a galaxy, ram pressure stripping causes some of this gas to be pushed close to the SMBH, thus providing the fuel required to make the galactic nucleus active (Poggianti et al., 2017a; Marshall et al., 2018; Ricarte et al., 2020; Peluso et al., 2022).

Furthermore, AGN are likely to be triggered by galaxy mergers for a similar reason. The large amount of tidal interactions and turbulence between galaxies as they merge causes gas and other matter to get thrown around, often passing closer to the SMBHs of the host galaxies and triggering enhanced AGN activity (Treister et al., 2012; Ehlert et al., 2015; Ellison et al., 2011). Finally, AGN in BCGs are provided with the fuel required for their activity via cooling flows that feed ICM gas residing close to the centre of the cluster into the central galaxy's black hole (Best et al., 2007; Donahue & Voit, 2022).

Figure 1.6: The narrow-angle radio tails of NGC 1265 within the Perseus Cluster. *Image credit: M. Gendron-Marsolais et al.; S. Dagnello, NRAO/AUI/NSF; Sloan Digital Sky Survey.*

Once triggered, AGN are capable of ejecting gas from their host galaxies via radiation pressure and jet outflows, therefore shutting off star formation (Silk & Rees, 1998; Murray et al., 2005; Fabian, 2012; Combes, 2017; Morganti, 2017; Harrison & Ramos Almeida, 2024). These processes are described by two modes: "radiative mode" and "radio mode". Radiative mode occurs when an AGN's disk is highly luminous due to extremely high accretion rates. The radiation power from the disk is theorised to be able to drive huge outflows which have the power to completely eject cold gas from a galaxy (Fabian, 1999; Benson et al., 2003), although observational evidence of this process is often much less dramatic. Radio mode occurs when an AGN is emitting large radio jets, which are produced from lower accretion rates. These jets produce outflows in a very localised area, but also have the effect of heating the CGM and therefore inducing starvation (McNamara & Nulsen, 2007; Bower et al., 2012).

Thus, the triggers that enhance AGN activity - which itself is already a quenching mechanism - are also responsible for shutting down star formation. AGN have also been seen to trigger star formation (Ishibashi & Fabian, 2012; Gaibler et al., 2012), particularly in the case of radio-quiet AGN, which are often found in star-forming spiral galaxies, such as Seyfert Galaxies (Seyfert, 1943). In contrast, radio-loud AGN are more commonly associated with feedback processes that can quench star formation in their host galaxies. These observations result in a complicated tangle of mechanisms which appear to sometimes trigger and sometimes quench star-formation and nuclear activity in both SFGs and AGN. We must therefore study these galaxies in detail in order to gain a greater understanding of them, but to do so we need to be able to identify SFGs and AGN reliably.

1.5 Identification of SFGs and AGN

In the nearby Universe where galaxies are visible at higher resolutions, it is easy to identify star-forming galaxies due to their unique and intricate spiral structure and blue colour. However, this observation does not necessarily mean that they are devoid of an AGN, as discussed in the previous section. Radio-quiet AGN can be present in both star-forming and quiescent galaxies, whereas radio-loud AGN are more commonly found in massive elliptical hosts. Therefore, identifying

AGN requires distinguishing between these two populations using a combination of optical and radio diagnostics. Furthermore, when observing more distant galaxies, it becomes more difficult to identify a galaxy as quiescent or star-forming purely based on their colour or morphology, due to the lower spatial resolution available. As such, there are a variety of methods that have been developed in order to determine how active or star-forming a galaxy might be.

In SFGs, the large amounts of UV radiation emitted due to the formation of young stars leads to the ionisation of any surrounding hydrogen, resulting in large clouds of HII. Through the recombination of ionised electrons and hydrogen nuclei, Hα emission is produced; thus, Hα is a strong indicator of star formation (Kennicutt, 1998). However, Hα is easily absorbed by dust clouds, making it unreliable as a quantitative star-formation indicator. Furthermore, although it is possible to measure Hα emission using imaging filters or slit spectroscopy, it is often the case that Hα emission is detected with a single fibre aimed at the centre of a galaxy, meaning that such a measurement is not a good representation of the spread of the Hα emission over the entire extended source.

These pitfalls make radio detection of SFGs a very attractive alternative, as dust clouds are transparent to radio emission, resulting in a much more accurate representation of the SFR of a galaxy without any issues due to extinction. Core-collapse supernovae occur much more frequently in highly star-forming regions than elsewhere, and as such emit radio waves via the process of ionising and accelerating electrons to relativistic speeds. These electrons get accelerated in large, galactic magnetic fields, thus allowing them to emit synchrotron radiation observable at radio wavelengths (Condon, 1992).

However, due to the fact that they emit radiation across the entire electromagnetic spectrum, AGN can be detected via Hα emission (which is more prominent in radio-quiet AGN) or radio emission (which is stronger in radio-loud AGN due to their relativistic jets). Due to this issue, other features and emission lines of galaxies must be observed and compared in order to make a clear distinction between SFGs and AGN when taking observations at radio wavelengths, and various diagnostics have been proposed and compared in the literature to achieve this goal (Best & Heckman, 2012; Gürkan et al., 2018; Sabater et al., 2019)

1.5.1 D_{4000} vs. $L_{150\mathrm{MHz}}/M_*$

The D_{4000} index measures the strength of the 4000Å break in a galaxy's spectrum. The break arises from the accumulation of metal absorption lines such as calcium, magnesium and sodium, found at wavelengths of $\lambda < 4000$Å. These ionised metals are mostly found in cold, old stars (K-type and M-type), and so the 4000Å break is an indicator of this stellar population. A higher D_{4000} means that the galaxy has a more dominant population of old stars, and is therefore more likely to be quiescent.

Meanwhile, $L_{150\mathrm{MHz}}/M_*$ provides a measure of the specific low-frequency radio luminosity of a galaxy. Solely within the star-forming population, this value gives an indication of the number of supernovae occurring per unit mass, which is why SFGs have an inverse correlation of D_{4000} strength with $L_{150\mathrm{MHz}}/M_*$ (see Figure 1.7) – galaxies with a lower fraction of older stars will have a higher supernovae rate due to their younger stellar population. However, radio-loud AGN exhibit much higher low-frequency radio luminosities than SFGs for the same stellar mass, due to the intensity of synchrotron emission from their relativistic jets. Radio-quiet AGN, on the other hand, lack powerful jets and typically have lower radio luminosities.

Therefore, the plot of D_{4000} vs. $L_{150\mathrm{MHz}}/M_*$ can be used to attempt to separate SFGs and AGN (Best et al., 2005b)[1], as shown in Figure 1.7. However, it is not quite as simple as AGN having higher specific radio luminosities and higher D_{4000} values, and vice versa for SFGs. The location of the division line on this plane has been continuously refined over time (Kauffmann et al., 2008; Sabater et al., 2019) to achieve the cleanest separation of AGN and SFGs, but, due to the intrinsic variables being measured, the diagnostic is less efficient at separating galaxies with both star-forming and active nuclear features.

1.5.2 $[\mathrm{O_{III}}]/\mathrm{H}\beta$ vs. $[\mathrm{N_{II}}]/\mathrm{H}\alpha$

The $[\mathrm{O_{III}}]/\mathrm{H}\beta$ vs. $[\mathrm{N_{II}}]/\mathrm{H}\alpha$ diagnostic, better known as the "BPT" diagnostic – named after the authors who proposed the measure (Baldwin et al., 1981) – uses

[1]Confusingly, upon looking this paper up I discovered that it is very frequently mis-cited as Best et al. (2005a), and vice versa!

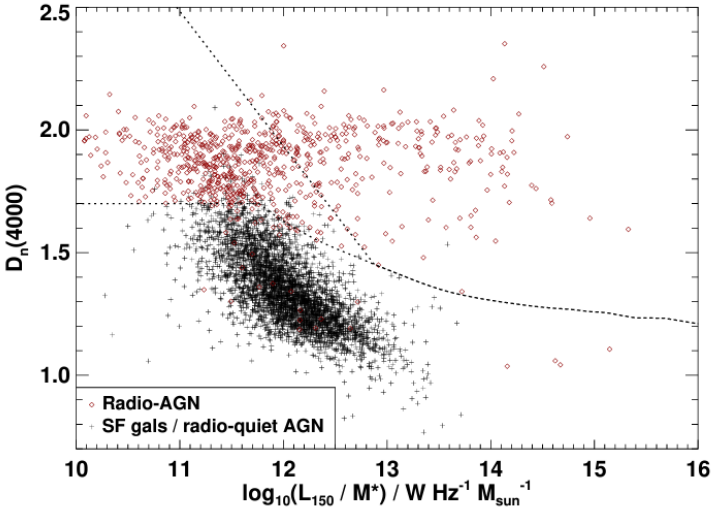

Figure 1.7: The D_{4000} vs. $L_{150\mathrm{MHz}}/M_*$ diagnostic plot taken from Sabater et al. (2019), shown with radio sources from the LOw-Frequency ARray (LOFAR) Two-metre Sky Survey (LoTSS). The upper dotted line shows the revised division suggested by Kauffmann et al. (2008), whereas the lower dotted line is the division adopted by Sabater et al. (2019) in order to maximise agreement with more recent, sophisticated classifications undertaken by Gürkan et al. (2018).

the ratios of galaxy emission lines in order to differentiate between AGN and SFGs.

Both ratios serve to measure the strength of the hard ionising radiation of the galaxy. [O_{III}] and [N_{II}] are forbidden lines emitted by doubly ionised oxygen and ionised nitrogen respectively, both of which require high-energy photons. Thus, both emission lines are good tracers of hard, ionising radiation from an AGN's accretion disk, which produces photons in the far-UV or X-ray. This method is particularly effective for identifying radio-quiet AGN, which often exhibit strong optical emission lines. Radio-loud AGN, on the other hand, may have weaker line emission if their jets have cleared out gas from the host galaxy. Star-forming regions, by contrast, produce softer UV radiation that is less effective at creating these ionised elements, therefore leading to weaker [O_{III}] and [N_{II}] lines.

[O_{III}] and [N_{II}] are normalised by Hβ and Hα respectively, due to their wavelengths. The primary and secondary emission lines from [O_{III}] are found at 5007 Å and 4959 Å (Bowen, 1927) – very close to Hβ at 4861 Å. Meanwhile, the primary and secondary emission lines from [N_{II}] are found at 6584 Å and 6548 Å (Bowen, 1927), right next to Hα at 6563 Å. These choices mean that the measure of the hard-

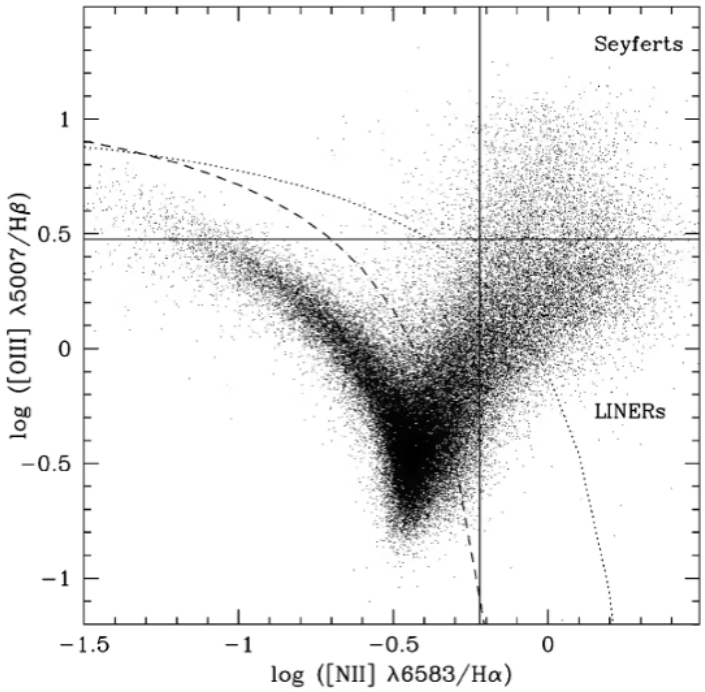

Figure 1.8: A BPT diagram taken from Kauffmann et al. (2003a). The dotted line shows the SFG-AGN division suggested by Kewley et al. (2001), whereas the dashed line is the revised division proposed by Kauffmann et al. (2003a). The vertical and horizontal lines dictating the Seyfert and LINER regions are proposed by Ho et al. (1997).

ioinising radiation of the galaxy can be normalised by the strength of that galaxy's radiation in that region of the spectrum, thus accounting for any dependencies on distance and dust extinction.

The specific classification boundaries for the BPT diagram have been undergoing revision since their conception (Ho et al., 1997; Kewley et al., 2001; Kauffmann et al., 2003a), but it is widely accepted in the literature that the diagram is able to separate not just SFGs and AGN, but also Seyfert galaxies from less active AGN referred to as low-ionisation nuclear emission regions (LINERs), as shown in Figure 1.8.

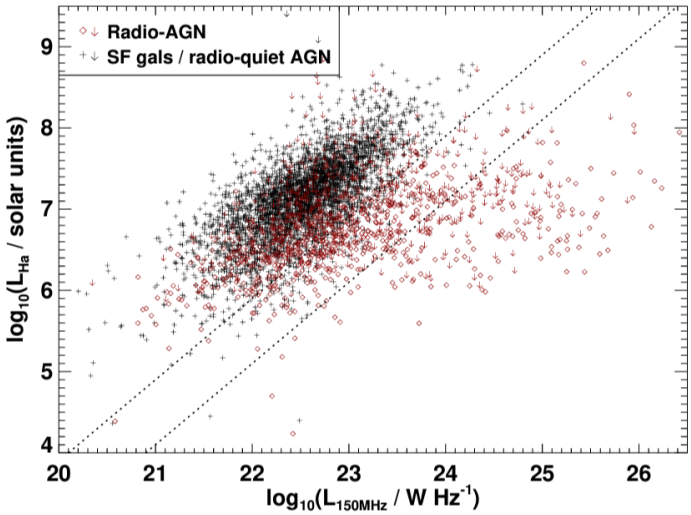

Figure 1.9: A $L_{H\alpha}$ vs. L_{Rad} diagram taken from Sabater et al. (2019), where the radio luminosity has been calibrated to the LoTSS 150MHz frequency. The right-hand dashed line shows the boundary proposed by Best & Heckman (2012), with the left-hand dashed line being an additional constraint introduced by Sabater et al. (2019) to maximise agreement with Gürkan et al. (2018).

1.5.3 $L_{H\alpha}$ vs. L_{Rad}

The $L_{H\alpha}$ vs. L_{Rad} diagnostic is based on the concept that the star-formation rate of SFGs can be directly measured via both Hα luminosity, $L_{H\alpha}$, and radio luminosity, L_{Rad}, meaning that these properties must be correlated. AGN on the other hand are capable of emitting $H\alpha$ and radio emission of varying strengths, meaning they produce very little correlation in the $L_{H\alpha}$-L_{Rad} plane. However, radio-loud AGN do emit much stronger radio emission than SFGs, meaning that this method is particularly effective for separating radio-loud AGN from both SFGs and radio-quiet AGN by defining the outer boundary of the SFG correlation region (Kauffmann et al., 2008). However, because radio-quiet AGN have much lower radio luminosities, they may still overlap with the star-forming galaxy population in this diagram. The boundaries for this diagnostic have been revised by Best & Heckman (2012) and Sabater et al. (2019), with the latter building upon work from Gürkan et al. (2018). We show the plot of this diagnostic from Sabater et al. (2019) in Figure 1.9.

1.5.4 WISE W1-W2 vs. W2-W3

The WISE W1-W2 vs. W2-W3 diagnostic compares the infrared colours of galaxies in order to separate SFGs from AGN. W1 corresponds to infrared emission at 3.4μm, W2 at 4.6μm, and W3 at 12μm.

The W1 and W2 bands are primarily dominated by continuum emission from old stars, therefore providing a baseline for a galaxy's underlying stellar population. W1 is minimally affected by dust due to the fact that emission from hot dust peaks at longer wavelengths. W2 is therefore more sensitive to hot dust emission from AGN activity, whereas W1 is a good tracer of the bulk stellar content. W3, on the other hand, contains strong Polycyclic Aromatic Hydrocarbon (PAH) emission bands, which are indicative of the presence of warm dust usually associated with star formation.

Given these WISE band properties, it follows that the W1-W2 colour is sensitive to hot dust heated by AGN activity, but less affected by variation with star formation. W1-W2 provides more of an indication as to whether a source is an inactive quiescent galaxy, or an early-type hosting an AGN. However, inactive quiescent galaxies do not emit at radio wavelengths, making this distinction unnecessary when, as in this thesis, analysing a radio sample.

The W2-W3 colour on the other hand is very effective at separating SFGs from AGN, due to the fact that star formation produces strong PAH and warm dust emission, and AGN produce lots of hot dust emission. SFGs therefore have high W2-W3 values, having low W3 and high W2 magnitudes, whereas AGN have low W2-W3 colour values, due to having low W2 magnitudes and high W3 magnitudes. This relation can be seen in Figure 1.10. Studies such as Cluver et al. (2014); Herpich et al. (2016); Sabater et al. (2019); Hardcastle et al. (2019) utilise this separation in the W2-W3 axis to set a boundary which distinguishes AGN from SFGs, which we then follow in this work. Further details of the use of this classification method are outlined in Section 2.2.2.

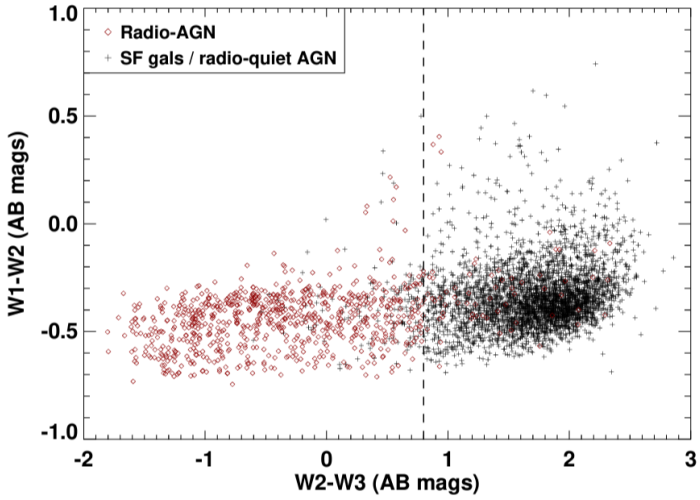

Figure 1.10: The WISE W1-W2 vs. W2-W3 diagnostic taken from Sabater et al. (2019). The single boundary has been derived in accordance with the results of Gürkan et al. (2018), and is very similar to that adopted by Herpich et al. (2016).

1.6 Structure of this Thesis

In this thesis, we explore the impact of galaxy cluster environments – from their cores to the very outskirts of their outskirts – on the galaxies that live in and near them, at radio and optical wavelengths. The structure of the thesis is as follows: in Chapter 2 we outline the details of the surveys used in this work and the common methods used throughout the thesis. In Chapter 3 we address the first question we laid out in this chapter: "how does the number density of SFGs change with cluster proximity?" We begin by investigating how far out the decline of the radio-identified SFG fraction starts, and how the quenching of SFGs in this distribution is affected by both the stellar mass of the galaxies and the local environments in which they live. In Chapter 4, we perform a similar analysis on the radial distribution of the radio AGN fraction, comparing both host galaxy stellar mass and radio luminosity. We discuss how these galaxy properties might correlate with the radial distribution we discover. By conducting this analysis, we address the question: "does proximity to the cluster environment also have an effect on the activity of a galaxy's nucleus?". In Chapter 5, we investigate the orbital angles of narrow-angle-tail radio galaxies with respect to their host galaxy clusters by utilising their tails as directional indicators. We find that NATs are

primarily on radially inbound orbits out to surprisingly large radii, and discuss the implications of these results. In Chapter 6, we utilise our own $H\alpha$ observations taken at the Isaac Newton Telescope (INT) of SFGs in the region of such a NAT, to attempt to find evidence of ram pressure that might extend the results found in Chapter 5. These two chapters seek to address the third scientific question of this thesis: "Can galaxy properties such as jet orientation and location of enhanced star formation be used to investigate the nature of the local environment?". Finally, we summarise the results presented in this thesis in Chapter 7, and discuss possible future work that would extend the discoveries of this thesis.

Throughout this thesis, we adopt a flat ΛCDM cosmology with $\Omega_m = 0.3$, $\Omega_\Lambda = 0.7$, and $H_0 = 100\ h$ kms^{-1} Mpc^{-1} where $h = 0.7$.

Chapter 2

Data & Methods

In this chapter we describe the data and methods used throughout this thesis. Section 2.1 presents the details of the observational surveys that we take data from, and Section 2.2 discusses the common methods used throughout this work, such as galaxy-cluster association and Abel inversion.

2.1 Survey Data

In this section we will discuss the varied data used throughout this thesis. This work primarily utilises radio data obtained from the LOw-Frequency ARray (LOFAR, van Haarlem et al., 2013) Two-metre Sky Survey (LoTSS), first and second data releases (DR1, DR2, Shimwell et al., 2019, 2022), and optical data from the Sloan Digital Sky Survey (SDSS) 16th data release (DR16, Ahumada et al., 2020), which are discussed in Sections 2.1.1 and 2.1.2 respectively. These catalogues are complemented by data from the MPA-JHU value-added catalogue (Brinchmann et al., 2004), and the Wide-field Infrared Survey Explorer (WISE) allWISE source catalogue (Wright et al., 2010), which we describe briefly in Sections 2.1.3 and 2.1.4, respectively.

2.1.1 LOFAR Two-metre Sky Survey

The LOw-Frequency ARray (van Haarlem et al., 2013) is a large radio interferometer primarily based in the Netherlands, with member countries all over Europe. It observes in the largely unexplored range of 10 - 240MHz, achieving unparalleled angular resolution and sensitivity at such low radio frequencies.

The LOFAR Two-Metre Sky Survey (Shimwell et al., 2017) is a 6" resolution, low-frequency radio survey that will span the entire Northern Sky upon its completion, centred at a frequency of 144MHz. The LoTSS first data release covers 424 square degrees of the Northern Sky, in the region of the HETDEX Spring field (Shimwell et al., 2019). It has a sensitivity of better than 0.1 mJy beam^{-1} and detected over 325,000 sources. The high-resolution radio survey is not only an order of magnitude deeper than previous wide-area radio surveys, with a median noise level of only 71μJy beam^{-1}, but is sensitive to structures with sizes ranging from 6" to more than a degree. It was released with optical counterparts for 71% of the sources (Williams et al., 2019) and photometric redshifts (Duncan et al., 2019). This data release has been used in Chapter 5, as the second data release had not yet been completed at the time the work was conducted.

The LoTSS second data release (Shimwell et al., 2022) incorporates DR1 and spans 27% of the Northern Sky over two large regions. The catalogue comprises over 4 million radio sources, the majority of which had never been detected at radio wavelengths before. The survey spans a frequency range of 120-168Mhz, with a median RMS sensitivity of 83 μ Jy beam^{-1}, and a point-source completeness of 90% at a peak brightness of 0.8 mJy beam^{-1}. At the time of beginning the research for Chapters 3 and 4, the optical counterparts for the radio sources in DR2 had not yet been released (Hardcastle et al., 2023); we therefore identified optical counterparts using SDSS DR16 ourselves (see Section 2.1.2).

2.1.2 Sloan Digital Sky Survey

The Sloan Digital Sky Survey (York et al., 2000) is a huge, optical imaging and spectroscopic redshift survey, conducted using a dedicated 2.5-m wide-angle optical telescope at Apache Point Observatory in New Mexico. It has undergone multiple

phases of operation since it first began in 2000, with each phase comprising sub-surveys with their own scientific goals. At the time of writing, the SDSS is in its fifth phase.

In this thesis (Chapters 3 and 4), we use data from SDSS data release 16 (Ahumada et al., 2020), taking sources from the DR16 spectroscopic catalogue[1], which comprises 5 789 200 sources from SDSS surveys such as Legacy, BOSS, eBOSS and more, within an approximate redshift range of $0 < z < 7$. As the work in this thesis is based entirely on analysing galaxies, we only take sources in this catalogue defined as being in the class "galaxy". This data is used in order to provide optical counterparts and spectroscopic redshifts to the LoTSS DR2 radio sources described in Section 2.1.1 for the research done in Chapters 3 and 4.

Finally, we utilise the cluster catalogue from Wen et al. (2012) and Wen & Han (2015, hereafter WH15) in order to determine the global environments of the galaxies in the SDSS DR16 spectroscopic sample. The WH15 cluster catalogue defines a sample of 158,103 clusters within the redshift range $0.02 < z \leq 0.8$, identified using a friends-of-friends algorithm from galaxies in the SDSS DR12 catalogue (Alam et al., 2015). The catalogue has a false detection rate of $< 6\%$, and is 95% complete for clusters of mass $M_{200} > 10^{14} M_{\odot}$. WH15 define the position of the brightest cluster galaxy to be the cluster centre, and identify the BCG as the brightest galaxy within $\pm 0.04(1+z)$ in redshift and 0.5 Mpc on the sky of the densest region of each cluster.

Of the clusters within WH15, 72% have spectroscopic redshifts, which are defined as either the redshift of the BCG or the mean redshift of the cluster members. The remainder of the clusters have photometric redshifts derived by Wen et al. (2012), which have a redshift-independent standard deviation of ≤ 0.018. WH15 calculate an M_{500} proxy for each cluster by first combining estimated cluster masses from six X-ray and Sunyaev–Zeldovich (SZ) cluster surveys. They compare these samples to each other by using common clusters, in order to produce empirically-derived scaling relations. These newly-scaled M_{500} are then used to calculate new values of r_{500} for this cluster sample, using the equation

$$M_{500} = \frac{4\pi}{3} r_{500}^3 \times 500 \rho_c. \tag{2.1}$$

[1] https://www.sdss4.org/dr16/spectro/spectro_access/

WH15 are then able to derive a relation between r_{500} and the observable property L_{1Mpc}, which is the background-subtracted total r-band luminosity of cluster members within $1Mpc$ of the cluster centre, measured in terms of $L^*(z) = L^*(0)10^{0.4Qz}$, which is the evolved characteristic luminosity of galaxies in the r-band, where $Q = 1.16$. Cluster members are determined using a combination of r-band magnitude cuts and Δz from the BCG. Redshift evolution is accounted for in this relation by the use of a variable $E(z)$, where

$$E(z) = \sqrt{\Omega_\Lambda + \Omega_m(1+z)^3}. \tag{2.2}$$

Finally, L_{500}, the total r-band luminosity within r_{500}, can be calculated and compared with M_{500} in order to produce a scaling relation between the two properties, and ultimately define a new cluster richness

$$R_{L*,500} = L_{500}E(z)^{1.40}, \tag{2.3}$$

as the optical mass proxy. We use these cluster properties from WH15 to obtain the characteristic velocity dispersion, σ_{500}, of each cluster, where

$$\sigma_{500} \equiv (GM_{500}/r_{500})^{1/2}. \tag{2.4}$$

The WH15 catalogue reports an uncertainty of 0.14 dex on M_{500} for the full cluster sample, which translates to an estimated uncertainty of 0.06 dex on r_{500}. As M_{500} values were calibrated using a combination of X-ray and SZ mass estimates from multiple surveys, systematic biases linked to any single mass proxy are minimised. Additionally, the richness-based mass scaling relation used in WH15 is explicitly corrected for redshift evolution, reducing the risk of systematic trends with redshift. While individual mass estimates may exhibit some scatter, the correlation between L_{500} and M_{500} (0.1–0.15 dex scatter) suggests that these variations are well understood and do not introduce significant biases. Since the work in this thesis relies on stacked cluster profiles, any stochastic variations in mass or r_{500} should average out, further mitigating the impact of systematics. Moreover, as WH15 derive M_{500} using an optical richness-based approach that does not preferentially select higher-mass clusters over lower-mass ones, no strong mass-dependent bias is expected in the scaling of profiles. These considerations indicate

that the adopted r_{500} values are robust and that systematic effects are unlikely to significantly impact the results.

This cluster catalogue is used in Chapters 3 to 5.

2.1.3 MPA-JHU

The MPA-JHU value-added catalogue (Brinchmann et al., 2004) is so-named for the collaboration between researchers from the Max Planck Institute for Astrophysics and John Hopkins University. It presents measurements of absorption line indices, emission line fluxes, stellar masses, star formation rates and gas-phase oxygen abundance determinations using the data from SDSS DR7 (Abazajian et al., 2009) Legacy survey.

This catalogue acts as a very useful source of galaxy stellar masses (Kauffmann et al., 2003a), as well as emission line data for the classification of SFGs and AGN in Chapters 3 and 4.

2.1.4 Wide-field Infrared Survey Explorer

The Wide-field Infrared Survey Explorer was an infrared space telescope launched into Earth's orbit by NASA in 2009. The science goal of WISE was to create infrared images of 99% of the sky in the wavelengths bands 3.4, 4.6, 12 and 22 μm. During its ten-month mission, the 40cm diameter IR telescope took 1.5 million images, which equated to one every 11 seconds. Each image covered a 47 arcminute field of view, with a resolution of 6".

In this thesis we utilise the infrared magnitude values collected in the allWISE survey catalogue (Wright et al., 2010) in order to classify AGN and SFGs in Chapters 3 and 4.

2.2 Methods & Techniques

In this section we will describe the common methods and techniques used across multiple projects throughout this thesis. The galaxy-cluster association process described in Section 2.2.3 is used in Chapters 3 to 5, but the remaining methods presented in Sections 2.2.1, 2.2.2, 2.2.4 and 2.2.5 are only used in Chapters 3 and 4.

2.2.1 Catalogue Matching and Stellar Mass Proxy Calculation

In Chapters 3 and 4, we combine data from the surveys described in Section 2.1 in order to create two master catalogues, which are then used to analyse how the fraction of galaxies identified as either SFGs or AGN changes with distance from the cluster centre.

The first master catalogue we have constructed comprises the spectroscopic galaxy catalogue from SDSS DR16, with additional data from the MPA-JHU value-added catalogue and the allWISE source catalogue matched by taking the closest source within 2" on the sky. The resulting catalogue contains over 3 million optically-identified galaxies with spectroscopic redshifts, for which 85% have WISE magnitude data, and 27% have emission line fluxes from MPA-JHU. This low fraction is due to the fact that MPA-JHU solely uses Legacy Survey data, and the SDSS DR16 catalogue used in this work is a cumulative catalogue, containing sources from all of the available SDSS surveys. As such, only 23% of sources in this catalogue have good stellar mass values from MPA-JHU, so we calculate a stellar mass proxy, M_i, for all galaxies in this sample based on their i-band magnitudes, i, using the best fit formula

$$\log_{10}(M_i) = -0.42i + 1.93, \tag{2.5}$$

which is an empirical formula we have derived by taking the scaling relation between the MPA-JHU sources with good stellar masses and their i-band magnitudes, as shown in Figure 2.1. Although this fit has significant scatter, it is entirely adequate for the purposes of this work.

This catalogue will hereafter be referred to as *SDSS galaxies*. The second master

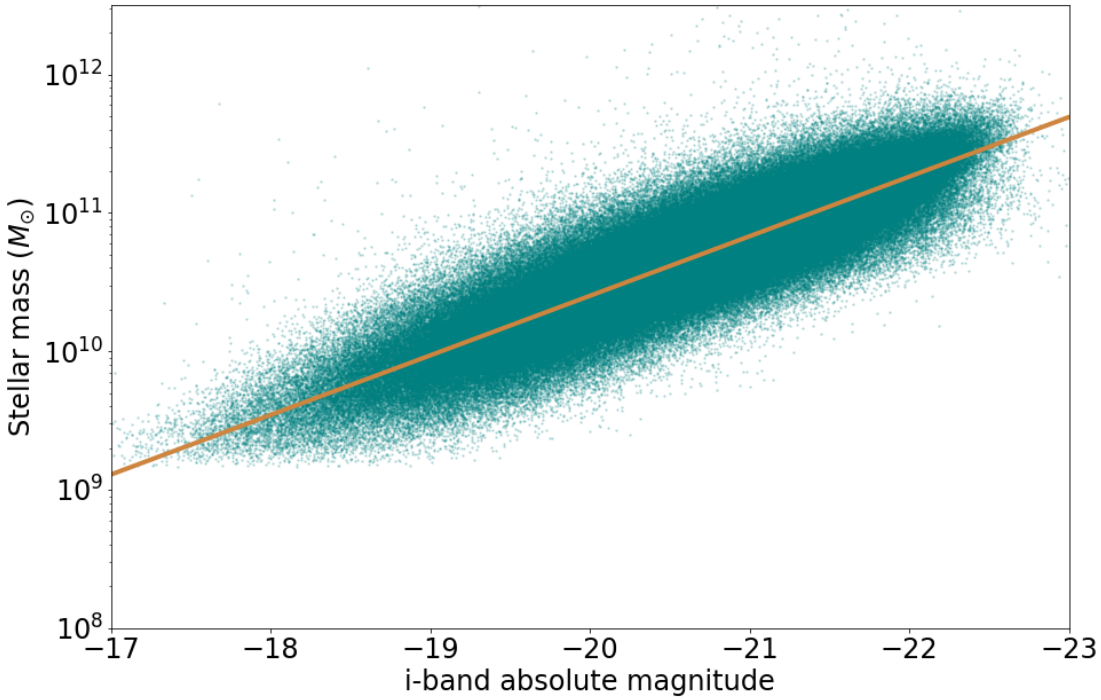

Figure 2.1: The relationship between the i-band absolute magnitudes and stellar masses in the *SDSS galaxies* catalogue. The orange line of best fit shown is the empirical relation described by Equation (2.5).

catalogue we derive, *radio galaxies*, comprises the radio sources from LoTSS DR2 matched within 2" on the sky to *SDSS galaxies*. We choose 2" as we find empirically that, conducting a nearest neighbour match of the two catalogues, the vast majority of sources match to each other within this distance.

SDSS galaxies, *radio galaxies* and the WH15 cluster catalogue are further limited to the same region of sky and the redshift range $0.05 < z \leq 0.2$. We implement a lower redshift limit of $z > 0.05$ as nearby radio galaxies are resolved into multiple emission regions due to LoTSS's 6" resolution. This feature means that, below this lower limit, we are unable to match a single LOFAR source with a single optical galaxy. The upper redshift limit at $z = 0.2$ is implemented to minimise issues arising from completeness and galaxy evolution, as lower luminosity galaxies become less detectable at higher redshifts, making higher redshift samples more biased towards only containing brighter, more massive galaxies.

2.2.2 Classification of SFGs and AGN

In order to extract the sub-samples of SFGs and AGN from all sources of emission in *radio galaxies*, we follow Sabater et al. (2019, hereafter S19) and Herpich et al. (2016) by using a simple WISE colour cut at $W2 - W3 = 0.8$. S19 showed that this colour cut is effective at separating SFGs and AGN. We therefore adopt this singular diagnostic method to classify the radio-identified SFGs and AGN in this sample, which will hereafter be referred to as *radio SFGs* and *radio AGN* respectively.

We choose this diagnostic for several reasons. Firstly, S19 show this classification method to be surprisingly robust when overlaying the final combined classification of each source onto each of their diagnostic diagrams. Secondly, emission line data is not available from MPA-JHU for every radio source in our sample, whereas WISE data is, and so we opt to primarily use the WISE colour diagnostic in order to maintain as large a sample as possible, whilst still retaining a good level of purity.

However, in order to check that the results found in Chapters 3 and 4 are not due to this choice of AGN/SFG classification, we take a smaller test sample of *radio*

AGN that satisfies not just the WISE colour diagnostic, but also the "D_{4000} vs. L_{150MHz}/M_*" method developed by Best et al. (2005b), and the "BPT" diagnostic developed by Baldwin et al. (1981), both of which are also presented in Sabater et al. (2019). We find that the results with this smaller, stricter sample are largely consistent with the results seen in Chapter 4 from the purely WISE colour-cut sample, and thus we can be confident that any trends are not due to the diagnostic method.

We calculate the SFRs, ψ of *radio SFGs* following the SFR-L_{150} relation outlined in Smith et al. (2021),

$$(1.058 \pm 0.007) \log_{10}(\psi/M_{\odot}\mathrm{yr}^{-1}) = \log_{10} L_{150\mathrm{MHz}} - (22.221 \pm 0.008), \qquad (2.6)$$

where $L_{150\mathrm{MHz}}$ is the radio luminosity at 150MHz. Specific star formation rates (sSFR) for *radio SFGs* are then given by ψ/M_i. The minimum sSFR for the *radio SFGs* sample is 4×10^{-12} yr^{-1}.

To ensure that the *radio SFGs* and *radio AGN* samples are directly comparable to *SDSS galaxies* in their mass limits at all redshifts, we divide the *radio SFGs* and *radio AGN* samples into redshift bins of width 0.01, and apply a lower mass threshold that cuts off at 95% of each bin's sample size. We then apply the respective threshold to *SDSS galaxies*, depending on whether we are analysing the *radio SFGs* sample or the *radio AGN* sample. This cut corresponds to a lower mass limit range of (0.6–6.3)$\times 10^{10} M_{\odot}$ for *radio SFGS*, and (0.2–1)$\times 10^{11} M_{\odot}$ for *radio AGN*, across the $0.05 < z \leq 0.2$ redshift range. This process results in sample sizes of 50 516 *radio SFGs* and 213 072 *SDSS galaxies* when doing the SFG analysis, and 12 380 *radio AGN*, and 141 586 *SDSS galaxies* when doing the AGN analysis. We show examples of these cuts in Figure 2.2 for the analysis of SFGs done in Chapter 3.

2.2.3 Galaxy-Cluster Association

To quantify each galaxy's relationship to a cluster environment, we associate objects in *SDSS galaxies* and *radio galaxies* with the closest cluster in the WH15 cluster catalogue by following a similar method to that used in Garon et al. (2019).

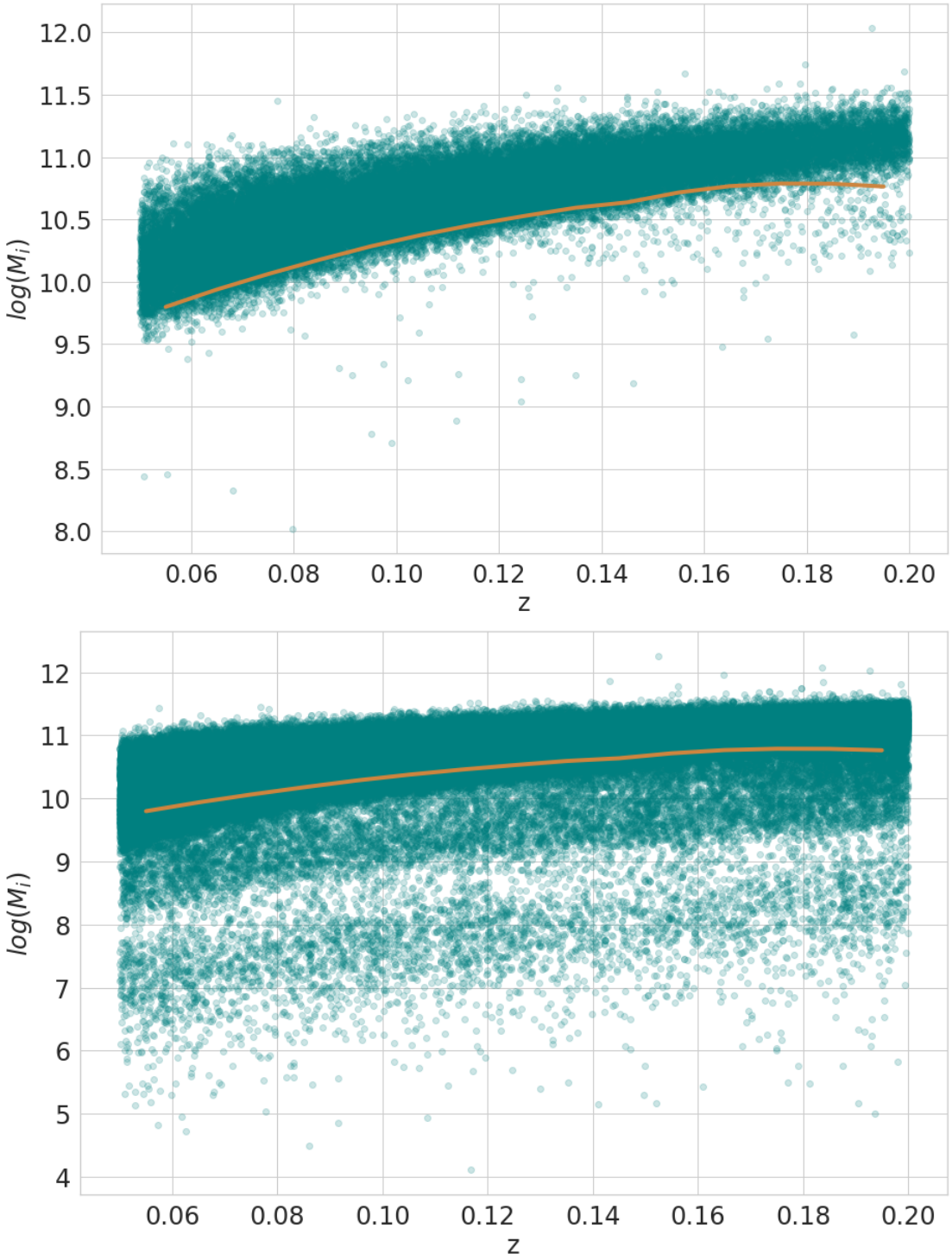

Figure 2.2: The distribution of i-band stellar masses with respect to redshift for the *radio SFGs* catalogue (*top*) and the *SDSS galaxies* catalogue (*bottom*). The orange line shows the described lower mass limit range based on 95% of each redshift bin's sample size from the *radio SFGs* sample, which is also applied to the *SDSS galaxies* sample. All sources below this line are removed.

For each individual cluster at redshift z_{clus}, we identify the galaxies associated with that cluster using the formula

$$\frac{|z_{gal} - z_{clus}|}{1 + z_{gal}} < 0.04, \tag{2.7}$$

where z_{gal} is the galaxy redshift, and the threshold of 0.04 taken here is from Garon et al. (2019); Wen & Han (2015), and chosen due to the excess of cluster-associated sources within this range. Of these remaining galaxies, only those within a radially projected distance on the sky of $< 50r_{500}$ are matched to the cluster. At this preliminary stage, some objects are matched to multiple clusters, and the redshift range is large enough to include sources that may not actually be associated with their prescribed cluster. There is no way to determine for individual objects with which cluster they are most closely associated, but the process described in the following Section (Section 2.2.4) allows us to resolve these issues statistically.

Finally, only entries in the WH15 cluster catalogue with spectroscopic redshifts are kept, in order to avoid photometric uncertainty when matching galaxies and clusters.

2.2.4 Background Subtraction

Since the density of galaxies physically associated with a cluster decreases with radius, the membership assigned in Section 2.2.3 will see increasing relative contamination with radius. It is not possible to determine which individual galaxies are truly associated with each cluster, but we can correct for this contamination statistically. In order to assess the level of contamination, we analyse the phase spaces for *SDSS galaxies*, *radio AGN*, and *radio SFGs* individually, the last two of which are shown in Figure 2.3. In order to combine data from multiple clusters, each galaxy's distance from their host cluster and velocity is scaled by their associated cluster's r_{500} and characteristic velocity, σ_{500}, respectively.

It is clear from Figure 2.3 that there is a signal of correctly-associated galaxies lying within the characteristic velocity range of $v = \pm 2\sigma_{500}$, but this signal becomes significantly contaminated outside of $\sim R_{500}$. By slicing this phase space up into logarithmically-spaced radial bins, we are able to ascertain the level of line-of-sight

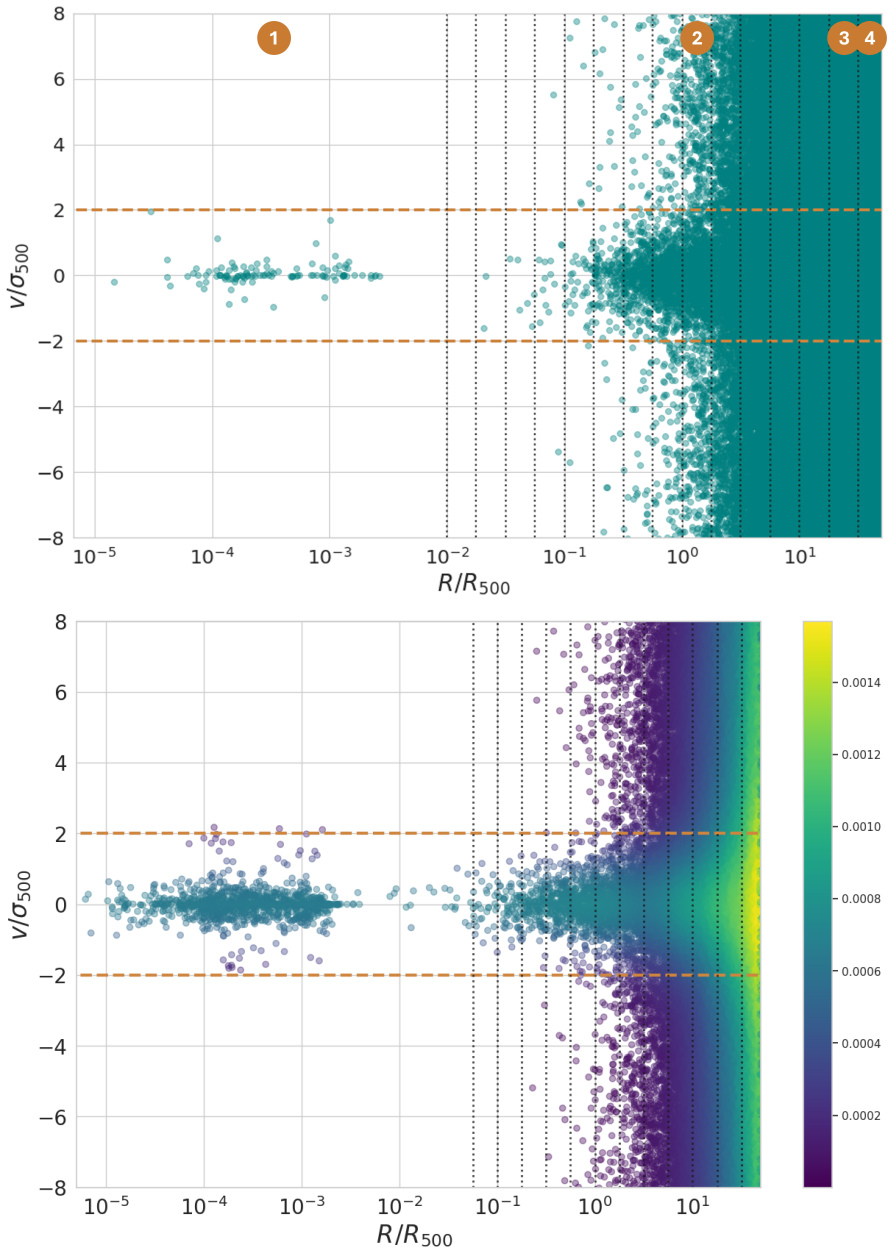

Figure 2.3: The projected phase-space distribution (showing line-of-sight velocity versus projected separation) for *radio SFGs* (*top*) and *radio AGN* (*bottom*) out to $50r_{500}$. The orange, horizontal, dashed lines at $v = \pm 2\sigma_{500}$ indicate the limits of velocity associated with the cluster, and the black, vertical, dotted lines indicate the cluster radius slicing used to determine the line-of-sight contamination in each annulus bin. The numbered, orange circles in the *top* figure correspond to the histogram bins shown in Figure 2.4, and the variation in colour amongst the scatter in the *bottom* figure shows the Gaussian kernel density estimation, the values of which are given by the colour bar.

contamination in each individual annulus, as illustrated in Figures 2.4 and 2.5.

In each bin, the line-of-sight contamination is determined using the mean of the number of galaxies outside of $v = \pm 2\sigma_{500}$, as indicated by the horizontal line in Figures 2.4 and 2.5. There is a slight difference in background level on the two sides of the cluster $v = \pm 2\sigma_{500}$ region due to the variation in completeness with redshift, so we take the average to define the background contamination at the cluster's redshift. This value is subtracted from the number of cluster-associated galaxies within $v = \pm 2\sigma_{500}$ to give the background-subtracted signal in each annulus. These values are then divided by the annulus area to give the projected number density, $N(R)$, for each radial bin, where R is the projected distance from the cluster centre. Finally, we take the error on the projected number density in each annulus to be the Poisson error, and adopt the field value, $N_f(R)$, to be the sum of the projected number density of background galaxies within all annuli.

It is interesting to note that this cluster-associated signal seen in Figure 2.4 remains statistically-significant out to the penultimate radial bin at more than $30R_{500}$, which for a typical cluster in this sample is more than 20 Mpc. This finding confirms that the overdensity of galaxies associated with a cluster extends to many times the virial radius.

2.2.5 Abel Inversion

The quantities that we derive in Section 2.2.4 measure projected densities on the plane of the sky, $N(R)$, but these quantities are intrinsically diluted towards the centre of the cluster due to projection. To determine more intrinsic physical quantities, we need to de-project these values into volume densities. Since the process of stacking many clusters together averages out any asymmetries in structure, we can assume spherical symmetry in the density profiles, so the projected densities can be straightforwardly converted to spatial density via an Abel inversion, using

$$n(r) = -\frac{1}{\pi}\int_r^\infty \frac{dN}{dR}\frac{1}{(R^2 - r^2)^{\frac{1}{2}}}dR, \tag{2.8}$$

where $n(r)$ and r are the de-projected number density and radial distance respectively, and $N(R)$ and R are the projected equivalent variables. In the numerical

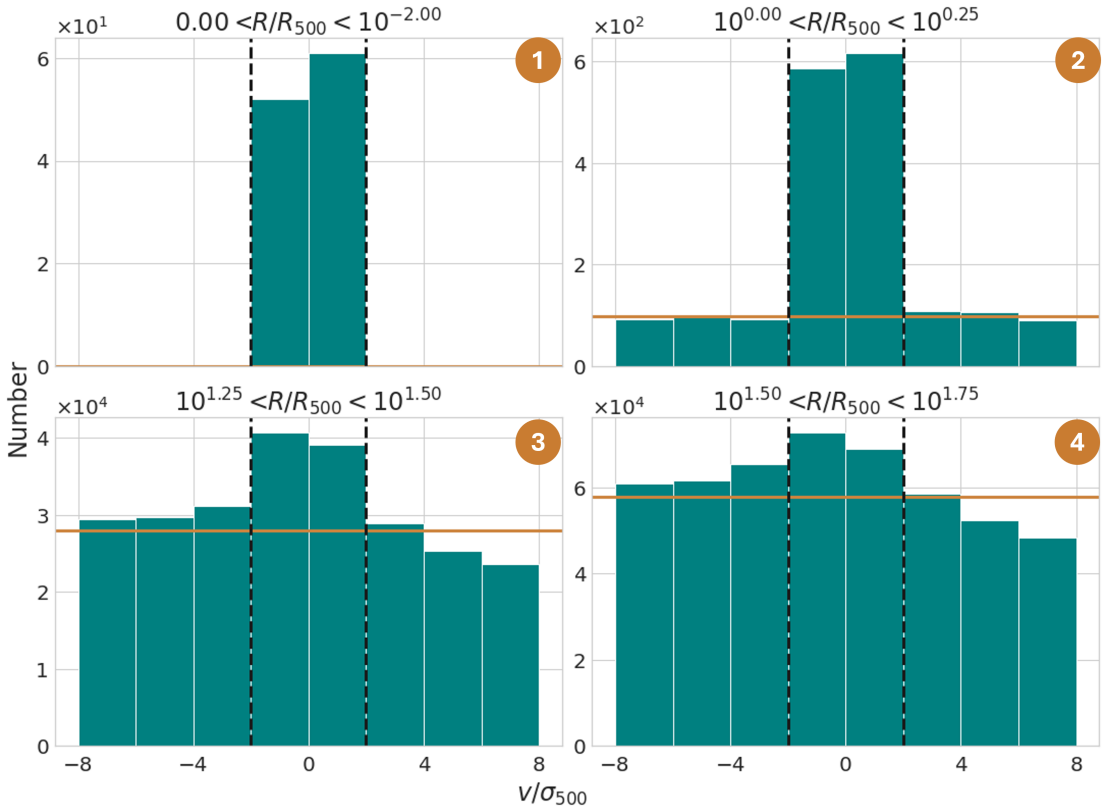

Figure 2.4: The line-of-sight velocity of galaxies within four of the logarithmically-spaced annuli from the *top* panel of Figure 2.3. Galaxies within the black, vertical, dashed lines (indicating the characteristic velocity range $v = \pm 2\sigma_{500}$) are deemed to be correctly associated with their host cluster, and those outside are identified as contaminants. The orange, horizontal, solid line shows the mean of the background contamination in each bin, and the numbered, orange circles correspond to the annulus bins shown in the *top* panel of Figure 2.3.

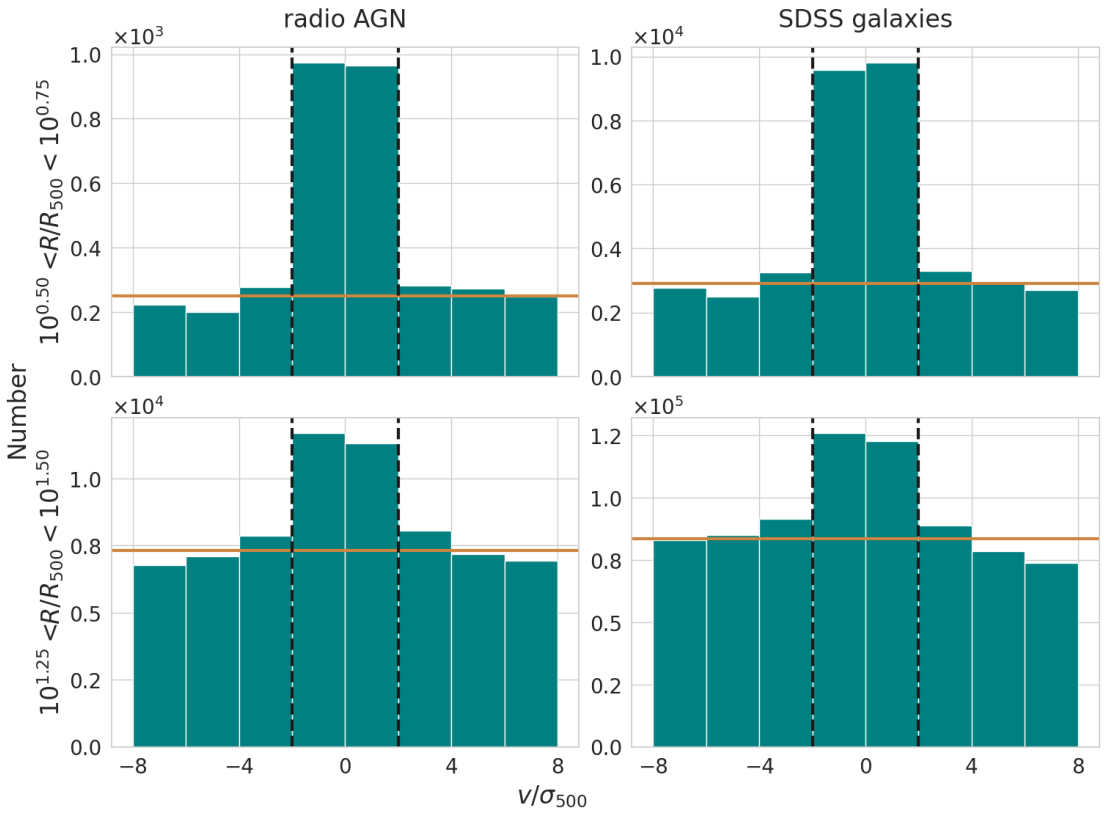

Figure 2.5: The line-of-sight velocity of galaxies within two of the logarithmically-spaced annuli from the phase spaces of *radio AGN* (*left*) and *SDSS galaxies* (*right*). Galaxies within the black, vertical, dashed lines (indicating the characteristic velocity range $v = \pm 2\sigma_{500}$) are deemed to be correctly associated with their host cluster, and those outside are identified as field galaxies. The orange, horizontal, solid line shows the mean of the background contamination in each bin.

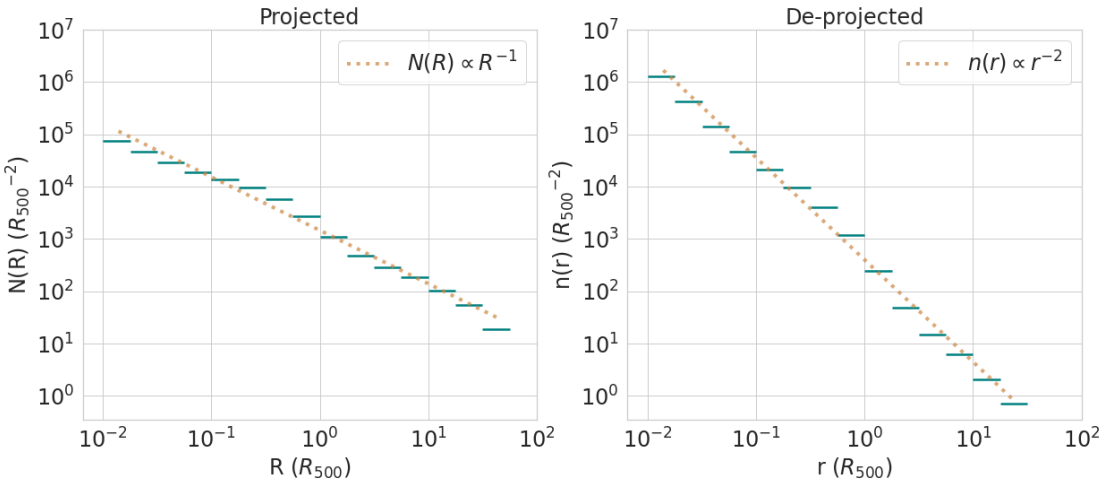

Figure 2.6: The projected and de-projected (via an Abel inversion) number density distributions of *SDSS galaxies*, with respect to cluster radius. The dotted lines show the power laws that fit to these distributions.

implementation of this quadrature, the value in the outermost bin considered is indeterminate. Fortunately, here we can use the overall average field value from the entire survey as a boundary condition at this point. The imposition of this constraint has the desirable effect of suppressing the error amplification inherent in such a de-projection. Finally, we can calculate errors on the de-projected distributions by applying a Monte Carlo method that resamples the projected data using their Poisson errors.

By way of illustration, Figure 2.6 shows the projected number density profile of the full *SDSS galaxies* sample with projected distance from their associated cluster, and the numerical implementation of the Abel inversion, which yields the variation in number density with radius. As previously noted by Beers & Tonry (1986), the projected number density of galaxies around clusters follows an approximate power law of $N(R) \propto R^{-1}$. The numerically-derived inversion yields a number density in good agreement with the analytic solution to Equation (2.8) that exists in this case, given by $n(r) \propto r^{-2}$. This overall power law agrees well with the general profile determined by Beers & Tonry (1986).

Chapter 3

Local versus Global Environment: the Suppression of Star Formation in the Vicinity of Galaxy Clusters[1]

3.1 Introduction

There has long been evidence to suggest a strong correlation between the star formation rate of a galaxy, and the density of the environment in which it lives (Oemler, 1974; Davis & Geller, 1976; Dressler, 1980; Dressler & Gunn, 1983; Postman & Geller, 1984; Balogh et al., 1997; Poggianti et al., 1999; Peng et al., 2010). Star-forming galaxies are seen more commonly in lower-density field environments, and quiescent galaxies are more commonly seen in denser environments such as groups or clusters. This observation is often referred to as the SFR-density relation, and emphasises the importance of environmental effects on the processes that drive galaxy evolution.

This relation strongly suggests that a galaxy's transition from a low-density environment into a high-density one involves external physical processes that reduce or even extinguish entirely the star-formation within a galaxy, which is a process

[1]This work is published in: *de Vos, K., Merrifield, M. R., & Hatch, N. A. 2024, MNRAS, 531, 4, 4383, 10.1093/mnras/stae1403*

known as quenching. However, there are many suggested external mechanisms that contribute to quenching, and it is likely that various combinations of them are responsible for shutting down the star formation in a galaxy, depending on the environments that a galaxy encounters throughout its life. These various phenomena include: "strangulation" or "starvation", which is the process by which a galaxy is no longer able to accrete cold gas onto its disk, thereby preventing any further star formation from occurring (Larson et al., 1980); ram pressure stripping, whereby a galaxy's cold, star-forming gas is pushed out due to the relative velocity difference between its host galaxy and the hot, dense, virialised gas of the medium surrounding it (Gunn & Gott, 1972; Abadi et al., 1999); "harassment", which are tidal interactions disruptive to star-formation, caused by the gravitational pull of other nearby galaxies in high density environments (Farouki & Shapiro, 1981; Moore et al., 1996); and galaxy mergers, which have a similar effect (Makino & Hut, 1997; Angulo et al., 2009; Wetzel et al., 2009a,b; White et al., 2010; Cohn, 2012).

Additionally, a galaxy's star-formation may be affected before even arriving at a cluster, during the period within which it is travelling towards a cluster along filaments or in groups. This effect is know as pre-processing, and is the means by which a galaxy experiences quenching prior to crossing the virial radius, due to quenching mechanisms associated with higher density local environments than the field. Pre-processing is thought to be a large contributor to the high proportion of quiescent galaxies in clusters (Zabludoff & Mulchaey, 1998; McGee et al., 2009), and could be an explanation for some of the observed timescales that suggest quenching starts prior to infall (Wetzel et al., 2013; Haines et al., 2015; Werner et al., 2021).

There is a great deal of literature that investigates quenching processes for infalling satellite galaxies out to $\sim 2-5R_{200}$ (Balogh et al., 1998; Lewis et al., 2002; Bahé et al., 2013; Wetzel et al., 2014; Haines et al., 2015; Bianconi et al., 2018; Pintos-Castro et al., 2019; Lacerna et al., 2022; Baxter et al., 2022; Salerno et al., 2022; Hough et al., 2023; Kesebonye et al., 2023; Rihtaršič et al., 2024; Lopes et al., 2024), and any radii further than this distance is commonly considered the field. However, Haines et al. (2015) found that the fraction of galaxies that are star-forming still had not reached the observed field fraction by $3R_{200}$, suggesting that the influence of the cluster outskirts on the star-forming properties of galaxies

must extend further. More recently, Lopes et al. (2024) have shown that quenching begins as far out as $5R_{200}$ from the cluster centre, and that group galaxies have an undeniably lower fraction of SFGs than isolated galaxies, which provides strong evidence for pre-processing.

To extend this analysis, we corroborate and expand on these exciting new results: we investigate this transitionary region in the far cluster outskirts in order to further quantify the distance from the cluster centre that the SFG fraction starts to deviate from the SFG field fraction value. In addition, we investigate the effects of both intrinsic and external galaxy properties on the SFG fraction by measuring the influence of both stellar mass and distance to nearest neighbour, in order to determine the various mechanisms that could be influencing quenching at the distances seen. In Section 3.2, we present the data and method used in addition to those described in Chapter 2, while Section 3.3 presents the resulting fractional distributions with respect to cluster-centric radius, and discusses the various possibilities for the physical mechanisms responsible for them. Finally, in Section 3.4, we summarise the somewhat surprising results.

3.2 Data & Methods

In order to conduct this study, we utilise the data and methods described in Chapter 2, exclusively using the 50 516 *radio SFGs* identified from LoTSS DR2 (Shimwell et al., 2022), and the 213 072 *SDSS galaxies* compiled from SDSS DR16 (Ahumada et al., 2020), MPA-JHU (Brinchmann et al., 2004), and the allWISE survey catalogue (Wright et al., 2010). The work presented here also requires a nearest neighbour matching method which is unique to this chapter, and so we outline this method below.

In order to determine a measure of the local environment of each galaxy, we conduct a nearest neighbour matching process. To minimise line-of-sight contamination, we restrict the search for neighbours to galaxies that were assigned to the same cluster (as outlined in Section 2.2.3). This method is implemented by conducting an on-sky match of the *SDSS galaxies* to themselves for each galaxy's 3rd, 5th and 10th nearest neighbour. The angular offset, θ, between each galaxy

and its nearest neighbours is then used to calculate the physical on-sky distance between them, using $d_{nn} = \theta D$, where D is the angular diameter distance found using each cluster's redshift. These same nearest neighbour distances are then applied to the matched galaxies in *radio SFGs*. One concern might be that some of these distances are distorted by edge effects in the survey, but we find that the impact is negligible out to beyond $40R_{500}$, which lies at the largest radii considered in this study (see Section 2.2.4).

In the subsequent analysis, we use d_{5nn}, the distance to the 5th nearest neighbour, but the results are qualitatively similar for d_{3nn} and d_{10nn}.

3.3 Results

3.3.1 Total SFG Fraction

Using the two catalogues described in Section 2.1, *SDSS galaxies* and *radio SFGs*, we can determine how the fraction of galaxies that are star-forming changes with respect to distance from the centre of the associated cluster. This projected fraction is shown in Figure 3.1, where $F_{SF,all} = N_{SF}/N_{SDSS}$, and N_{SF} and N_{SDSS} are the projected number densities of *radio SFGs* and *SDSS galaxies*, respectively. We defined the field value, $N_f(R)$ in Section 2.2.4, to be the sum of the projected number density of background galaxies within all annuli. The field values of both *radio SFGs* and *SDSS galaxies* are used to calculate the SFG field fraction using the formula $F_{SFG,f} = N_{SFG,f}/N_{SDSS,f}$. This value is also shown in Figure 3.1, but it is worth noting that *radio SFGs* only comprises 21% of *SDSS galaxies*, as opposed to the $\sim 60\%$ (Dressler, 1980) seen when selecting SFG samples via H-α emission. This difference reflects the higher threshold that these radio data place on the detection of star formation. Since all of the comparisons in this work are made relatively using this threshold, it has no impact on any of the results obtained.

It is immediately apparent from this figure that there is a steady decline in the fraction of SFGs with decreasing radius which starts at least $10R_{500}$ from the cluster centre, if not further. Since projection has the effect of combining data from

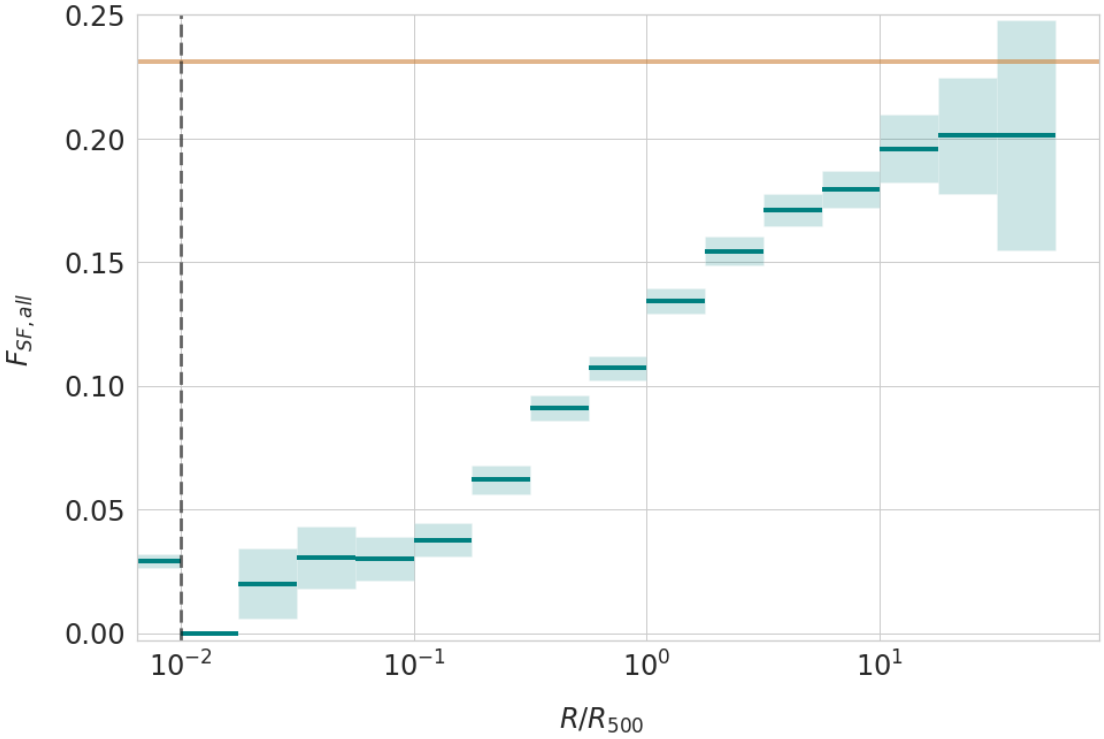

Figure 3.1: The projected distribution of the fraction of galaxies identified as star-forming, with respect to cluster radius. The orange, horizontal, solid line is a measure of the field fraction of SFGs (see Section 2.2.2), and the black, vertical, dashed line represents the radius at which everything within is considered to be the very centre of the galaxy cluster. This inner bin includes all galaxies between $0 < r < 0.01R_{500}$.

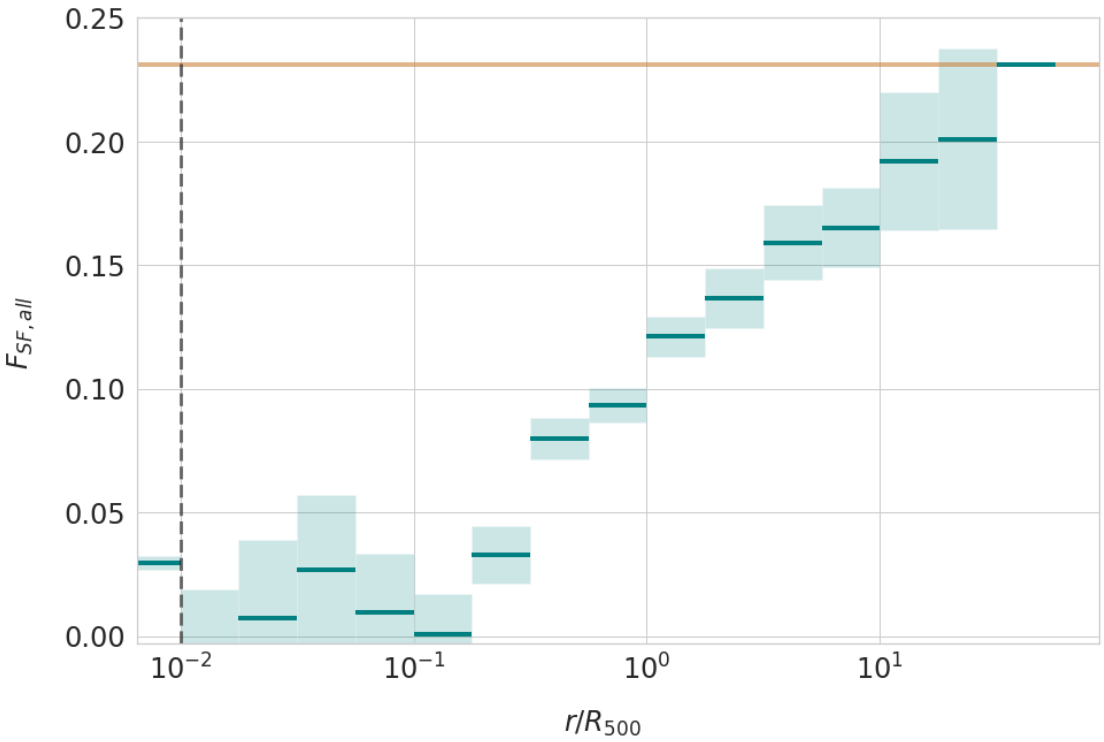

Figure 3.2: The de-projected distribution of Figure 3.1.

a range of radii, this plot will tend to average away some of the true variation with radius. Indeed, the Abel-inverted spatial density presented in Figure 3.2 shows an even more dramatic decline in the star-forming fraction, which reaches zero within the central $0.1R_{500}$. For the remainder of this chapter we therefore generally only present the de-projected results as representative of the intrinsic properties of the systems, and due to the small sample size of any SFGs in annuli $< 10^{-0.75}R_{500}$, we make the decision to only investigate how the SFG fraction changes for galaxies at radii of $> 10^{-0.75}R_{500}$ for the remaining analyses.

At the large radii of $\sim 10R_{500}$ where the fraction of SFGs starts to drop, we are unlikely to be seeing cluster members or even the "backsplash" galaxies that have recently fallen through the cluster and have yet to virialize, as these objects seldom travel more than $\sim 3R_{500}$ from the cluster centre (Haggar et al., 2020). Thus the decrease in star-forming galaxies does seem simply to reflect the properties of galaxies on their first infall onto the cluster. To investigate what the driving mechanism for this transition might be, we next explore whether it is driven by an internal property such as the galaxy's mass, or an external one like the local

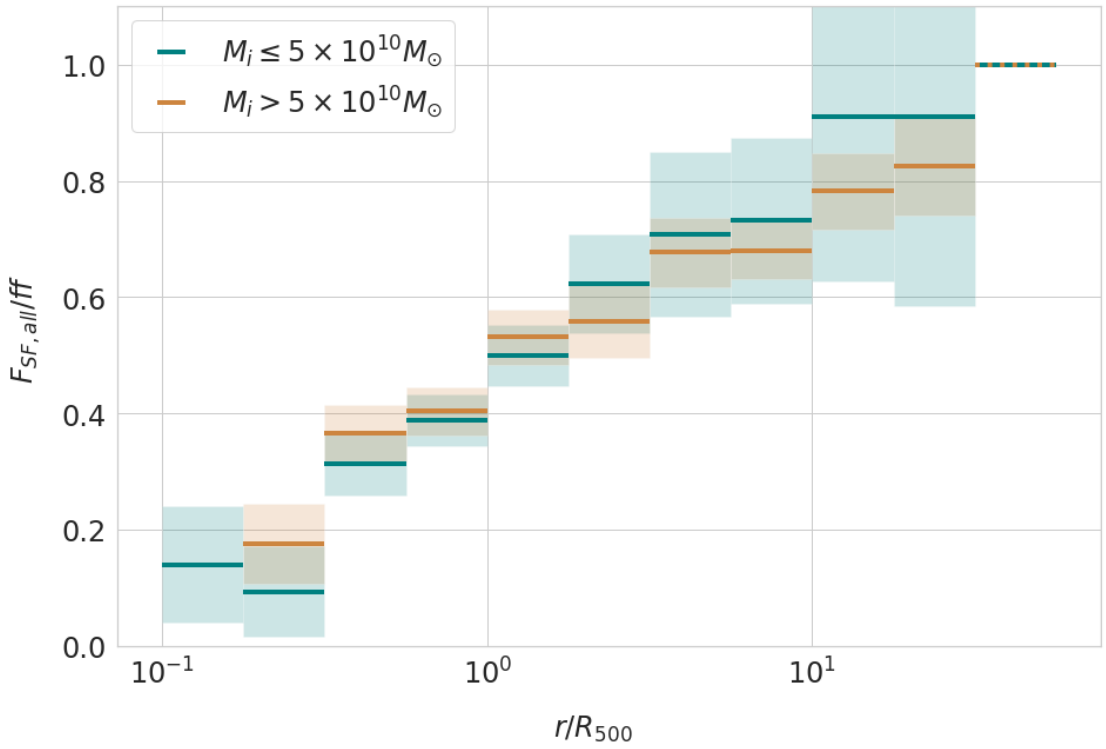

Figure 3.3: The de-projected distribution of the fraction of SFGs that fall into the two mass bins either side of $M_i = 5 \times 10^{10} M_\odot$, normalised by their respective field fractions: 0.24 for the low mass bin, and 0.19 for the high mass bin.

density around the galaxy.

3.3.2 Stellar Mass

In order to quantify any dependence on the mass of the galaxy, we split both samples - *radio SFGs* and *SDSS galaxies* - into two roughly equally-sized bins at the stellar mass value $M_i = 5 \times 10^{10} M_\odot$, and determine how the fraction of SFGs in each sub-sample varies with cluster-centric radius. There is a lower fraction of high-mass SFGs than low-mass SFGs, therefore in order to easily compare the difference in the two distributions, each fraction is normalised by its field fraction value, which is 0.24 for $M_i \leq 5 \times 10^{10} M_\odot$ and 0.19 for $M_i > 5 \times 10^{10} M_\odot$. The resulting radial profiles are presented in Figure 3.3.

Immediately, we see that the decline still begins at very large radii for both mass populations, suggesting that the distribution seen in Figure 3.2 is not being dom-

inated by one mass population over another. On closer inspection, we notice that there are slight differences in the two sample distributions, an example being that the gradient for the decline of the low-mass sample appears slightly steeper and starts declining later than the high-mass sample. However, as these slight differences are within errors and therefore not statistically significant, it is hard to draw any concrete conclusions from these minor distinctions. As such, we conclude that the mass of the galaxy does not seem to be a significant factor in determining how or why star-formation is being suppressed at such large radii. We therefore now turn to local environment, to see if this can be held responsible.

3.3.3 Local Environment

In order to investigate how the local environments of SFGs affect their fractional distribution with respect to cluster radius, we separate *radio SFGs* into six bins based on each galaxy's distance to its 5th nearest neighbour, d_{5nn}. This parameter d_{5nn} is defined such that higher values correspond to lower local densities, and vice-versa.

When dividing the data into so many bins, the noise-amplifying effects of the Abel inversion become significant, so in this case we present both the observed projected distributions (Figure 3.4) and the de-projected physical quantities (Figure 3.5). We also present the results as both profiles for individual density bins in which the size of the uncertainty is explicitly presented (right panels) and as a two-dimensional tile plot of radius and local density, which gives a clearer overall impression of how the star-forming fraction depends on both variables (left panels). Comparing these two figures, it is clear that the main features seen are not artefacts of the de-projection process.

When analysing the right-hand plots of these figures, we see a largely flat distribution in the high density local environment bins that gradually steepens into a declining distribution as density decreases. The higher local density distributions also have a lower field SFG fraction, which increases with decreasing density.

The combination of these results can be interpreted as follows: SFGs that become part of higher density regions such as groups and filaments in the galaxy cluster

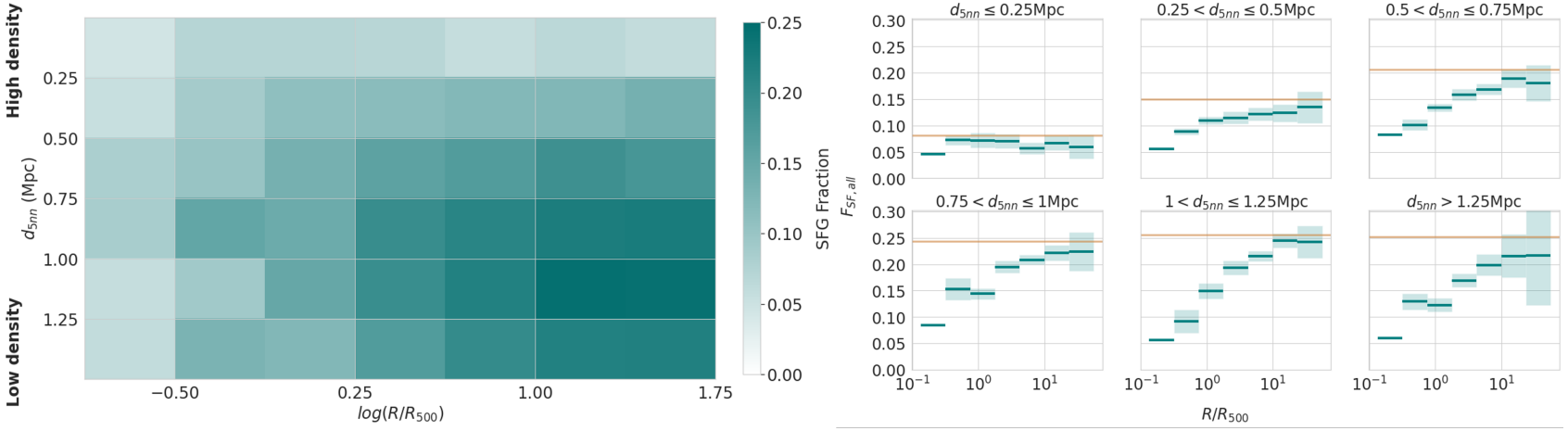

Figure 3.4: *Left:* The projected tile distribution of the fraction of galaxies identified as star-forming, with respect to the distance to the 5th nearest neighbour galaxy and the R_{500}-normalised distance from the cluster centre. *Right:* The associated projected distributions of the fraction of galaxies identified as star-forming with respect to cluster radius, binned by the distance to the 5th nearest neighbour galaxy. The horizontal, orange lines are a measure of the field fraction for each bin. Each subplot equates to a row in the left-hand tile plot.

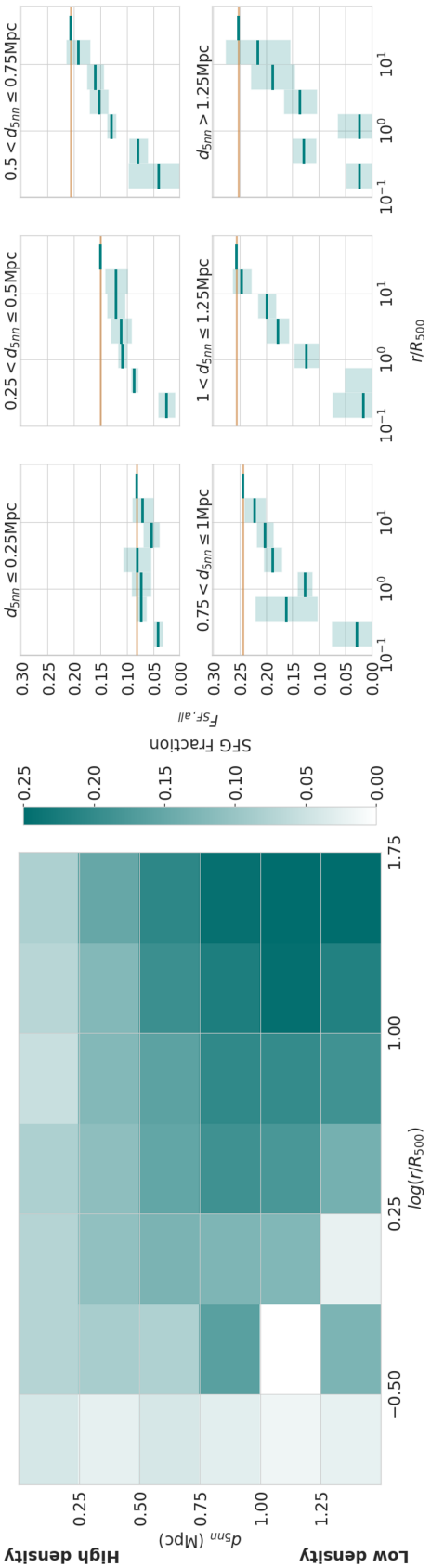

Figure 3.5: The de-projected distributions of Figure 3.4.

outskirts undergo pre-processing which quenches some, but not all SFGs (Zabludoff & Mulchaey, 1998; McGee et al., 2009). This suppression of star-formation results in a lower overall SFG fraction in these types of local environments, but those environments then appear to host a flatter distribution with radius than that seen in the lower density local environments too. This smaller variation with radius implies that higher density local environments shield their surviving SFGs from any global environment mechanisms that are responsible for the declining trend we see in lower density bins, perhaps because the inter-galaxy medium is dense enough to deflect gas associated with the cluster from further stripping cold, star-forming gas from these objects, thus resulting in the flattened distribution. This potential shielding would be less and less effective at lower densities which explains the gradual steepening seen as local environment density decreases.

These trends are also apparent in the left panels of Figures 3.4 and 3.5, with the extra information that we can more readily compare the absolute value of the SFG fraction at different local densities. It is apparent from these plots that the chances of a SFG surviving during its infall into a cluster is a balance of two factors: at high local densities, pre-processing by this local environment quenches most SFGs; at low local densities, the influence of the cluster starts to win out at larger radii, also quenching SFGs; so it is at intermediate local densities that the fraction of SFGs stays high to the smallest radii. However, in all cases eventually the cluster wins, quenching almost all SFGs at small radii, irrespective of their local environment (Choque-Challapa et al., 2019; Haggar et al., 2023).

Having found this interplay between local and global environment, the remaining question is whether the protection afforded by the local environment depends on the intrinsic property of the mass of the galaxy in a subtle way that wasn't apparent when we just considered galaxy mass in Section 3.3.2.

3.3.4 Stellar Mass vs Local Environment

Finally, we analyse how the variation in radial distribution that we see when binning by local environment density, might also be mass-dependent. We conduct this test separating both of the *radio SFGs* and *SDSS galaxies* samples into four bins, split by low and high stellar mass either side of $M_i = 5 \times 10^{10} M_\odot$, and low

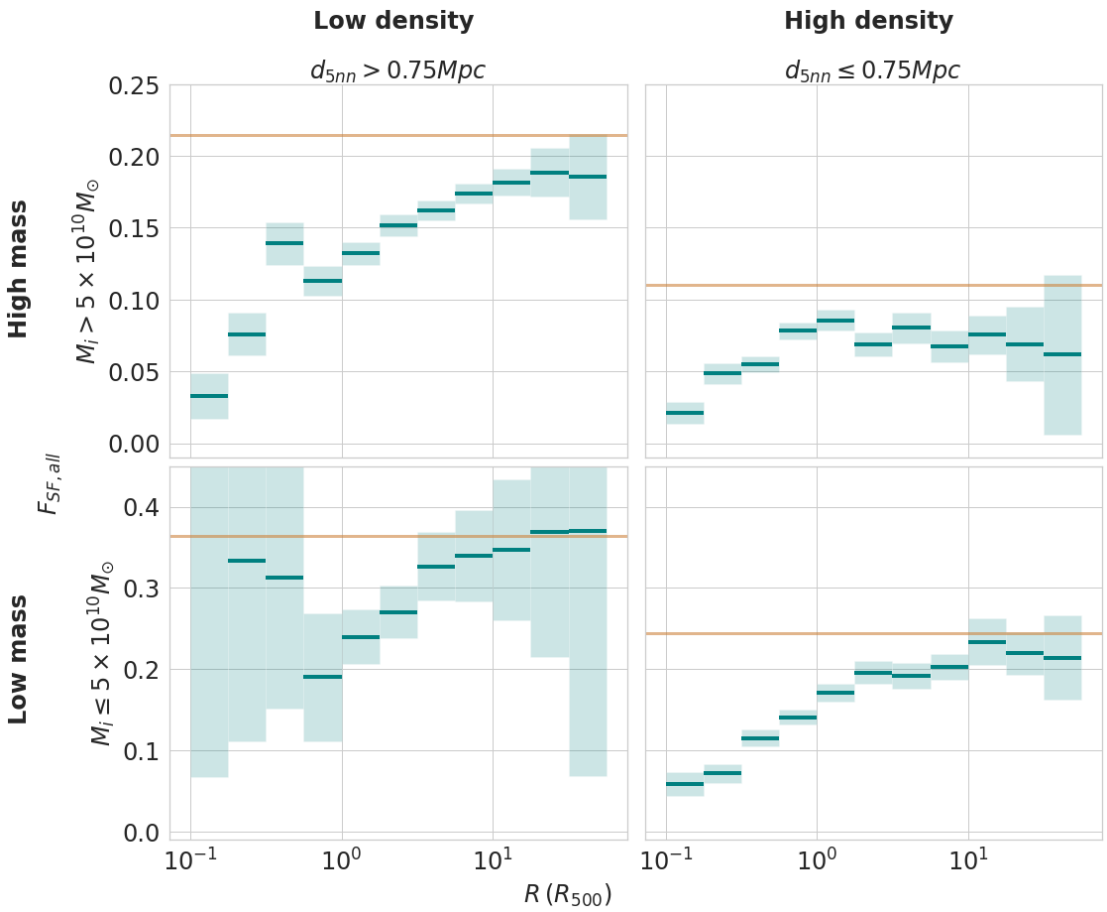

Figure 3.6: The projected distribution of the SFG fraction, binned by both M_i and d_{5nn}. The binning boundaries are given by $M_i = 5 \times 10^{10} M_\odot$ and $d_{5nn} = 0.75$Mpc, and the horizontal, orange lines are a measure of the field fraction for each bin.

and high local environment density either side of $d_{5nn} = 0.75$Mpc. The results of this analysis are shown in Figure 3.6. As in Section 3.3.3, we show the projected distribution here, but very similar results are seen in the de-projected distributions.

We find declining cluster-centric SFG fractions similar to the trends seen in Figures 3.1 and 3.2 in both of the low-density subsamples. The high-density, high-mass sample, however, exhibits a flat distribution at large radii, down to $\sim 1 R_{500}$. The final subsample of high-density, low-mass galaxies shows a similar trend to that seen for its high-mass counterpart, but is somewhat less clear-cut and could therefore also be interpreted as a shallow decline. This distinction suggests that the flattening of the cluster-centric SFG fraction exhibited in the high local environment density plots of Figures 3.4 and 3.5 is predominantly driven by the

subsample of higher mass galaxies, and to a lesser extent by lower mass galaxies.

Looking at Figure 3.6, one interpretation may be that the lower fraction of massive (and possibly also low-mass) SFGs that are able to continue forming stars – despite the pre-processing effects of their higher local density – are then protected from further loss of star formation due to the approaching cluster, by that same denser local environment. This protection appears to hold until $1R_{500}$, at which point the SF fraction decline begins again – presumably, past this point the defence provided by a higher-density local environment is not enough to shield its remaining SFGs from quenching. This subtle effect was hidden in Figure 3.3 when the samples were only divided by stellar mass and local environment was not considered. In this more nuanced analysis, however, we see that the stellar mass of a galaxy *does* impact the effectiveness of the global environment on galaxy quenching, but only when the galaxy resides in a particular dense local environment.

3.4 Summary & Discussion

Through this analysis, we show that there is a consistent and persistent trend displaying a decline in the SFG fraction with decreasing cluster-centric radius, that begins by at least $10R_{500}$ from the cluster centre - even further than the $5R_{200}$ ($\sim 7R_{500}$) found in the recent, similar results of Lopes et al. (2024). We interpret this decline as the quenching of the SFG population prior to infall into a cluster, as the large radius at which this decline begins is too far out to be explained by backsplash galaxies, which only travel out to $\sim 3R_{500}$ at most (Haggar et al., 2020). In order to determine what might be driving this decline in the SFG fraction, we investigate how the radial distribution is affected when binning by stellar mass, distance to nearest neighbour (local environment density), and a combination of both.

When binning by stellar mass, we find that both populations still experience this same decline at large radii, past $10R_{500}$, and experience very little difference in the gradient of their decline. It is noted that there is – unsurprisingly – a lower fraction of high mass SFGs than low mass ones, but the gradient with which they are both reduced is comparable. If this decline is due to quenching as predicted,

then these results imply that all SFGs, regardless of mass, experience the same rate of quenching outside of R_{500}. Consequently, whatever quenching mechanism(s) are responsible for this decline are largely independent of mass, and galaxy mass is clearly not solely responsible for the SFG fraction decline that we see at such large radii.

We then turn to binning by distance to the 5th nearest neighbour, d_{5nn}, in order to determine if local environment is the driver behind the declining trend we see at large radii. As it happens, we do in fact observe that local environment affects the rate at which the star-forming fraction declines, with denser local environments experiencing less SFG quenching, and less-dense local environments experiencing more. We also find that the overall fraction of SFGs is lower in denser environments, which suggests that these higher-density environments have a pre-processing effect on the galaxies within them – resulting in the star-formation of the members being suppressed before reaching the galaxy cluster (Fujita, 2004; Haines et al., 2015). Additionally, we observe that upon approach to the cluster centre, there is a lower fraction of SFGs across the board, irrespective of the density of their local environment. These findings therefore suggest that the declining trend seen in the total SFG population is primarily due to the SFGs in lower density local environments experiencing quenching at large radii, as SFGs in higher density environments at these radii appear to be protected from any global quenching. These results are in agreement with those seen in Lopes et al. (2024).

Finally, we conclude this analysis by attempting to determine whether the seemingly protective qualities seen from high local environment densities depend on the stellar mass of the galaxies, in a more nuanced way that was not visible in Section 3.3.2. We find that this situation is in fact the case in higher density regions, and that the distribution flattening seen in galaxies residing in high density local environments (see Section 3.3.3) primarily applies to high mass galaxies, with a less pronounced but still detectable shielding effect influencing lower-mass galaxies.

We postulate that these results suggest one of two possibilities in high density local environments. The first being that these high density regions, such as groups and filaments, are mainly only capable of shielding high mass galaxies from any potential global environment mechanisms responsible for quenching in the cluster

outskirts. Low mass galaxies may be more susceptible to these mechanisms, and therefore the shielding effect of the high density environment is not always strong enough to protect them. Alternatively, we could be seeing that high density local environments *are* effective at shielding all SFGs, irrespective of mass, from global environment quenching mechanisms, but they are in fact host to quenching mechanisms of their own that are more effective on low-mass galaxies, thus leaving the high mass SFG population unaffected.

This second possibility could provide an explanation for the driver behind the declining distribution seen here in high density local environments, but it still does not explain the driver behind the universally declining distributions seen in low-density regions for galaxies of all masses. Nevertheless, these findings suggest that whatever mechanisms are responsible for the decline of the SFG fraction must be mass-independent in low-density local environments, and potentially *mass-dependent* in high-density local environments. Ultimately, it would be very interesting to see the specific mechanisms responsible for these results identified and associated with their respective quenching effects, in both high and low local environment densities, in order to understand the root of the quenching of SFGs in the outskirts of galaxy clusters.

Chapter 4

From Outskirts to Core: the Suppression and Activation of Radio AGN around Galaxy Clusters[1]

4.1 Introduction

It is well established that both internal feedback from active galactic nuclei (Kauffmann et al., 2003b; Best et al., 2005a; Schawinski et al., 2007; Hickox et al., 2009; Best & Heckman, 2012) and external environmental influences (Kauffmann et al., 2004; Park et al., 2007; Silverman et al., 2008; Ellison et al., 2011; Sabater et al., 2013) play key roles in shaping the properties of galaxies. However, if AGN activity is, in turn, affected by the wider environment, then these two factors are not entirely independent, and study of the coupling between them is required to fully understand the drivers of galaxy evolution.

Since nuclear activity depends on the abundance of available gas to feed the AGN, which can be influenced by external environmental factors (Gunn & Gott, 1972; Larson et al., 1980; Farouki & Shapiro, 1981; Moore et al., 1996; Makino & Hut, 1997; Abadi et al., 1999), and the triggering mechanisms of the AGN can also be

[1]This work is published in: *de Vos, K., Merrifield, M. R., & Hatch, N. A. 2024, MNRAS, 535, 1, 217, 10.1093/mnras/stae2391*

externally driven—such as by interactions or mergers that disturb gas orbits and funnel material to the galactic center (Best et al., 2007; Poggianti et al., 2017a; Marshall et al., 2018; Ricarte et al., 2020; Peluso et al., 2022), it follows that different types of AGN may be affected in distinct ways by their environments.

AGN are broadly divided into two populations: radio-loud AGN (often referred to as "jet-mode" AGN) and radio-quiet AGN (or "radiative-mode" AGN), which differ significantly in their host properties and environmental dependencies (Heckman & Best, 2014). Radio-loud AGN, which are primarily identified via radio surveys, exhibit powerful relativistic jets and are typically found in massive, early-type galaxies within dense environments such as galaxy clusters. These AGN are strongly linked to their host galaxy mass and cluster environment, as denser surroundings provide the conditions necessary for jet-mode activity to be sustained. Studies have found that radio-loud AGN are more prevalent in high-density regions (Best et al., 2005a; Sabater et al., 2013), suggesting that dense environments may enhance the availability of accretable material or facilitate the conditions required for AGN fueling. Furthermore, Best et al. (2007) reported that brightest cluster galaxies (BCGs) host an enhanced fraction of radio-loud AGN, further reinforcing the link between cluster environments and this AGN population.

In contrast, radio-quiet AGN, which are more commonly detected via optical and X-ray surveys, lack extended radio jets and are often hosted by lower-mass galaxies with significant cold gas reservoirs. Unlike radio-loud AGN, the prevalence of radio-quiet AGN appears to be less strongly linked to cluster density. Optical and X-ray studies suggest that radio-quiet AGN activity is often suppressed in high-density regions, with triggering instead being more common in lower-density environments where mergers and secular processes can more easily transport gas to the galactic nucleus (Kauffmann et al., 2004; Silverman et al., 2008; Hickox et al., 2009). This difference in environmental dependence highlights the importance of AGN selection effects when interpreting their distribution.

Indeed, a recent large-scale simulation incorporating these physical processes (Ričhtaršič et al., 2024) confirmed that the prevalence of AGN depends not only on environment but also on AGN type. The study found that AGN activity depends significantly on distance from the nearest cluster of galaxies, with an enhancement in activity above the field level out to surprisingly large radii, and a suppression

of activity within the cluster itself, apart from a spike in AGN activity at the very centre of the cluster.

However, observational support for these environmental trends is rather mixed, and results often depend on the AGN selection method. For radio-loud AGN, many studies have found little to no variation with distance from a cluster, except for an increase in its very central region, where brightest cluster galaxies (BCGs) host a higher fraction of AGN (Best et al., 2007; Ruderman & Ebeling, 2005; Gilmour et al., 2009; Manzer & De Robertis, 2014; Mo et al., 2018; Hashiguchi et al., 2023). In contrast, for radio-quiet AGN, optical and X-ray surveys have frequently reported a suppression of AGN activity in high-density regions, with lower AGN fractions in the outskirts of clusters compared to the field (Ehlert et al., 2013, 2014; Gordon et al., 2018; Koulouridis et al., 2024). These contrasting findings highlight the importance of distinguishing between AGN populations when analysing their environmental dependence.

The reason for the lack of conclusive observational trends may be due to the modest amplitude of these effects, as well as the influence of AGN selection biases, where radio, optical, and X-ray surveys probe different AGN populations with distinct environmental dependencies. A large, homogeneous dataset is required to measure these trends unequivocally, but such a dataset has not been available until recently. Fortunately, the combination of the Low-Frequency Array Two-Metre Sky Survey (LoTSS) second data release (Shimwell et al., 2022) with the Sloan Digital Sky Survey sixteenth data release (Ahumada et al., 2020) provides just such a dataset. Its wide-area coverage allows for a detailed study of AGN distribution around clusters, and its well-defined radio-based AGN selection primarily traces jet-mode (radio-loud) AGN in dense environments. In this chapter, we use these data to examine how the fraction of radio-loud AGN varies with position out to large radii around clusters, providing insight into the role of environment in AGN triggering and suppression.

4.2 Data & Methods

To undertake the work in this chapter, we again utilise the data and methods described in Chapter 2, this time using the 12 380 *radio AGN* identified from LoTSS DR2 (Shimwell et al., 2022), and the 141 586 *SDSS galaxies* compiled from SDSS DR16 (Ahumada et al., 2020), MPA-JHU (Brinchmann et al., 2004), and the allWISE survey catalogue (Wright et al., 2010).

As was mentioned in Chapter 2, the optical cross-matching process for the radio sources used in this chapter was conducted manually using a maximum separation of 2" on the sky, which may have led to the omission of extended radio sources due to their larger positional offsets. Since the initial analysis, the LoTSS DR2 value-added catalogue has become available, containing 10,830 additional extended radio sources within the redshift range and spatial region used in this thesis, that were not matched in our dataset due to having a separation greater than 2" on the sky from their corresponding optical counterparts. Given that the majority of these sources appear to be AGN from their WISE colours, we investigated their potential impact on the results in this chapter by cross-matching their optical coordinates with *SDSS galaxies*.

Of the 10,830 extended sources, 815 were successfully matched to optical sources within *SDSS galaxies*. The distribution of these matched sources follows a similar pattern to that observed in our results, with 77% of the sample located at smaller cluster-centric distances, 20% at larger distances, and 3% at intermediate distances. This consistency suggests that the omission of these sources is unlikely to significantly alter our conclusions. However, as only a small fraction of the missing sources were matched, some uncertainty remains. While a more detailed investigation could further clarify the impact, the current analysis indicates that the overall trends reported in this chapter remain robust.

4.3 Results

4.3.1 Total AGN Fraction

With use of the two samples outlined above, *SDSS galaxies* and *radio AGN*, we are able to determine how the AGN fraction varies with respect to projected cluster-centric radius. We calculate this fraction in each annulus using the formula $F_{AGN} = N_{AGN}/N_{SDSS}$, where N_{AGN} and N_{SDSS} are the projected number densities of *radio AGN* and *SDSS galaxies* respectively. We choose to merge all galaxies into one bin at $R < 10^{-1.25}R_{500}$ due to the increasingly small number of AGN (< 10 per bin) in the individual logarithmically-spaced annuli within this radius. Finally, in order to more quantitatively define any deviation from the field fraction in the distribution, we normalise F_{AGN} by the field fraction, $F_{AGN,f}$, which is found to be ~ 0.09. Here, the "f" subscript denotes the field values for any pre-defined variables. We calculate the field AGN fraction by taking $F_{AGN,f} = N_{AGN,f}/N_{SDSS,f}$, where $N_{AGN,f}$ and $N_{SDSS,f}$ are the field values (as defined in Section 2.2.4) of *radio AGN* and *SDSS galaxies* respectively. The resulting cluster-centric distribution can be seen in Figure 4.1.

This figure, however, is a projection of the true radial trend, meaning each annulus has the effect of combining data from a range of radii. This plot will therefore tend to average away some of the true variation with radius, and so we de-project the distribution using the Abel inversion method described in Section 2.2.5. In Figure 4.2 we show the de-projected distribution of the trend seen in Figure 4.1.

From both of these figures, it is immediately apparent that there is a trend resembling a "wiggle" that has not been seen before with observational data. We see that out at around $10R_{500}$, the AGN fraction has risen above the field fraction to peak at a $\sim 25\%$ increase, with a 5.5σ significance for the projected distribution in Figure 4.1, and a 3σ significance for the de-projection in Figure 4.2. The AGN fraction then decreases with decreasing cluster-centric radius, until it reaches a minimum of $\sim 20\%$ below the field fraction line at around $0.5R_{500}$, with a 2.4σ significance in Figure 4.1, and a 2σ significance in Figure 4.2. The distribution finally trends back up again in the centre of the cluster, and culminates in a large spike at the very core, with a fraction over three times more than the field fraction.

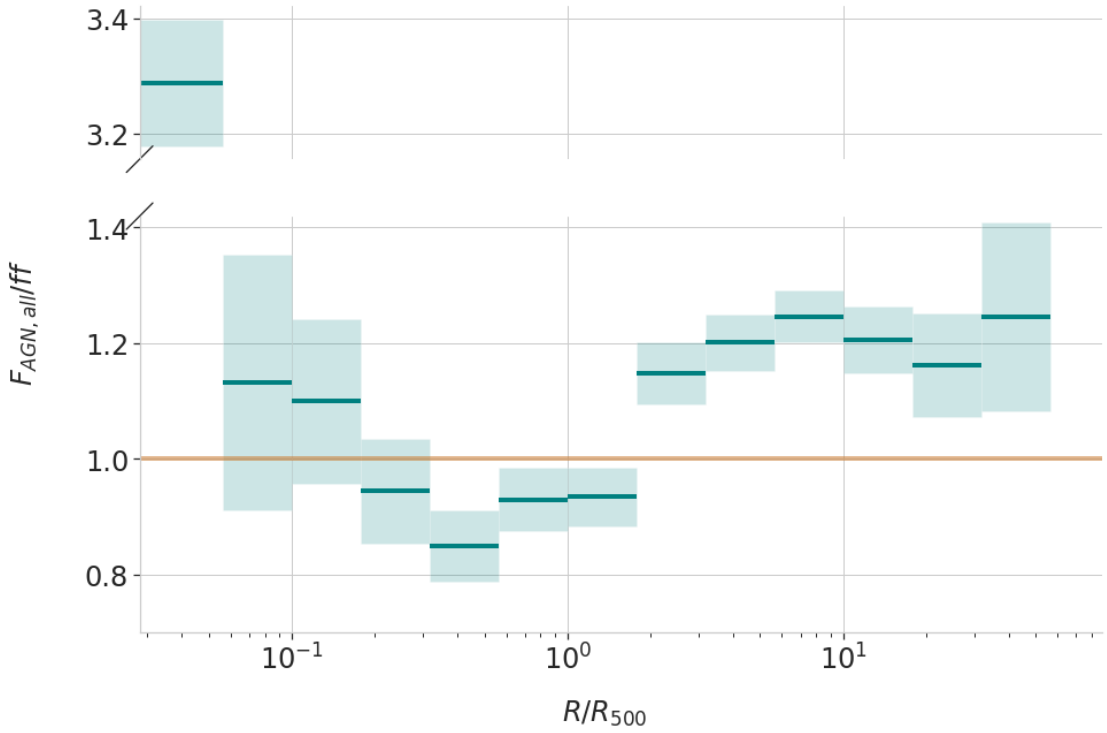

Figure 4.1: The projected distribution of the relative fraction of galaxies identified as active, with respect to projected cluster radius. The fraction values have been normalised with respect to the AGN field fraction, which is ~ 0.09. As such, the orange, horizontal, solid line marks the normalised AGN fraction in the field, which is 1. The innermost bin includes all galaxies between $0 < R < 10^{-1.25} R_{500}$.

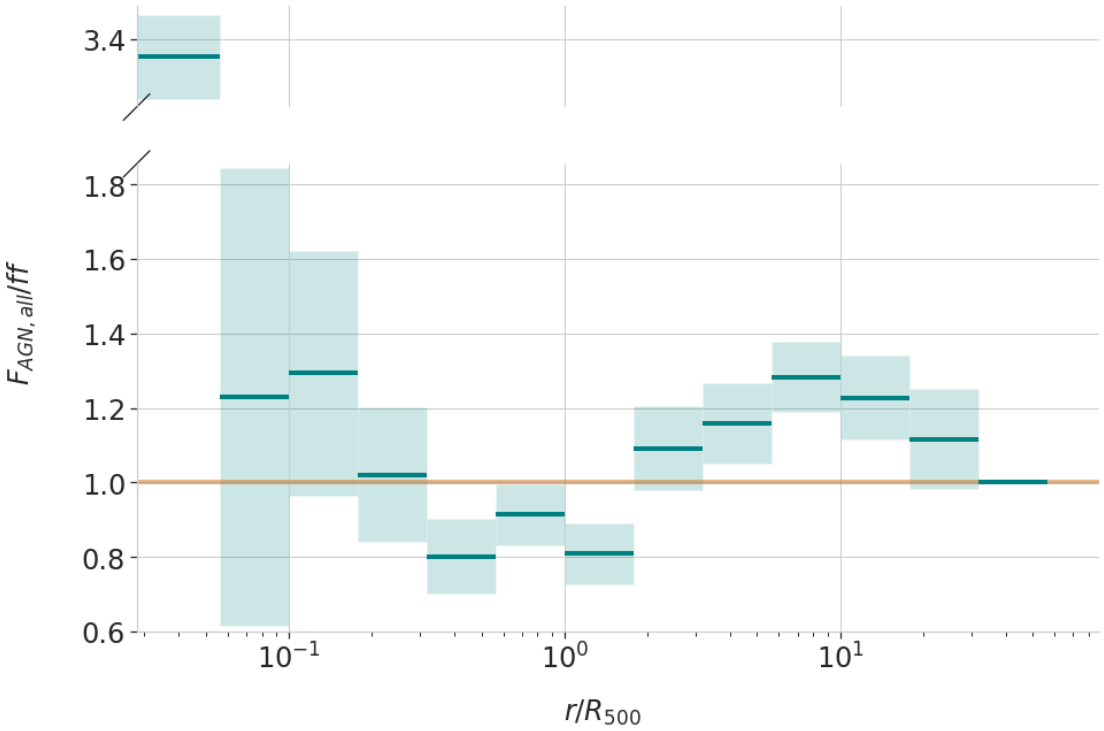

Figure 4.2: The de-projected distribution of Figure 4.1, showing the relative fraction of galaxies identified as AGN, with respect to cluster radius.

In order to test the significance of the features in this trend against a uniform distribution centred at 1, we perform a χ^2 test with the projected distribution data, not including the innermost bin, which results in a significance of more than 99.99 per cent for $\nu = 10$, where ν is the number of annulus bins minus the number of model parameters. It is worth noting that the qualitative shape of this variation with radius is very similar to that seen in Rihtaršič et al. (2024); we discuss the implications of this similarity in Section 4.4.

To explore the possible cause of these features, we split the cluster-centric radial bins into three regions: the *outer* region, defined by a radius of $r > 10^{0.25} R_{500}$ ($\sim 2R_{500}$); the *intermediate* region, given by $10^{-0.75} R_{500} < r < 10^{0.25} R_{500}$; and the *inner* region, for $r < 10^{-0.75} R_{500}$ ($\sim 0.2R_{500}$). These three regions are simply dictated by the radii at which the distribution crosses the field fraction line. This split allows us to investigate if the AGN in these three regions have different intrinsic properties or host galaxies that might be the cause of the fractional variation we are seeing as a function of cluster-centric distance.

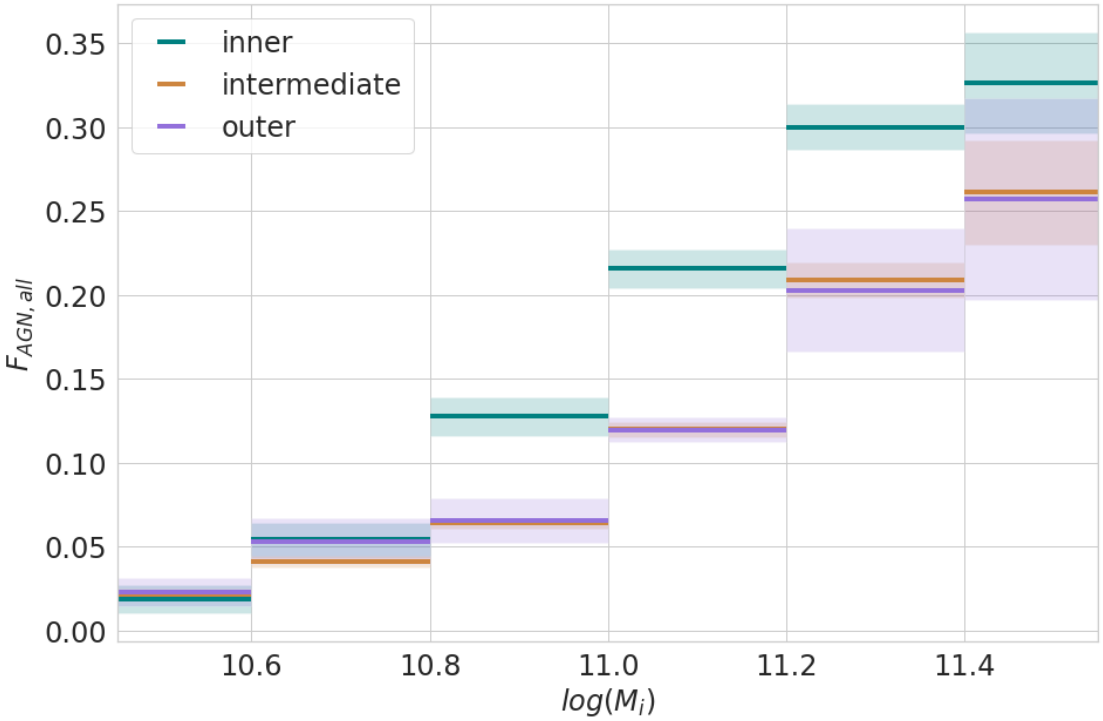

Figure 4.3: The i-band stellar mass distribution of the host galaxies of F_{AGN} separated into three distinct regions: *inner*, *outer* and *intermediate*. These regions are defined by the radii at which the AGN fraction distributions in Figures 4.1 and 4.2 cross the field line.

4.3.2 Mass Distribution

We start by analysing the stellar mass distribution of the AGN host galaxies for these three *inner*, *intermediate* and *outer* regions, as shown in Figure 4.3. Here we can see that, for all three radial ranges, there is an increase in the AGN fraction with mass, as expected (Sabater et al., 2019). However, it is not the absolute values that are informative here, but rather it is the differential between the regions that provides us with information that might suggest that radio AGN in one region have different intrinsic properties to the norm.

For instance, it is immediately apparent that there is a much higher fraction of galaxies in the *inner* region that have high stellar mass, which is to be expected as this region includes massive BCGs, many of which host AGN. There is no statistically significant difference between the *intermediate* and *outer* region mass distributions, which brings us to the conclusion that the stellar mass of the host

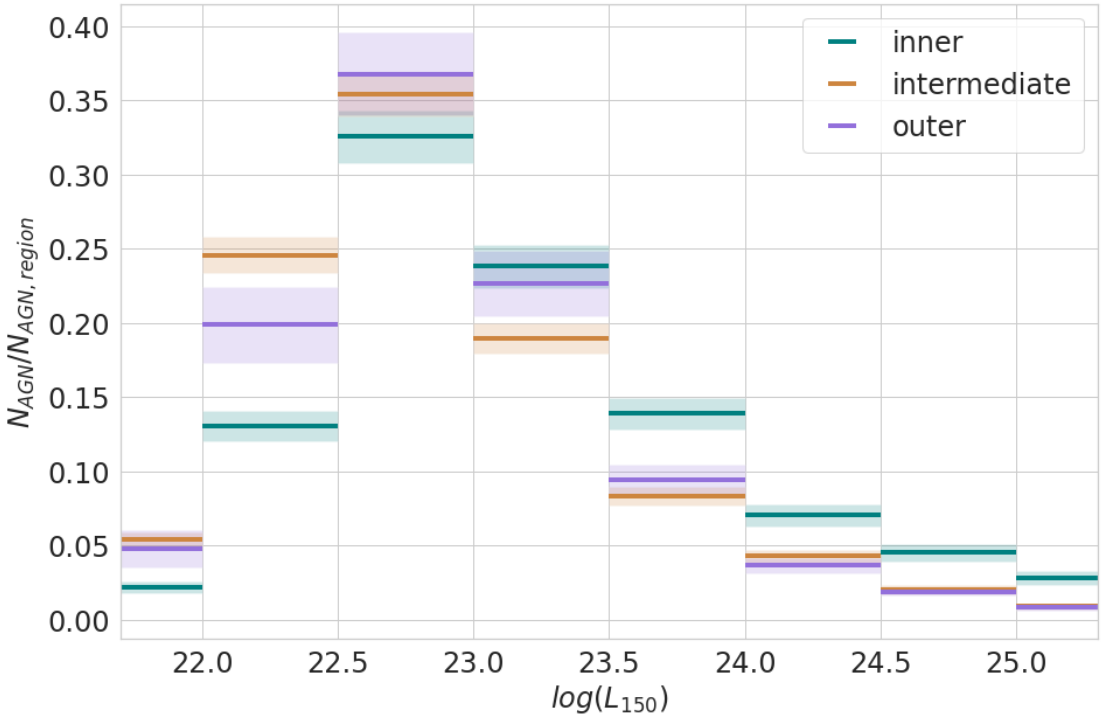

Figure 4.4: The L_{150} luminosity PDF of the *radio AGN* sample separated into three distinct regions: *inner*, *outer* and *intermediate*. These regions are defined by the radii at which the AGN fraction distributions in Figures 4.1 and 4.2 cross the field line.

galaxy is not the driver behind the fractional AGN differences seen in Figures 4.1 and 4.2 between these two regions.

4.3.3 Radio Luminosity

To assess whether the nature of AGN activity varies with radius, we next consider radio luminosity, L_{150}, which is investigated using the radio luminosity probability density function (PDF) in Figure 4.4. Here, as *SDSS galaxies* cannot be binned by L_{150}, we present $N_{AGN}/N_{AGN,region}$ on the y-axis, which is the number of AGN in a given region and luminosity bin, normalised by the total number of AGN in that region.

Looking at the differential between the three regions, we find that AGN in the *inner* region have a higher luminosity on average than the other two regions.

This result, again, is to be expected due to the BCGs in this sub-sample, which are known for both being the most massive galaxies at a given redshift, and for having higher radio luminosities for a given stellar mass (Von Der Linden et al., 2007; Best et al., 2007). We do notice, however, that the *intermediate* region has the highest fraction of low-luminosity AGN, and generally the lowest fraction of high-luminosity AGN, making the *outer* region the middling luminosity sample on average; this finding indicates that the nature of AGN activity does depend on cluster-centric radius.

4.4 Summary & Discussion

In this chapter, we have seen from both Figures 4.1 and 4.2 that the distribution of the fraction of radio-loud AGN with respect to cluster-centric radius takes the form of a "wiggle". In the *outer* regions, past $\sim 2R_{500}$, we see an increase of up to $\sim 25\%$ above the field fraction, followed by a decrease of $\sim 20\%$ relative to the field in the *intermediate* region, and a huge spike in the very core, *inner* region of the cluster. Although they explored a smaller range of radii, the shape of this distribution is very similar to that seen for massive, quiescent AGN in the recent simulation paper from Rihtaršič et al. (2024). In their paper, they propose that the surge of excess AGN in the outskirts of the cluster is due to the velocity dispersion being lower in this region, thus allowing for a greater frequency of mergers that trigger AGN activity, which would be in agreement with other findings in the literature (Ruderman & Ebeling, 2005; Fassbender et al., 2012; Haines et al., 2012; Koulouridis & Bartalucci, 2019). They also postulate that the reduction seen in the *intermediate* region might be due to the opposite effect, of fewer mergers taking place due to the higher velocity dispersion in the cluster itself. The spike of radio AGN seen in the cluster core can be explained by the work of Best et al. (2007), which shows that the accretion of hot gas from a strong cooling flow increases the likelihood that BCGs host radio AGN.

This scenario is consistent with the luminosity variations seen in the three populations observed in Figure 4.4. Given that the fraction of AGN is declining in the *intermediate* region, it would stand to reason that the AGN populations in this area may be starved of fuel due to less frequent mergers, resulting in a lower

radio luminosity. Similarly, the potential mergers providing fuel and generating the excess of AGN in the *outer* regions may be responsible for the higher radio luminosities observed within this sample, as mergers have been found to generate the most luminous and radio-loud AGN (Treister et al., 2012; Chiaberge et al., 2015).

It thus appears as though the variations seen in AGN fraction are reflected by their radio luminosity in the same spatial regions. The AGN fraction is at its highest in the *inner* region, and these AGN also appear to be the most radio luminous; whereas the AGN fraction is at its lowest in the *intermediate* region, which also appears to hold the highest fraction of low luminosity AGN; finally, the *outer* region, which has the "middling" galaxy fraction extremum, also appears to host the "middling" level of AGN activity across the luminosity range.

However, we do not see variations in the i-band stellar masses of the host galaxies of AGN in the *intermediate* and *outer* regions of galaxy clusters. The *inner* region displays a clear increase in the number of massive host galaxies, which can be attributed to the presence of BCGs near the centre of most clusters (Best et al., 2007), but the mass distributions of AGN host galaxies in both the *intermediate* and *outer* regions are almost identical, suggesting that the fractional "wiggle" seen in Figures 4.1 and 4.2 cannot be attributed to a difference in the host stellar mass.

The features seen and discussed here are all relatively subtle effects, which may be the reason why previous studies have found conflicting or inconclusive results. The combination of both AGN being quite rare astronomical objects, and the variation from the field fraction being only $\sim 20-25\%$, means that it would be easy to miss without a large population of clusters and AGN, as used here.

To conclude, we have determined that there is statistically significant variation in the fraction of radio AGN with respect to cluster-centric radius, the shape of which was predicted in a recent simulation paper by Rihtaršič et al. (2024). The similarity of the host galaxy stellar masses in the *intermediate* and *outer* regions suggests that the differences in AGN fraction between these regions are not driven by their host galaxy properties. However, the variation in radio luminosity seen between all three regions suggests that AGN fraction isn't the only difference in these radial windows - AGN activity itself is distinct too. The combination of

these results suggest that the effects seen are driven by different environmental mechanisms, depending on the AGN's location with respect to the nearest cluster, which cause them to oscillate between activity and inactivity independent of their host galaxy's stellar mass. In the case of AGN activity in the proximity of galaxy clusters, nurture wins out over nature.

Chapter 5

Clusters' Far-Reaching Influence on Narrow-Angle Tail Radio Galaxies[1]

5.1 Introduction

Having identified variations in the AGN fraction with radius, we now turn to more detailed physics about the interplay between AGN and their environments. The interaction between galaxies and their surrounding gas, whether circumgalactic medium, intergalactic medium or intracluster medium, is a major driver of galaxy evolution. Nowhere is this interaction more dramatically demonstrated than in radio galaxies moving through the ICM of their surrounding cluster. The synchrotron-emitting plasma that comprises the radio lobes is ejected from the body of the galaxy, meaning that it is subject to the hydrodynamical processes that result from its interaction with the ICM: ram pressure will cause the jets to bend (Cowie & McKee, 1975; Begelman et al., 1979; O'Dea, 1985; Roberts et al., 2021b), while buoyancy effects can cause them to "float" towards the edge of the cluster (Gull & Northover, 1973; Gendron-Marsolais et al., 2017).

Narrow-angle tail radio sources are a particular class of extended, double-tail radio galaxy that have had their radio jets bent back such that the observed angle

[1]This work is published in: *de Vos, K., Hatch, N. A., Merrifield, M. R., & Mingo, B. 2021, MNRAS, 506, 1, L55, 10.1093/mnrasl/slab075*

between them is acute. Of course, this projected angle on the sky may not reflect the true three-dimensional bending which could be significantly less extreme, but the most plausible underlying physical cause of such distortions – ram pressure due to the galaxy's motion relative to the cluster – means that this projected geometry can always be used as a diagnostic of the source's direction of motion on the plane of the sky. O'Dea et al. (1987) took this approach to analyse the orbits of 70 NATs in Abell clusters, and concluded that the orbits were close to isotropic, but with some indication of a radial bias at small radii. However, they argued that a larger sample was required to make any definitive statement about cluster orbits.

The largest study of bent radio jets in clusters to date is by Garon et al. (2019, hereafter G19), who made use of a sample of extended radio galaxies identified through Radio Galaxy Zoo (Banfield et al., 2015). G19 found that the 340 radio sources they identified as "highly" bent have a slight tendency to indicate radial orbits with respect to their cluster centre. They also discovered that such bent systems were found out to fairly large radii, with as many outside $1.5R_{500}$ as inside it. Since ram pressure is proportional to the density of the ICM, and is a necessity for bending double-tail radio sources to such a high degree, it is puzzling that such bent sources would be commonly found out at large distances from the cluster centre where the ICM density is low.

However, G19 adopted a generous limit on what constituted a "highly bent" double-tail source, and in fact explicitly excluded all sources in which the observed angle between the two radio jets was less than 45° over the concern that such objects might be mis-associated background sources. Since these steeply-bent sources comprise a large proportion of what is classically labelled as a NAT, it is not clear that G19 and O'Dea et al. (1987) identified comparable populations, and hence whether the physics bending the jets is the same in both cases.

We have therefore sought to revisit these issues, focusing specifically on radio galaxies identified as NATs in the largest sample available to date. We explore the angles in which their jets are bent relative to the closest cluster, and investigate in more detail how this distribution varies with projected distance from the cluster centre. In Section 5.2, we describe the data set and analysis technique, while Section 5.3 presents the resulting distribution of orbital angles and its variation

with radius, and compares it to the analysis of G19. In Section 5.4, we discuss the implications of the rather unexpected but very strong signal that we detect.

5.2 Data & Methods

To conduct this study, we utilise data from LoTSS DR1 (Shimwell et al., 2019), as described in Section 2.1.1. In addition to the benefits of using LoTSS already outlined in Section 2.1.1, its observations at 144MHz have been shown to be significantly better for the detection of NATs than higher frequency data, due to the steep spectra of such mature radio sources (O'Neill et al., 2019a,b).

From this data set, we extract the 264 NATs visually identified by Mingo et al. (2019), who classified the morphologies of 5805 extended radio-loud AGN in LoTSS DR1. Optical or infrared counterparts for all of the NATs were identified by Williams et al. (2019) using either a likelihood ratio identification algorithm or, for larger and more complex sources, visual identification through the LOFAR Galaxy Zoo project[2]. Spectroscopic redshifts are available for 179 of the 264 NATs, and for the remaining 85 NATs we use the photometric redshifts derived by Duncan et al. (2019), which have an overall scatter $\sigma_{\rm NMAD} = 0.039$ and an outlier fraction of 7.9%.

To identify the environments of the NATs, we follow the cluster–galaxy association method outlined in Section 2.2.3, with a few minor differences. Firstly, we determine the most likely host cluster (if one exists) for a NAT by identifying all clusters associated with it using Equation (2.7), as opposed to identifying the most likely galaxies associated with individual clusters as described in Section 2.2.3. Taking into account the photometric redshift uncertainties of some of the sources used in this work, we find that Equation (2.7) corresponds to a velocity window of $\pm 12,000\,\mathrm{km/s}$.

Secondly, we only assign one host, which is the cluster with the minimum projected distance to the NAT. These criteria associated a cluster with 255 of the NATS in our sample. In 47 cases, the optical source associated with the NAT was found to

[2] https://www.zooniverse.org/projects/chrismrp/radio-galaxy-zoo-lofar

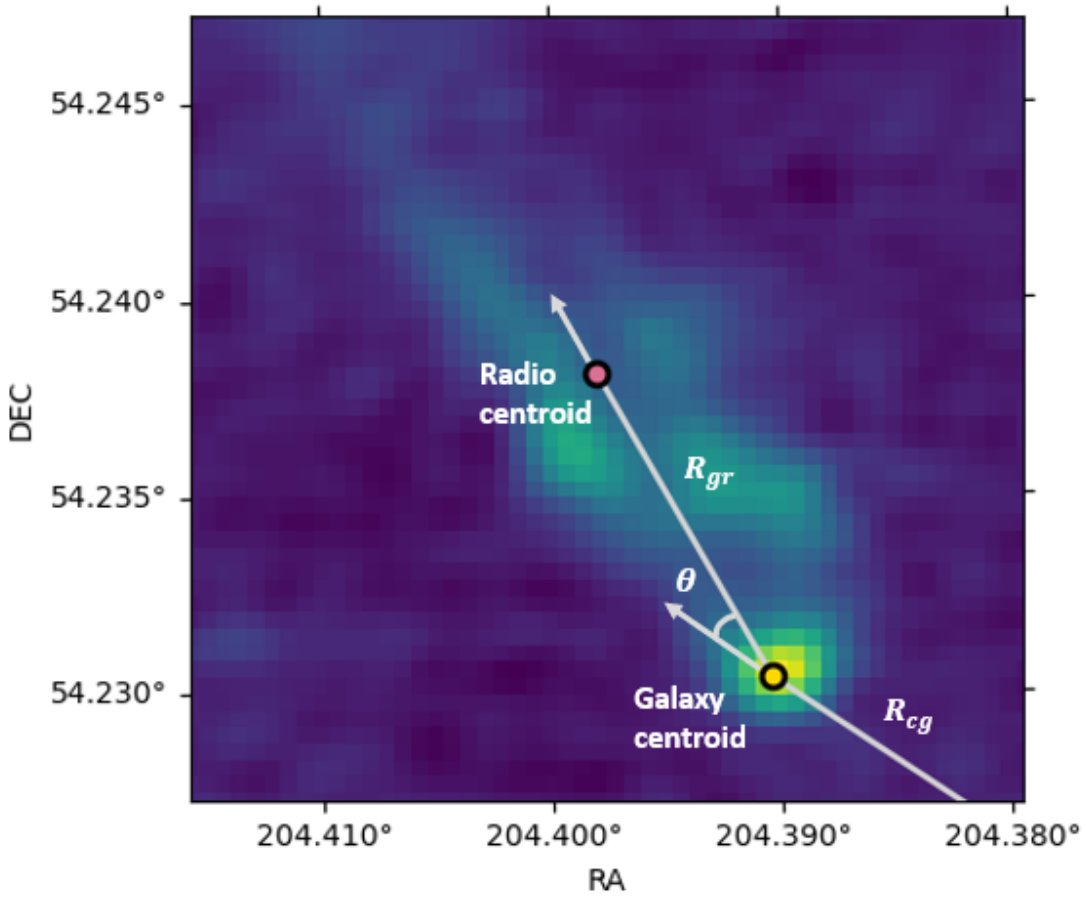

Figure 5.1: The definition of the angle θ between $\mathbf{R}_{cg}$ and $\mathbf{R}_{gr}$, overlaid on the image of a typical NAT as observed by LOFAR.

be the BCG of the cluster; since these objects are used as a proxy to define the centre of the cluster, there is no meaningful information to be obtained from them regarding offsets from the cluster centre. To exclude such objects, while allowing for possible centring errors, we eliminate all sources within a projected radius of $0.01R_{500}$, which leaves a final sample of 208 NATs.

For each NAT–cluster pair, we calculate θ, the counter-clockwise angle between the vector from the cluster centre to the galaxy centroid, $\mathbf{R}_{cg}$, and the vector from the galaxy centroid to the centroid of radio emission, $\mathbf{R}_{gr}$; a typical example of this calculation is shown in Figure 5.1, which also illustrates the high quality of the LoTSS data. We map these angles into the range $-180° < \theta < 180°$, so that $|\theta| \sim 0°$ describes a radio tail pointed away from the cluster centre, while $|\theta| \sim 180°$ represents a radio tail aligned toward the cluster centre.

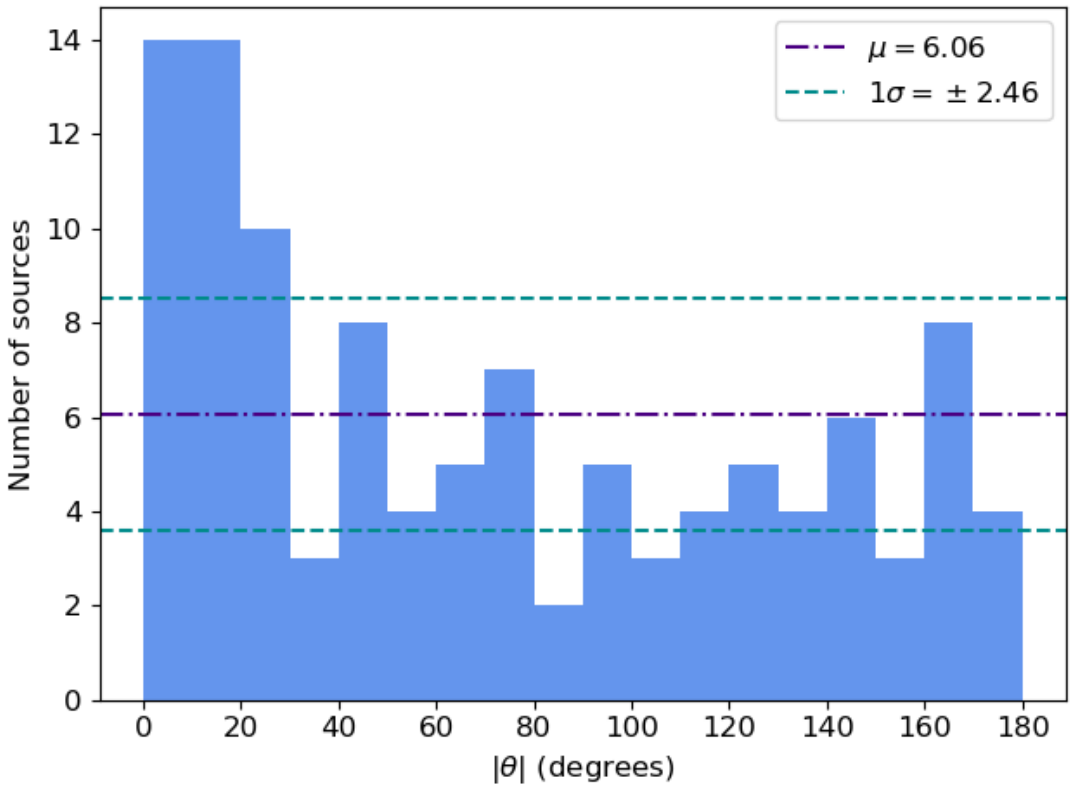

Figure 5.2: The angle distribution of narrow-angle tail radio sources with respect to their cluster centres, out to $7R_{500}$. The lines indicate the expectations of a uniform distribution, with Poisson noise appropriate to the size of the sample.

5.3 Results

Using a conservative limit of $R < 7R_{500}$ to avoid significant line-of-sight contamination, we are left with a sample of 109 NATs, the angle distribution for which is presented in Figure 5.2. It is immediately apparent from this figure that the data does not appear consistent with the expectations of a uniform distribution, but rather shows an excess at small angles. To test the significance of this apparent non-uniformity, we conducted an Anderson–Darling (AD) test, which offers a more powerful tool than the commonly used Kolmogorov–Smirnov test when assessing the significance of features near the ends of a distribution (Stephens, 1974). Testing the observed distribution against a uniform model results in an AD statistic of 7.94, which is significant at the 99.99% confidence level for a sample of this size (Jäntschi & Bolboacă, 2018). To check that this result is not an artefact produced

by the flux-weighted manner in which we have defined the NATs' angles on the sky, we repeated the analysis using the angle defined by the bisector of the two jets in each NAT, as located by their peak fluxes (Mingo et al., 2019); this definition produced a very similar non-uniform distribution of angles. We also note that any residual uncertainty in this measurement would serve only to dilute the signal apparent in Figure 5.2.

We next assess the level of line-of-sight contamination caused by using the photometric redshifts for the subsample of the NATs that lack spectroscopic data. Figure 5.3 shows the projected phase-space diagram for the subset of objects for which we have full spectroscopic redshifts. The data points have been scaled by their individual values of R_{500} and the characteristic velocity σ_{500}, so that objects in clusters of differing mass can be compared consistently in this phase space. Although the amount of line-of-sight contamination clearly increases with radius, this plot confirms that its level remains modest out to the $7R_{500}$ limit adopted in Figure 5.2: only $\sim 25\%$ of the cluster-NAT pairs are false associations which act to dilute the signal.

Beyond this radius, the level of contamination increases rapidly, but for these sources with spectroscopic redshifts we can extract a largely uncontaminated sample out to significantly larger radii by taking the NATs that lie within the dashed lines on Figure 5.3, for which $|v| < 2\sigma_{500}$. Reassuringly, as is also apparent from Figure 5.3, the contaminating sources excluded by this process have an angle distribution that is consistent with random, confirming that the alignment effect in Figure 5.2 is associated with the cluster rather than some spurious systematic bias.

In the remaining sources that are associated with clusters, the alignment effect appears to persist out to at least $\sim 10R_{500}$. We confirm that this phenomenon is not just associated with the cluster core by repeating the AD test on the spectroscopically-confirmed associations that lie in the radial range $3R_{500} < R < 10R_{500}$, well outside the virial radius, which lies at $\sim 1.4R_{500}$ (Walker et al., 2019). We find that their angular distribution is also inconsistent with a uniform distribution at the 99.9% confidence level, with an AD statistic of 6.02. Interestingly, if we do look at just the cluster core in Figure 5.3, there also appears to be an excess of NATs for which $|\theta| > 135°$, which we will discuss further in Section 5.4.

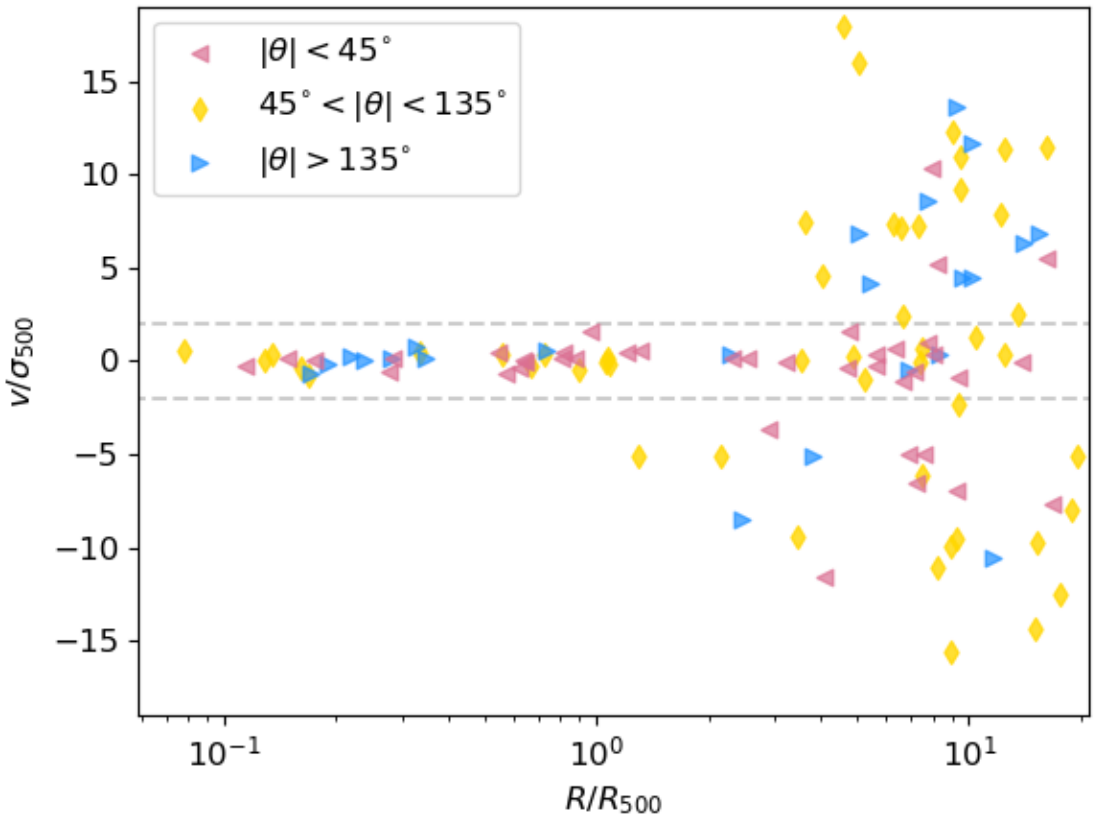

Figure 5.3: The projected phase space distribution (showing line-of-sight velocity versus projected separation) of the NATs in the sample with spectroscopic redshifts out to $20R_{500}$. The dashed lines at $v = \pm 2\sigma_{500}$ indicate the limits of velocity assumed to be associated with the cluster.

It is notable that these results differ from those of G19 in several ways. Not only is the non-uniformity in θ presented in Figure 5.2 significantly stronger that that detected by G19, but it also shows up as an asymmetric feature; we find that many more tails are directed away from the cluster than toward it, whereas G19 determined the presence of this asymmetry in folded data but did not disaggregate these populations. In addition, we find strong evidence that this phenomenon persists to much larger radii than previously probed. The greater strength of these effects suggests that the LOFAR-detected NATs studied here are more dramatic probes of the ICM–galaxy interaction than previously recognised.

5.4 Discussion

In this analysis, we have shown that the angle distribution of NATs implies that at least some are aware of the direction to the nearest cluster of galaxies, and that this awareness extends to surprisingly large distances. By way of summary, Figure 5.4 shows in polar form how, for the spectroscopically-confirmed NATs, the angles between bent radio jets and cluster centres are distributed as a function of radius. This plot emphasizes the preference of the radio jets to point away from the cluster out to $\sim 10R_{500}$, but also indicates the secondary feature of an excess of NATs whose tails point toward the cluster centre within $\sim 0.5R_{500}$. The cardinal labels on Figure 5.4 indicate the direction of travel of the NATs on the plane of the sky, assuming that their tail-bending is due to ram pressure.

Such features are notable because even if an infalling radio galaxy and its immediate surroundings are close enough to feel the gravitational effects of the nearby cluster, the equivalence principle implies that they cannot be aware of such influence – and hence the jets cannot be bent in specific directions – if they are simply freely falling in that gravitational field. As previous studies of jet bending have noted, it requires the additional presence of hydrodynamical phenomena, where forces other than gravity are in play (Cowie & McKee, 1975; Begelman et al., 1979; O'Dea et al., 1987; Sakelliou & Merrifield, 2000).

Within the virial radius of a cluster, one would expect the ICM to be largely in hydrostatic equilibrium, so radio jets emerging from galaxies in this region would

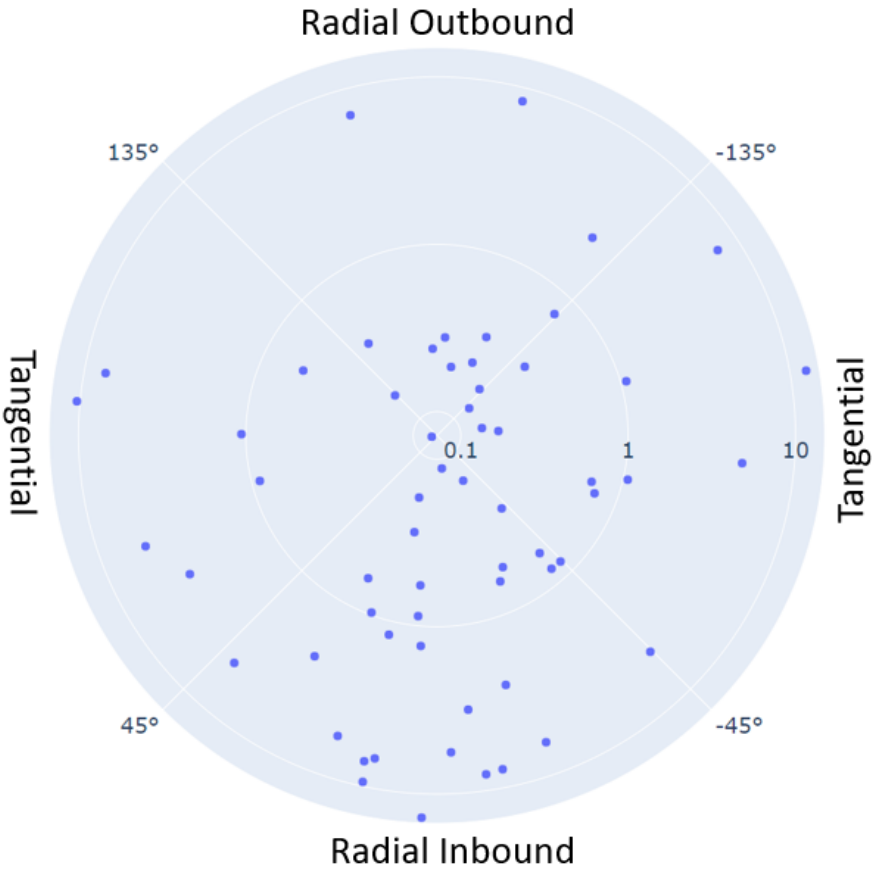

Figure 5.4: A polar diagram of the distribution of NAT angles on-the-sky, θ, as a function of radius, R/R_{500}, for those sources spectroscopically confirmed to be associated with a cluster, such that $|v| < 2\sigma_{500}$. The cardinal points are labelled to show the orbital direction we would expect the galaxies to be travelling in with respect to the cluster centre, if the values of θ are the result of ram-pressure bending of their jets.

be bent by their motions relative to this stationary gas due to ram pressure. Any additional infalling gas is rapidly decelerated at a "virial shock" close to this radius (Hurier et al., 2019), although the morphology of shocks in infalling gas can be quite complex, with external shocks occurring all the way out to $\sim 5R_{500}$ (Molnar et al., 2009; Walker et al., 2019). Such shocks produce the non-gravitational changes in the bulk flow of the gas that decouples it from the motions of galaxies, potentially providing the speed differential required to form NATs.

However, none of these shock processes seem to be predicted to occur out to the $\sim 10R_{500}$ where NATs are observed here. We therefore suggest that the true morphology of infalling gas is yet more complex, with significant hydrodynamical processes occurring out to even larger radii. In this context, it is interesting to note that Fig. 1 of Reiprich et al. (2013) shows tendrils of heated gas extending to well beyond $5R_{500}$. While such radially-extended features may be quite rare, it seems likely that hydrodynamical phenomena also play a role in triggering the AGN activity in the first place (Poggianti et al., 2017a; Marshall et al., 2018; Ricarte et al., 2020), which means that radio jets will preferentially be generated in just these regions, highlighting where they do occur. We presented potential evidence of this hypothesis in Chapter 4, with the findings that there is an increase in the AGN fraction above the field around $10R_{500}$.

An infalling NAT will, after passing its pericentre near the cluster centre, then continue radially outward on its orbit, on its way to becoming a cluster member. Indeed, we can seemingly identify such a component in Figure 5.4, which shows an excess of NATs within R_{500} that have their jets bent at $|\theta| \sim 180°$, indicating an outbound galaxy on the plane of the sky if the bends are caused by ram pressure. It is interesting to note that the timescale on which an outbound galaxy will reach the $\sim 0.5R_{500}$ radius at which the NATs seem to fade out, $\tau \sim 0.5R_{500}/\sigma_{500}$, is, for the characteristic masses of clusters in this sample, a few hundred million years, which is directly comparable to the lifetimes predicted for such sources (Antognini et al., 2012). This coincidence suggests that pericentre passage may represent the point at which new NATs are no longer being triggered.

We thus have a scenario that at least plausibly explains the rather unexpected structures apparent in Figure 5.4. At large radii, galaxies and gas lie in infalling filaments, some of which are dense enough that hydrodynamic effects start to

decelerate the gas relative to the galaxies. The resulting differential will disturb the gaseous environment around the galaxies, potentially triggering AGN activity to produce large-scale radio jets, and these jets are then bent through ram pressure effects that arise from the speed differential. At least some of these radio jets have long enough lifetimes to survive their pericentre passage, creating the excess of radially outbound NATs at small radii.

Chapter 6

The Search for Evidence of Ram Pressure Outside Galaxy Clusters

6.1 Introduction

As we saw in Chapter 5, many NATs lie on infalling orbits out to surprisingly large radii – as far out as $\sim 10R_{500}$ from the cluster centre. At such considerable distances there should not be any surrounding medium for ram pressure, and therefore jet bending, to take place. To explain these results, we hypothesised that these NATs could in fact be infalling towards clusters down filaments, where the gas medium may be dense enough to bend a radio AGN's jets into a NAT.

In this chapter, we test this hypothesis in the following way: if filament medium density is high enough to induce ram pressure, then we assume this same ram pressure will also be affecting other galaxies in the filament. In star-forming galaxies this mechanism will result in regions of increased star formation due to the compression of gas on the leading edge of the galaxy (Gavazzi et al., 2003; Poggianti et al., 2017b; Jaffé et al., 2018; Ramatsoku et al., 2019), or even the creation of jellyfish galaxies by the stripping of interstellar medium, and the triggering of starbursts along the resulting gas tail of the galaxy (Ebeling et al., 2014; Poggianti et al., 2017b; Jaffé et al., 2018). Such effects would be visible via distortions in the Hα emission distribution from the off-centre star formation, therefore confirm-

ing that the gas medium density in a filament can be high enough to induce ram pressure effects.

The Wide Field Camera (WFC) at the Isaac Newton Telescope (INT) is an ideal instrument with which to take images of such a galaxy cluster system in order to test this hypothesis, due to its large 34 arcmin^2 Field of View (FOV), and variety of available broad and narrow band filters. We reduce and analyse the i-band and Hα emission data we have obtained with the INT WFC to determine whether enhanced star-formation activity is visible on the leading edges of SFGs near a NAT, thus indicating the presence of ram pressure effects in the same region. We begin by describing the target selection, observations and analysis in Section 6.2, and present the results of this work in Section 6.3.

6.2 Data & Methods

6.2.1 Target Selection & INT Observations

In order to select a target with which to test this hypothesis, we choose a NAT from the sample described in Chapter 5 with which we can attempt to identify a dense filament. This choice must satisfy the following conditions: the NAT has to be at a large enough distance from its associated cluster that it lies outside the virial radius, but is close enough to be visible within a pointing of the INT WFC; the cluster must be at a suitable redshift to also be entirely visible within a pointing of the WFC without being too small, or taking up too much of the pointing so that any potential filament would not be visible; the cluster must be at a redshift such that Hα emission from its members would be visible through the available narrow-band (NB) filters at the INT WFC. These conditions are met by Abell 1682, a rich cluster at a redshift of 0.226 with R_{500} = 1.41 Mpc, with infalling NAT ILTJ130552.58+462245.6 located at a projected distance of 3.3Mpc ($2.3R_{500}$) away. Coincidentally, this NAT happens to lie on the line between Abell 1682 and another cluster identified by Wen & Han (2015) at RA 13:03:58.54, Dec 45:50:46.46, making it a particularly likely candidate to be the resident of a filament (Bond et al., 1996).

Using the WFC mounted at the prime focus of the INT, we obtained optical imaging data of the cluster Abell 1682 in the i-band and Hα. The large 34 arcmin^2 FOV enables us to capture both the cluster and its outskirts, including the identified NAT and the potential filament, all within one frame, as shown in Figure 6.1. This FOV corresponds to an area of $\sim 7.4 \times 7.4$ Mpc, 5.3$\times$ the R_{500} radius of the cluster. The instrument is a mosaic of four chips of 2048 $\times$ 4100 pixels, arranged in a square. The CCDs have a pixel scale of 0.33 arcsec pixel^{-1} which corresponds to a physical distance of 1.206 kpc pixel^{-1} at the redshift of the cluster.

We used the WFCSloanI broadband (BB) filter centred at 7743 Å and full width at half maximum (FWHM) of 1519 Å, and the custom made narrow band (NB) filter NOVA804HA, centred at 8038.5 Å with a FWHM of 110 Å. The NOVA804HA NB filter was in fact designed to detect Hα emissions redshifted from their usual restframe wavelength of $\lambda = 6562.8$ Å to redshifts of $z = 0.225$ (Stroe et al., 2014). The WFCSloanI BB filter was chosen as it overlaps with the bandwidth of the NOVA804HA NB filter.

We observed the cluster on the nights of 2023 April 18th, 20th, 22nd, and 23rd, with some of the time being split between this programme and a service proposal. Following Stroe et al. (2014), we took individual exposures of 200s in the BB and 600s in the NB, following a spiral dithering pattern of 60 arcsecond offsets in RA and Dec moving clockwise and outwards, with ±5 arcseconds in any unchanged axes. The dithering pattern was designed to cover the gaps in the CCDs, but also to spread any dead pixels around over multiple exposures, so that they might be more easily removed in the image reduction process. We discuss the total number of exposures below in Section 6.2.2.

6.2.2 Image Reduction

In order to reduce the images, we use the GUI version of THELI[1] (Erben et al., 2005; Schirmer, 2013a,b), a data processing pipeline for optical, near-infrared and mid-infrared astronomical images. THELI allows us to reduce the raw WFC images from the INT by processing the bias, flat and sky images for each night and filter, subtracting the sky, performing flux calibrations, and co-adding the images.

[1]https://github.com/schirmermischa/THELI

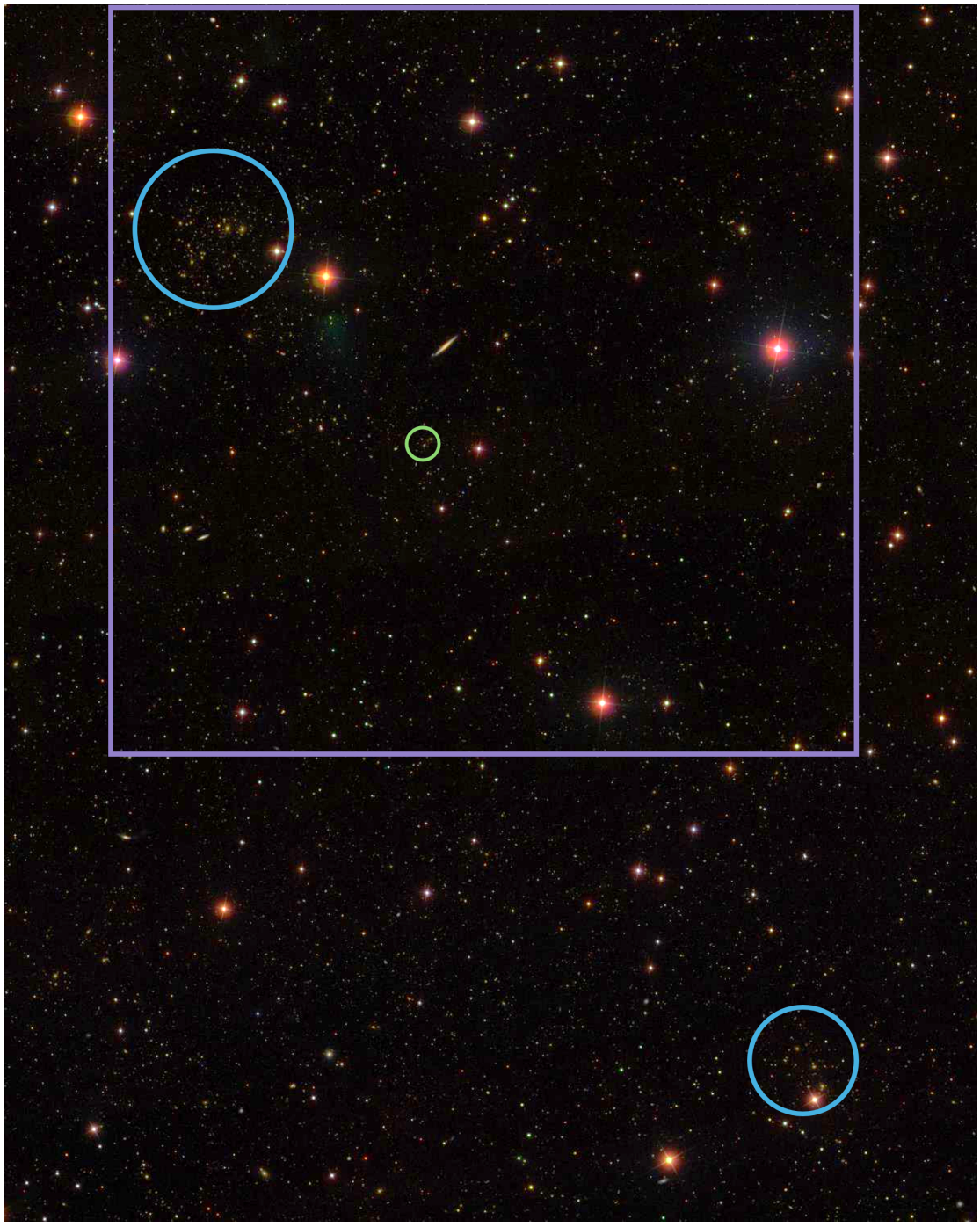

Figure 6.1: An SDSS image of the approximate positioning of the WFC field of view (purple square), NAT (small green circle), Abell 1682 cluster (large blue circle), and nearby cluster identified in Wen et al. (2012) (smaller blue circle). The NAT lies in a filament-likely location between the two clusters.

	Filter			
	WFCSloanI		NOVA804HA	
Night	No. of exp.	Int. time (s)	No. of exp.	Int. time (s)
18-04-2023	5	1000	5	3000
20-04-2023	13	2600	13	7800
22-04-2023	19	3800	19	11400
23-04-2023	18	3600	20	12000
Total	55	11000	57	34200

Table 6.1: The number of good exposures and total integration time of each of the three filters used, for each night of observations. The total number of good exposures and integration time for each filter is also stated.

Before reduction, we remove any bad frames due to over-exposure, cloud cover, or issues with the image headers having been incorrectly produced by the INT. The total integration time and number of good exposures for each night and filter is shown in Table 6.1. This process results in two co-added images of the selected field, one image for each of the WFCSloanI and NOVA804HA filters.

6.2.3 Source Extraction

With the images reduced, we perform the source extraction process using the Photutils package (Bradley et al., 2024) in Python, in order to identify potential SFGs in the region of the NAT that might also be experiencing effects due to ram pressure. We begin by re-projecting the i-band co-added image onto the world co-ordinate systems of the Hα-band image, so that the pixel size of the two images match perfectly. We then mask all bright foreground stars, as well as the outer edges of the images, in order to prevent spurious identification of sources due to noise or ghost objects. We show a side-by-side comparison of the original image and masked image in Figure 6.2. We produce a de-blended segmentation map of the Hα image, detecting sources more than 5σ above the background. From this segmentation map source catalogues are produced for both the i-band and Hα images, in order to ensure that both catalogues contain matched sources.

THELI provides the reduced images with flux conversion factors based on their waveband. We apply these factors to the Kron fluxes produced from the source

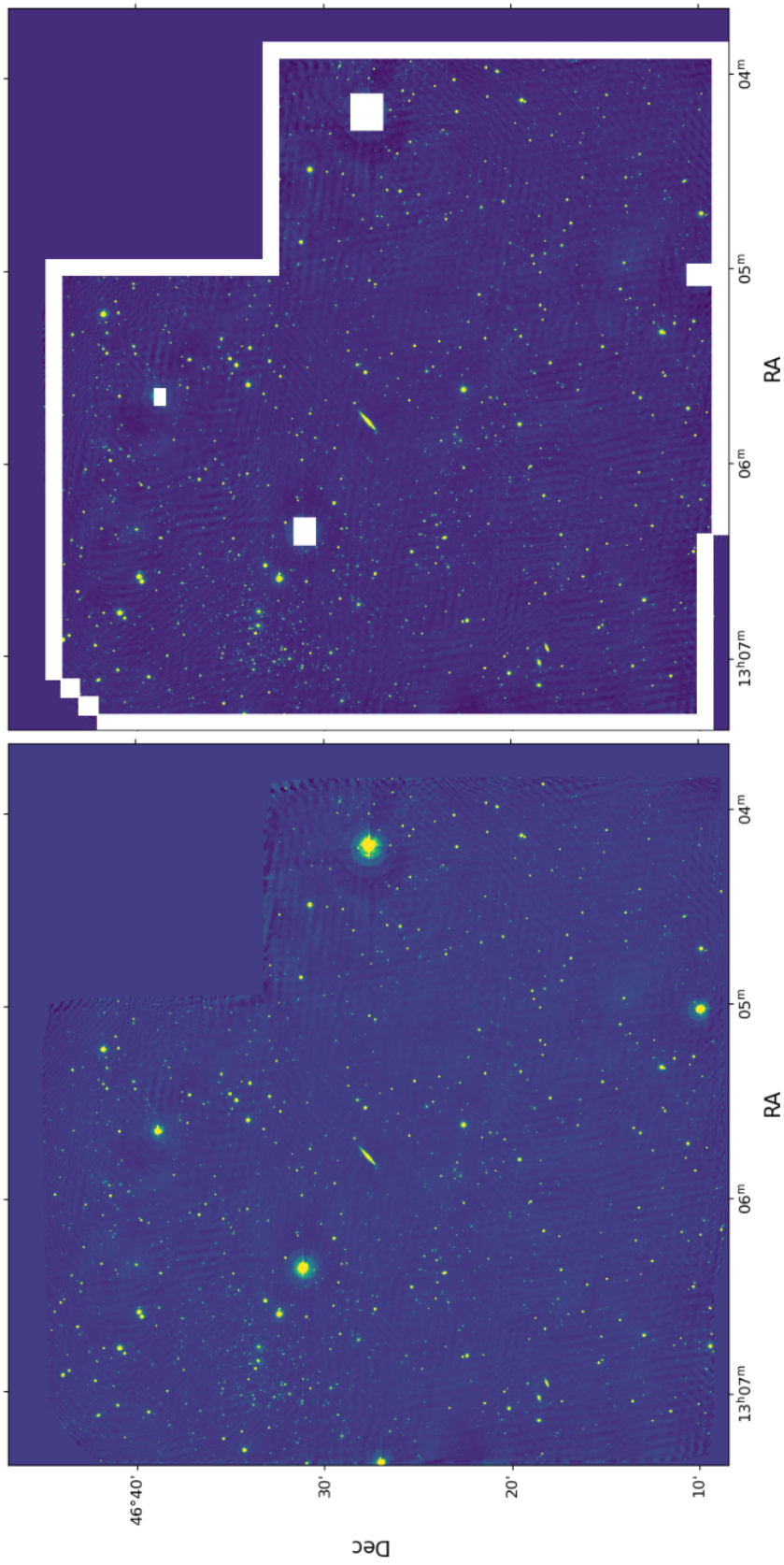

Figure 6.2: *left:* The co-added Hα image of the chosen pointing. *right:* The same image with the bright sources and noisy edges masked.

extraction process, before converting fluxes into AB magnitudes using

$$m_{AB} = -2.5 \log_{10} \left(\frac{f_\nu}{3631\text{Jy}} \right), \tag{6.1}$$

where f_ν is the spectral flux density in Jy. We are then able to analyse how the $i - \text{H}\alpha$ colour of each source varies with Hα in order to extract the primary Hα emitting sources from the sample, as shown in Figure 6.3. This process is done by calculating the standard deviation, σ, in magnitude windows of width 0.5 for all sources below $\text{BB} - \text{NB} = 0$. We then take a line of best fit for all 5σ values within these windows, which we reflect in the line $\text{BB} - \text{NB} = 0$ to give a lower boundary for classifying NB emitters. We take the NB emitter sample to be all sources with a colour value higher than this boundary, with an NB magnitude < 21.5.

The resulting sample from this method comprises 60 sources, which are then visually analysed to identify any potential contamination due to remaining ghosts from bright foreground stars, noise from the outer edges of the images, or double sources that are difficult to separate. With said contaminants removed, the sample consists of 39 NB emitters, which are shown in Figure 6.4. While Stroe & Sobral (2015) and Stroe et al. (2015) find the average number of Hα emitters to comprise $\sim 50\%$ of their NB emitter sample, we choose to refer to our entire sample of 39 sources as Hα emitters for the remainder of this work, accepting that any higher-redshift NB emitters within the sample will only serve to dilute any signals seen within our results.

6.2.4 Offset Calculation

To assess whether there is any evidence of the identified SFGs experiencing enhanced off-centre star-formation due to ram pressure, we must investigate the offset between each galaxy's position in the i-band and the relative location of its Hα emission. In order to calculate the offsets between the Hα emission and the i-band emission of the 39 identified sources, we take postage stamps which allow us to produce isophotal contours of each source in both Hα and i-band (see Figures 6.5a and 6.5b). Some of the selected sources are fainter or contain more noise, and so we visually select the appropriate number of isophotal levels for each source individually, as well as masking any bright spots in the corners that might

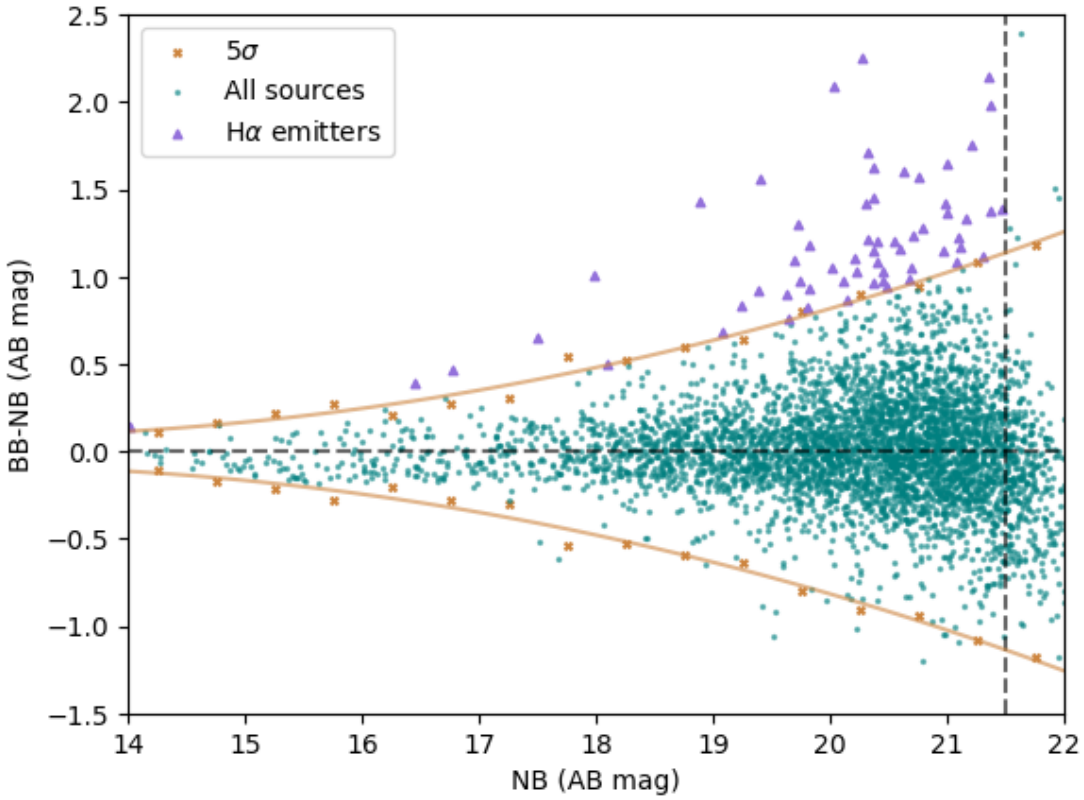

Figure 6.3: A colour–magnitude diagram displaying NB excess as function of NB magnitude, measured in AB mag. The bottom, orange curved line shows the best fit of the 5σ values (shown as orange crosses) taken from the source data below the horizontal, black dashed line showing BB − NB = 0. The top, orange curved line and points are a reflection in BB − NB = 0 of this 5σ boundary, and acts as the colour boundary we impose on classifying sources as Hα emitters, which are shown as purple triangles. The vertical black dashed line shows the upper magnitude boundary for classifying the Hα emitting sources.

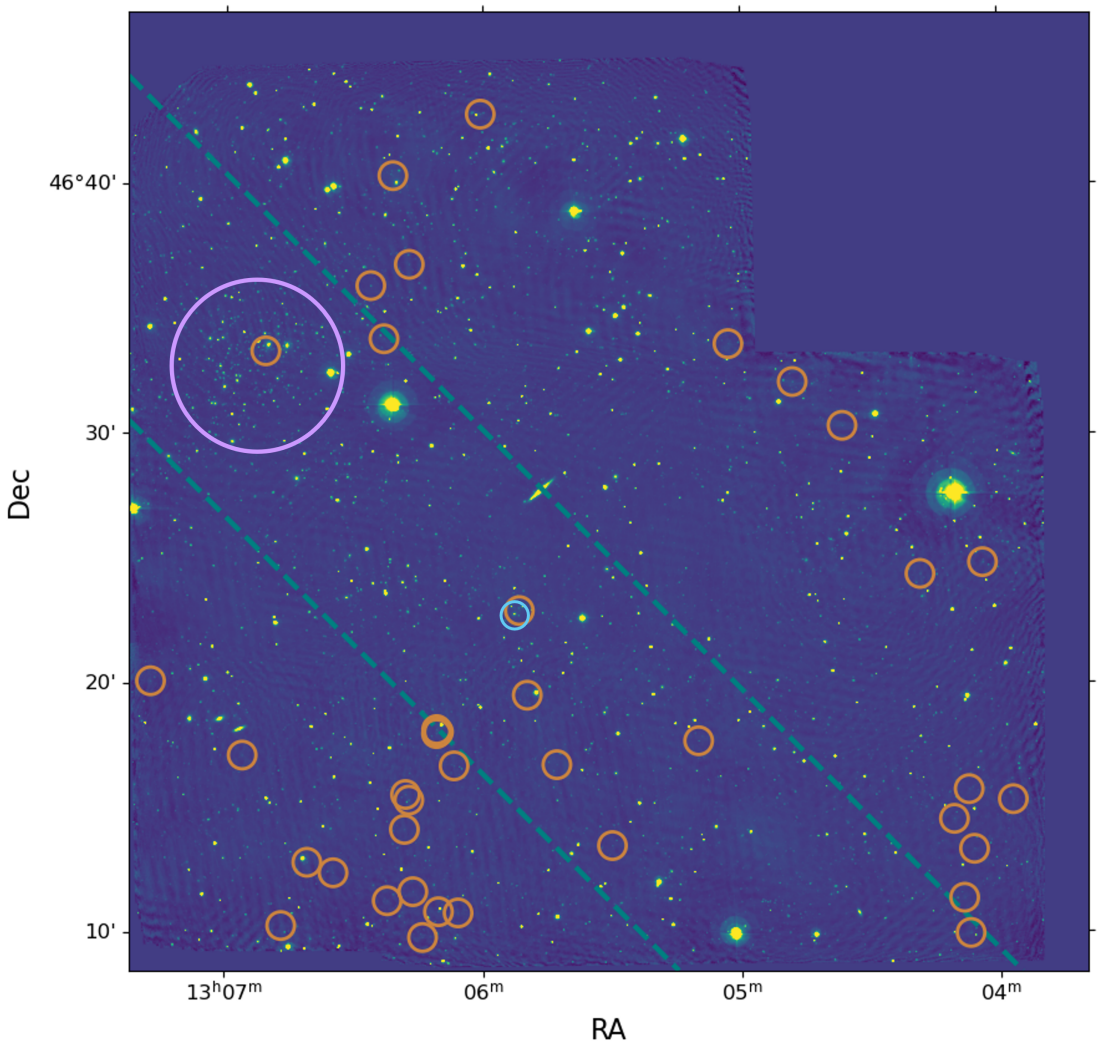

Figure 6.4: The locations (orange circles) of the Hα emitters in the FoV. The teal, dashed lines present a rough representation of where we would expect the filament containing the NAT ILTJ130552.58+462245.6 (small blue circle) to sit between Abell 1682 (large purple circle) in the upper left corner, and the other cluster identified by Wen & Han (2015) which is out of view.

affect the contour mapping.

If an SFG is experiencing enhanced star-formation on the leading edge of the galaxy caused by compression of cold, molecular gas due to ram pressure, we would expect to see a peak in Hα emission that is offset from the i-band in the direction of the cluster. However, if an SFG is in fact a jellyfish galaxy, we would expect to see extended, but not necessarily bright Hα emission caused by tails of enhanced star formation due to ram pressure stripping. Such emission might be offset from the i-band emission in the opposite direction to the cluster if the SFG is infalling. We therefore calculate the offsets in two ways: by taking the positional offsets between the centres of both the peak emission isophotes in each pair of postage stamps, and the outermost isophotes in each pair of postage stamps. As it is unclear which positional measurement is the best representation of the centre of the galaxy, we choose to compare like with like in order to maintain consistency.

Despite matching the world co-ordinate systems of both the Hα and i-band images, we find that there are systematic offsets present between the positions of sources in each band, which varies depending on the location of the source in the image. This systematic error might arise due to the stretching of the images in order to match the co-ordinate systems. We correct for this possible systematic bias by taking the 5 nearest neighbour sources of each of the 39 identified Hα emitters, calculating their vector pixel offsets between the i-band and Hα images in both the x and y axes, and taking the median of all five. This average vector pixel offset, which should contain any systematic offset in the adopted co-ordinates, is then subtracted from the offset between the i-band and Hα emission of the corresponding source. This systematic correction is shown in Figure 6.6.

After correction, the expected offset standard deviation, σ, between Hα and i-band emission is 0.084 pixels in the x-axis, and 0.071 pixels in the y-axis, resulting in a radial standard deviation of 0.078 pixels. Furthermore, to check that the angular distribution of the offsets is uniform, we perform a Rayleigh test of uniformity (Wilkie, 1983), which provides a p-value given the following hypotheses: H_0 (null hypothesis): The population is distributed uniformly around the circle, and H_1 (alternative hypothesis): The population is not distributed uniformly around the circle. The p-value for the uncorrected sources (teal in Figure 6.6), when measuring their angle counter-clockwise from North about the origin, is 1.30×10^{-25},

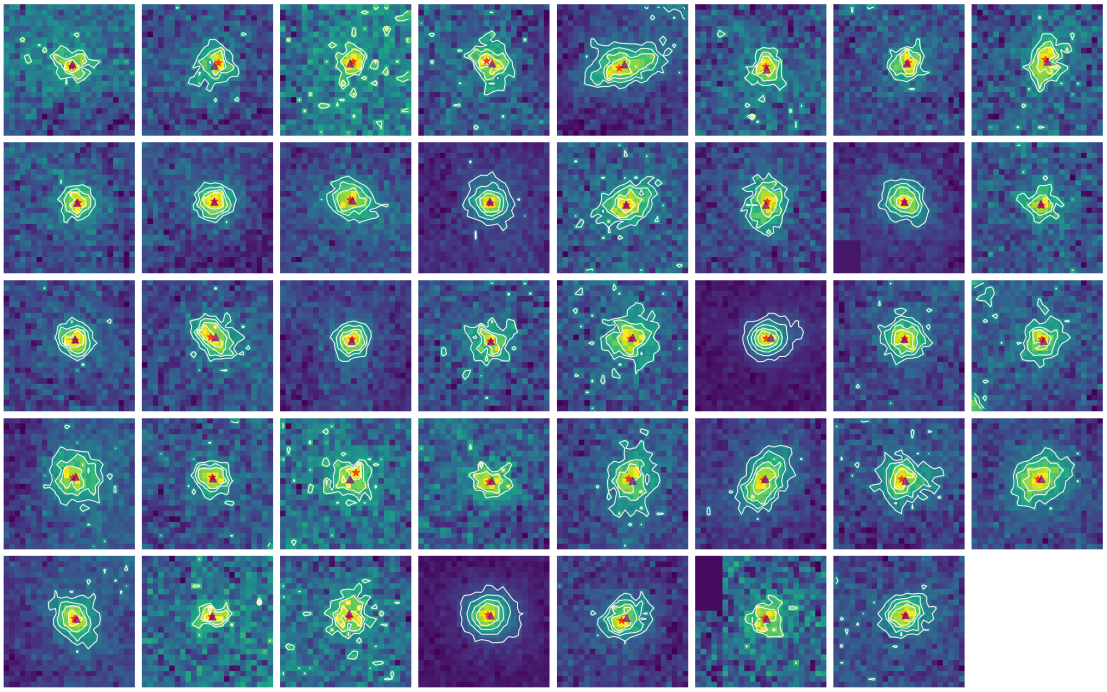

(a) Postage stamps of the 39 sources identified as Hα emitters, shown in Hα.

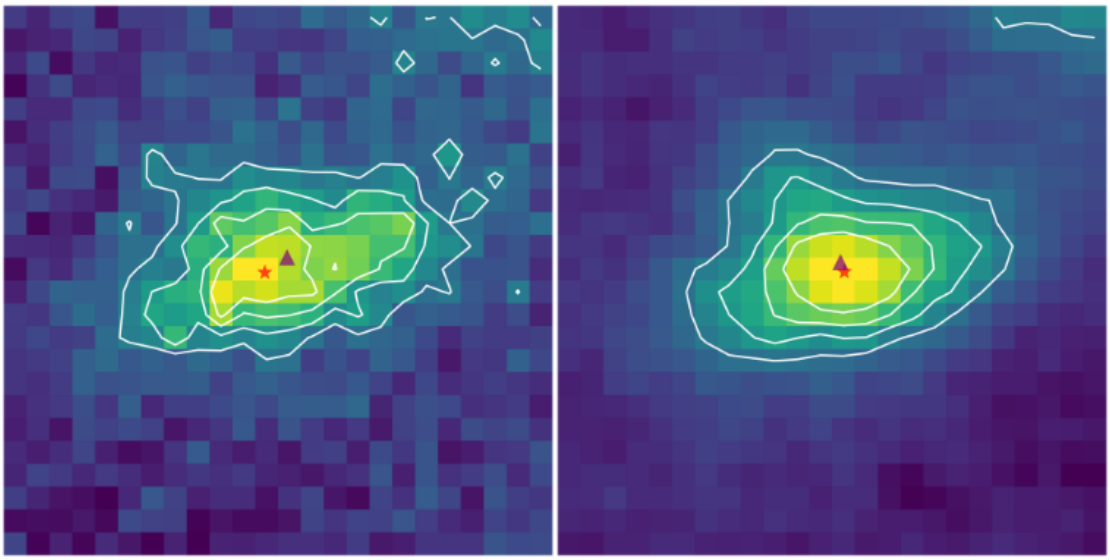

(b) An individual stamp of the same galaxy shown in both Hα (*left*) and i-band (*right*).

Figure 6.5: Postage stamps showing the isophotes, where the peak and outer isophote centres are represented by red stars and purple triangles respectively.

which is consistent with an extremely non-uniform distribution. After applying the described correction, the corrected sources (orange in Figure 6.6) have a p-value of 0.96, which is almost exactly consistent with a uniform distribution. Given these tests, we are satisfied that the corrections applied are adept at removing the systematic offsets.

After this systematic correction is applied to the sample of 39 Hα emitters, we are able to calculate the following: the pixel offset distance between the Hα and i-band emission, d_{ih}; the pixel offset distance between the cluster Abell 1682 at RA 13:06:49.70, Dec 46:32:58.92 and the centres of the i-band sources as defined by the segmentation process described in Section 6.2.3, d_{ci}; and the angle, θ, the definition of which is analogous to that presented in Chapter 5. Here, θ is the counter-clockwise angle between the vector from the cluster centre of Abell 1682 to the i-band isophote centre (be it the peak or outermost isophote, depending on the analysis), $\mathbf{R}_{ci}$, and the vector from this centroid to the corresponding Hα isophote centre, $\mathbf{R}_{ih}$. We present a diagram showing this setup in Figure 6.7 as visual assistance to the reader, which is very similar to that shown in Figure 5.1 in Chapter 5. The same mapping range of $-180^\circ < \theta < 180^\circ$ is also used, so that $|\theta| \sim 0^\circ$ describes Hα emission pointed away from the cluster centre, while $|\theta| \sim 180^\circ$ represents Hα emission on the same side as the cluster.

We present the analyses of the offsets and orientation angles of this sample in Section 6.3, where we search for signs of ram pressure effects.

6.3 Results & Discussion

We compare the pixel offset distance, d_{ih}, of each Hα – i-band pair with its associated cluster angle θ, and present these polar diagrams for the peak and outermost isophote centres in Figure 6.8.

Firstly, upon visual analysis of the *left* side of Figure 6.8, which displays the angular distribution of θ for the outermost isophote centres, we do not see any variation from a uniform distribution. The number of sources in each quadrant, starting from the uppermost quadrant and moving clockwise, is: 10, 15, 5 and 9. With 39 sources in total, one would expect to see ~ 10 sources in each quadrant

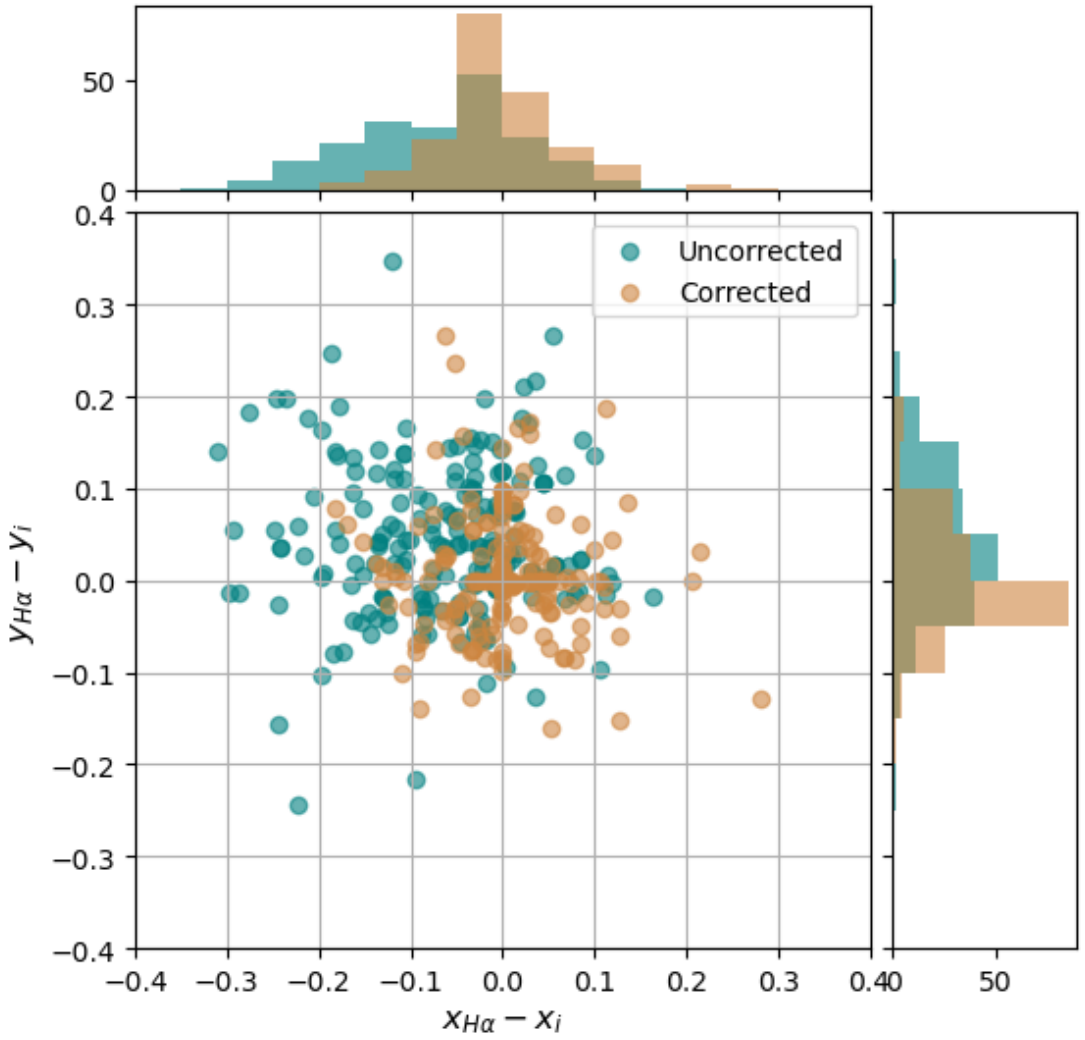

Figure 6.6: The scatter in the vector pixel offsets of the five nearest neighbours of the 39 sources in the sample. The uncorrected offsets and their distributions are shown in teal, with the corrected equivalents being shown in orange.

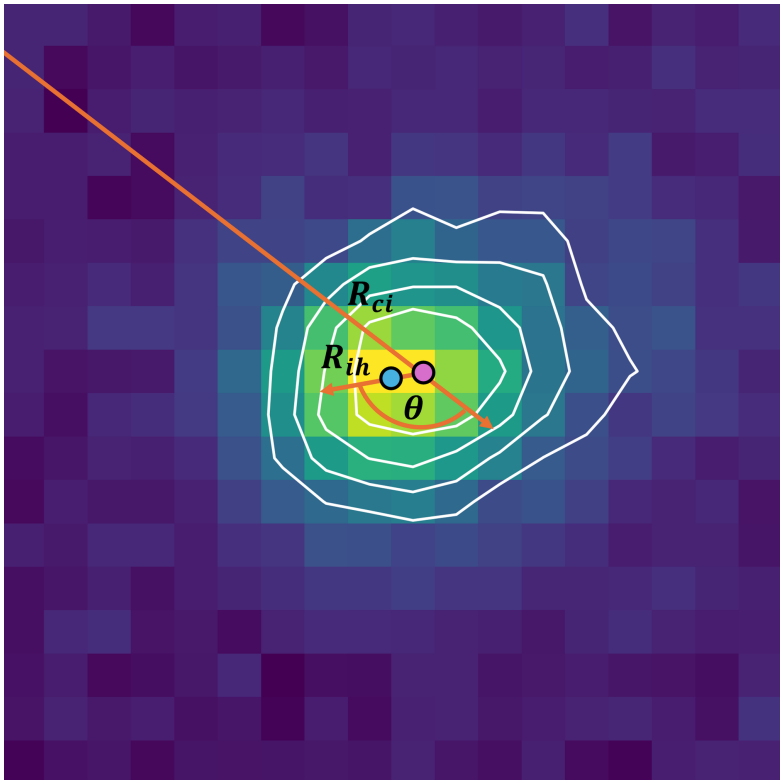

Figure 6.7: A stamp of one of the Hα sources in the sample, overlaid with white contours showing the isophotes from the i-band emission of the same source. The blue dot shows the Hα emission peak isophote centroid, and the pink dot shows the equivalent for the i-band emission. The vectors $\mathbf{R}_{ci}$, $\mathbf{R}_{ih}$, and the angle θ between them are all shown in orange.

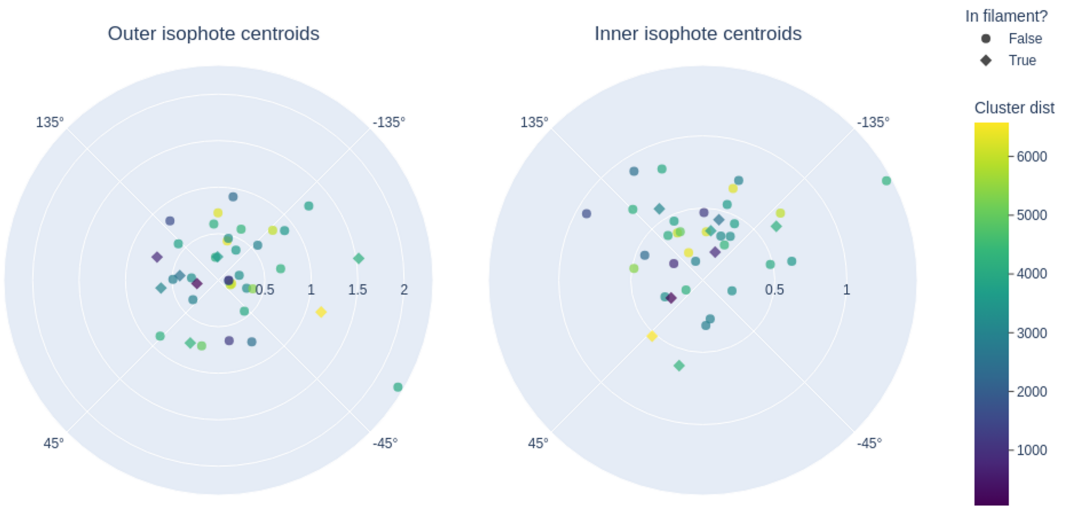

Figure 6.8: Polar diagrams representing the angle θ vs the pixel offset distance, d_{ih}, between the outer (*left*) or peak (*right*) isophote centres. The differently shaped markers represent whether the source lies between the expected filament boundaries given in Figure 6.4, and the colour of each point gives a measure of d_{ci}.

if the distribution was uniform. These numbers suggest that there is a small overdensity in the rightmost quadrant, and a small underdensity in the bottom quadrant. However, upon performing a Rayleigh test of this distribution, one finds a p-value of 0.13, which is not significant within a 95% confidence interval. Furthermore, we do not see any particular alignment with θ and distance from the cluster centre for either panel in Figure 6.8.

Upon inspection of the *right* side of Figure 6.8, it is immediately apparent that there is an overdensity of sources residing in the upper quadrant. This quadrant corresponds to sources with peak Hα emission on the leading edge of the galaxy, and contains 22 of the 39 sources, or 56.4% as opposed to the expected 25% if the sources were uniformly distributed. Again, moving clockwise from the upper quadrant, the remaining sections contain 6, 4 and 7 sources. This distribution generates a p-value of 1.17×10^{-4} with the Rayleigh test, which is significant to more than a 99.99% confidence level. This signal does not appear to be exclusive to "filament" sources, although it does account for 57% of the filament source population as well. Figure 6.8 suggests that sources all over the FOV have peak Hα emission directed towards the cluster centre, and we visually confirm this with Figure 6.9.

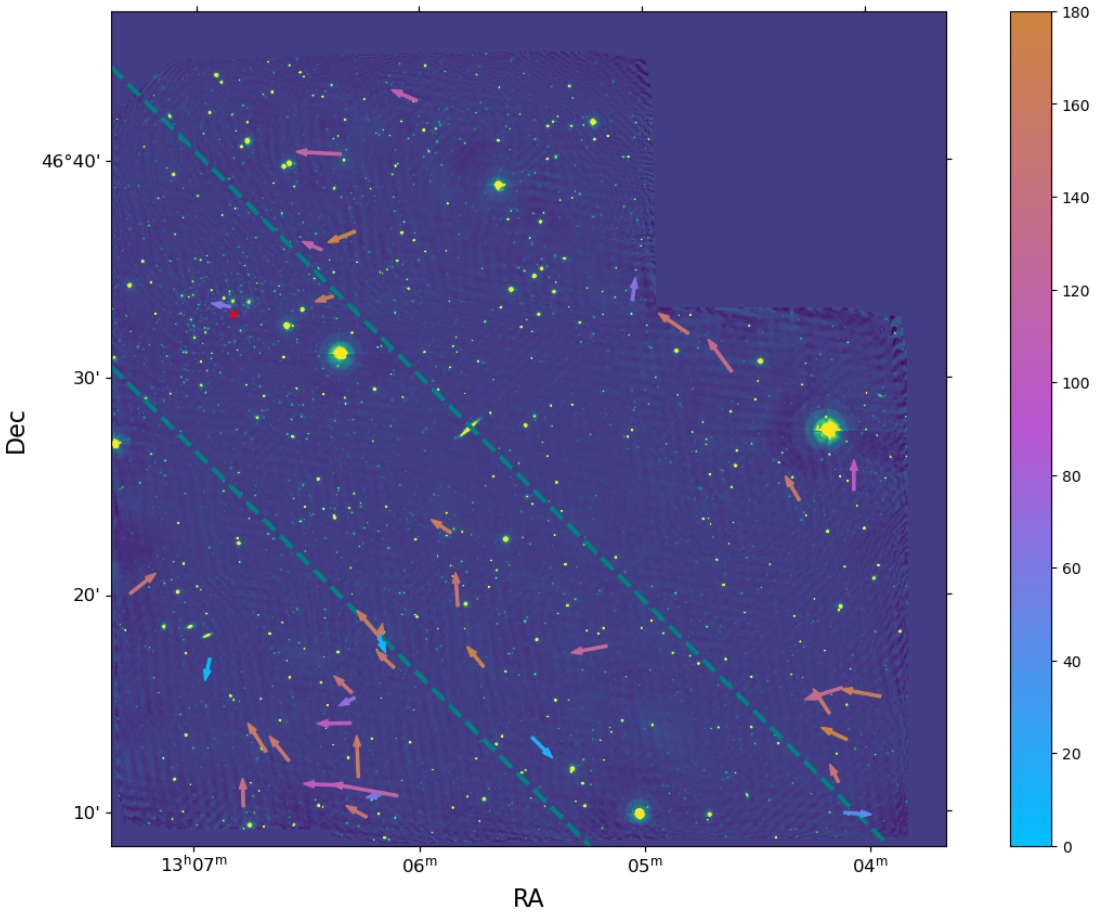

Figure 6.9: The Hα image of the FOV, superimposed with arrows representing the direction of the peak Hα emission with respect to the peak i-band emission for all 39 sources. The size of each arrow is 300$\times$ the size of d_{ih} in order to make the directional offsets more visible. The arrows are coloured with respect to $|\theta|$. The centre of cluster Abell 1682 is shown as a red cross, with the same rough filament boundaries shown as in Figure 6.4.

In Figure 6.9, we show the direction of the peak Hα emission with respect to the peak i-band emission for all 39 sources, and colour code each arrow with respect to $|\theta|$. It is evident from this image that a large fraction of these sources have peak Hα emission on the edge of the galaxy closest to the cluster, which could be an indicator of ram pressure compressing the molecular gas in this region and thus triggering enhanced star-formation. These tentative findings suggest that SFGs up to distances of 7.7Mpc away from Abell 1682 might have a velocity differential with the gas in their surroundings, be that ICM or IGM, thus producing the effects we see here. While we do not see evidence for such ram pressure in the angular distribution of the outer isophote centres (the *left* of Figure 6.8), which we assume would be synonymous with jellyfish galaxies, we postulate that perhaps any signal that might have been seen in this distribution has been diluted due to the potential inclusion of higher-redshift NB contaminants in the sample.

While these findings support the results seen in Chapter 5, they do not necessarily support our hypothesis, which was that enhanced ram pressure might be seen exclusively in filaments. Instead, we are seeing potential evidence of ram pressure in regions all around the cluster Abell 1682. While these intriguing results suggest that the gas density in the cluster outskirts might be denser than we think, or perhaps that the number of filaments feeding into Abell 1682 is very high even at great distances, we are hesitant to rely too heavily on these results due to the quality of the data. With higher resolution data, one might be able to visually identify enhanced star-formation in the same way that jellyfish galaxies like those in Poggianti et al. (2017a) are identified.

Chapter 7

Conclusions and Future Directions

Throughout this thesis, we have explored how the inner and outer cluster environments impact star-formation and nuclear activity in galaxies. In this final section, we summarise the findings from the previous chapters, and discuss the prospects of future directions.

7.1 Summary of Results

7.1.1 Local versus Global Environment: the Suppression of Star Formation in the Vicinity of Galaxy Clusters

In Chapter 3, we have shown that there is a clear decline in the SFG fraction with decreasing cluster-centric radius, beginning at a distance as far as $\sim 10R_{500}$ from the cluster centre. This finding uniquely extends the observable effects of environmental quenching to unprecedentedly large distances, revealing processes at play well beyond the virial radius that had not been systematically quantified before. We have interpreted this decline at large radii as the quenching of the SFG population prior to infall into a cluster, which we investigate by first binning the sample by stellar mass. We have found that both low-mass and high-mass SFGs still experience the same decline at large radii, with very little difference seen in the gradients of their decline. These results initially imply that all SFGs,

regardless of mass, experience the same rate of quenching outside of R_{500}.

We have also examined how the radial distribution is affected when binning the SFG sample by distance to nearest neighbour, which provides a measure of the local environment density. We have found that denser local environments appear to have a lower fraction of SFGs overall, although the galaxies within them experience less quenching of star-formation than galaxies in less-dense local environments, which appear to experience more quenching with cluster radius. This result paints the picture that SFGs in high-density local environments such as groups are shielded from global quenching mechanisms that would otherwise snuff out lone SFGs, but as a consequence have to pay the price of pre-processing upon joining the group, resulting in a lower SFG fraction in such environments overall.

Upon combining the binning of both mass and local environment density, we have found that the described local-environment shielding is actually much more pronounced for high-mass galaxies than low-mass ones, implying that high-density local environments are either not able to protect low-mass SFGs from global quenching mechanisms, or are in fact host to their own local quenching mechanisms which are more effective at ceasing star-formation in low mass SFGs than high mass ones.

7.1.2 From Outskirts to Core: the Suppression and Activation of Radio AGN around Galaxy Clusters

In Chapter 4, we have extended our study on the influence of the large-scale environment around clusters by presenting the distribution of the radio AGN fraction with respect to cluster-centric radius, and shown that the fraction lies either above or below the field fraction depending on the distance from the cluster centre. In the *outer* region, past $\sim 2R_{500}$, we see an increase of up to $\sim 25\%$ above the field fraction; in the *intermediate* region, between $10^{-0.75}R_{500} < r < 10^{0.25}R_{500}$, we see a decrease of $\sim 20\%$ relative to the field; and in the *inner* region, within $\sim 0.2R_{500}$, we see a huge spike in the cluster core corresponding to more than 3 times the field fraction. This comprehensive radial analysis provides a more detailed picture of AGN activity across cluster environments than previously reported, particularly the significant enhancement in the outer regions.

In an attempt to explain the variation in the AGN fraction from the field, we have investigated how both host galaxy stellar mass and radio luminosity vary in each of the three regions. We have found that there is very little difference between the stellar mass of the host galaxies in the *intermediate* and *outer* regions, with only the *inner* region displaying a larger fraction of high-mass hosts, likely due to resident BCGs. When analysing radio luminosity, we have found similarities between the AGN fraction and the radio luminosity distribution in each region: in the *inner* region the AGN fraction is at its peak, and these AGN also appear to be the most radio luminous; the *intermediate* region appears to hold the highest fraction of low luminosity AGN, and is also where the AGN fraction is at its lowest; finally, the *outer* region, which hosts the intermediate AGN fraction, also has the middling level of AGN radio luminosity.

We have postulated that the surge of excess AGN in the *outer* region is due to mergers permitted by the lower velocity dispersion, with the opposite being true in the *intermediate* region. The peak of radio AGN in the *inner* region is likely due to cooling flows or cool cores which are responsible for feeding the nuclear activity of BCGs. All of these scenarios are consistent with the radio luminosities seen in those regions. These results suggest that different environmental mechanisms, depending on the AGN's proximity to the nearest cluster, drive the observed effects, causing AGN to oscillate between active and inactive states independent of their host galaxy's stellar mass.

7.1.3 Clusters' Far-Reaching Influence on Narrow-Angle Tail Radio Galaxies

In Chapter 5, we have looked further at the interaction between AGN and their environment by developing a technique for determining the orbital direction of a NAT on the plane of the sky with respect to its host cluster, based on the orientation of its radio tails, which have been bent due to ram pressure. We have used this technique to show that NATs lie on primarily infalling orbits towards the cluster centre, out to the unusually large radius of $10R_{500}$, where one would not expect the ICM density to be high enough to induce ram pressure. Upon further analysis, we have also discovered that there is a small population of outbound

NATs close to the cluster centre, within $\sim 0.5R_{500}$.

In order to explain these results, we have suggested the following scenario: galaxies that will host NATs have their nuclear activity triggered via ram pressure whilst travelling down filaments towards clusters, thus producing jets which get bent into acute angles by the same ram pressure that induced them. These NATs fall into clusters, where they briefly retain their structure long enough to be identified as outbound NATs, before either becoming inactive as AGN or having their jet structure altered so that they are no longer identified as NATs. This work introduces a new framework for interpreting NAT orbits and provides valuable insight into the interplay between filamentary gas, AGN triggering, and jet morphology within cluster environments.

7.1.4 The Search for Evidence of Ram Pressure Outside Galaxy Clusters

Finally, in Chapter 6, we have sought to tie together the environmental impact on star-formation and AGN activity by investigating further into the results found in Chapter 5. We have looked for evidence of ram pressure on SFGs via enhanced Hα emission close to the NAT ILTJ130552.58+462245.6, which lies between the galaxy cluster Abell 1682 and a smaller cluster. After having identified 39 sources with Hα emission above 5σ significance, we have investigated the directional offsets of both their peak and outer isophote Hα emission centroids from their respective i-band centroids, with respect to the cluster Abell 1682.

Although we have seen no correlation in the outer isophote offsets, we have found that more than 50% of sources in the FOV have peak Hα emission directed towards Abell 1682, out to as far as $\sim 5R_{500}$, both inside and outside of the potential filament region between Abell 1682 and the other, smaller cluster. This result suggests that there could be mechanisms such as ram pressure inducing enhanced star-formation on the leading edge of SFGs as they fall towards clusters, in regions all around the outskirts of cluster Abell 1682. We do not wish to over-interpret these findings due to the low spatial resolution of the data, but we have still found that the results seen are statistically significant at more than a 99.99% confidence level.

7.2 Future Directions

7.2.1 Identification of Filaments and Groups

Throughout this thesis, we have found multiple threads of evidence that suggest that high-density local environments, such as groups and filaments, have a large impact on the star-formation and nuclear activity of galaxies. We attempt to quantify the density of these local environments with the use of nearest neighbour distances, but with a filament or group map of the areas surrounding the clusters in our sample, we would be able to compare effects seen in different environments more robustly.

Attempts have been made to identify filaments and groups around clusters (Kuchner et al., 2020, 2021; Cornwell et al., 2022, 2024), as well as correctly associate galaxies around clusters with their specific region in the cosmic web (Cornwell et al., 2023), but so far this work has been primarily done using simulations. We hope to see such techniques applied to large, observational data sets in the future, with a view to understanding the various quenching and triggering mechanisms native to specific cosmic web environments.

7.2.2 Identification of Gas Density

The density of the ICM in galaxy clusters is identifiable via X-ray emission due to Bremsstrahlung radiation, making it a key component in calculating the strength of ram pressure on galaxies moving through that cluster. In this thesis, we have postulated that ram pressure is the likely culprit for jet bending, AGN triggering, and enhanced star-formation on thr infalling galaxy edge at large distances from the cluster centre, and knowing the density of the gas in the local environments surrounding those sources would enable us to confirm or disprove that hypothesis.

Some observations of the gas in filaments close to large clusters have already been detected (Werner et al., 2008; Eckert et al., 2015), as well as observations of the intragroup medium (Mulchaey et al., 1996; O'Sullivan et al., 2017), but it remains very difficult to detect the WHIM and IGM with current X-ray instrumentation.

However, new X-ray instrumentation such as AXIS (Russell et al., 2024) are making the detection of the WHIM in filaments and the intragroup medium one of their primary goals, making this a viable future line of research.

7.2.3 Improved Resolution Data for Hα Emission Variation

Given the resolution of the observations taken in Chapter 6, we were able to identify the centroids of the peak and outer isophotes of the Hα emission of a sample of galaxies at redshift $z \sim 0.2$. However, the resolution of the INT was unfortunately not high enough to be able to quantify the detailed structure of the Hα emission in the SFGs in our sample, which would have given a much more robust indication of any areas of enhanced star-formation.

High resolution Hα imagery has already been obtained of much closer galaxies in the GAs Stripping Phenomena survey (GASP, Poggianti et al., 2017b; Jaffé et al., 2018; Ramatsoku et al., 2019), at redshifts of $z = 0.04 - -0.07$, using data from the Very Large Telescope. With the use of new, high-resolution optical telescopes such as the James Webb Space Telescope (JWST), similar high resolution Hα structures of SFGs at redshifts of $z \sim 0.2$ and higher are much more feasible, and provide scope to be able to explore in detail how mechanisms such as ram pressure might be affecting the star-formation of these galaxies on the outskirts of more distant clusters.

7.3 Outlook

The research presented in this thesis advances our understanding of the influence that environments exert on galaxy evolution. By exploring a diverse range of environments, from the dense cores of galaxy clusters to their distant outskirts, and the local environments that lie within them, this work highlights the intricate interplay of local and global factors that govern star-formation and nuclear activity. These findings underscore the pivotal role of environmental interactions in shaping galaxy properties, offering new insights into quenching and triggering mechanisms.

With upcoming surveys and advanced observational capabilities poised to enter the field of environmental galaxy evolution into a transformative new era, this work contributes to a crucial foundation that paves the way for exciting new discoveries. JWST, with its unprecedented resolution and sensitivity, promises to revolutionise our ability to study Hα emission in galaxies at intermediate redshifts, shedding light on localised star-formation enhancements driven by environmental processes such as ram pressure. Concurrently, next-generation X-ray observatories like Athena and AXIS aim to overcome current limitations in detecting diffuse gas in filaments and the IGM. These instruments will provide insights into the densities and distributions of the gas that governs environmental interactions, enabling more precise tests of hypotheses regarding quenching and triggering mechanisms of both SFGs and AGN.

Wide-field surveys, such as the Vera C. Rubin Observatory's Legacy Survey of Space and Time (LSST) and the Euclid mission, will also play a pivotal role by delivering detailed maps of the cosmic web. These surveys will enhance our understanding of how galaxies interact with their environments on large scales, facilitating studies that explore the detailed mechanisms and intricacies of the Baryon Cycle across diverse structures like filaments, groups, and cluster outskirts. The addition of the work in this thesis to the extensive current literature of the field, combined with the exciting new advancements yet to come, promise to deepen our understanding of the processes driving galaxy evolution within the dynamic context of the cosmic web, paving the way for a more comprehensive view of the universe.

Bibliography

Abadi, M. G., Moore, B., & Bower, R. G. 1999, MNRAS, 308, 947, doi: 10.1046/j.1365-8711.1999.02715.x

Abazajian, K. N., Adelman-McCarthy, J. K., Agüeros, M. A., et al. 2009, ApJS, 182, 543, doi: 10.1088/0067-0049/182/2/543

Ahumada, R., Allende Prieto, C., Almeida, A., et al. 2020, ApJS, 249, 3, doi: 10.3847/1538-4365/ab929e

Alam, S., Albareti, F. D., Allende Prieto, C., et al. 2015, ApJS, 219, 12, doi: 10.1088/0067-0049/219/1/12

Angulo, R. E., Lacey, C. G., Baugh, C. M., & Frenk, C. S. 2009, MNRAS, 399, 983, doi: 10.1111/j.1365-2966.2009.15333.x

Antognini, J., Bird, J., & Martini, P. 2012, ApJ, 756, 116, doi: 10.1088/0004-637X/756/2/116

Aragón-Calvo, M. A., van de Weygaert, R., & Jones, B. J. T. 2010, MNRAS, 408, 2163, doi: 10.1111/j.1365-2966.2010.17263.x

Arnold, V. I., Shandarin, S. F., & Zeldovich, I. B. 1982, Geophysical and Astrophysical Fluid Dynamics, 20, 111, doi: 10.1080/03091928208209001

Bahé, Y. M., McCarthy, I. G., Balogh, M. L., & Font, A. S. 2013, MNRAS, 430, 3017, doi: 10.1093/mnras/stt109

Baldwin, J. A., Phillips, M. M., & Terlevich, R. 1981, PASP, 93, 5, doi: 10.1086/130766

Balogh, M. L., Morris, S. L., Yee, H. K. C., Carlberg, R. G., & Ellingson, E. 1997, ApJ, 488, L75, doi: 10.1086/310927

Balogh, M. L., Navarro, J. F., & Morris, S. L. 2000, ApJ, 540, 113, doi: 10.1086/309323

Balogh, M. L., Schade, D., Morris, S. L., et al. 1998, ApJ, 504, L75, doi: 10.1086/311576

Banfield, J. K., Wong, O. I., Willett, K. W., et al. 2015, MNRAS, 453, 2326, doi: 10.1093/mnras/stv1688

Baxter, D. C., Cooper, M. C., Balogh, M. L., et al. 2022, MNRAS, 515, 5479, doi: 10.1093/mnras/stac2149

Beers, T. C., & Tonry, J. L. 1986, ApJ, 300, 557, doi: 10.1086/163833

Begelman, M. C., Rees, M. J., & Blandford, R. D. 1979, Nature, 279, 770, doi: 10.1038/279770a0

Benavides, J. A., Sales, L. V., & Abadi, M. G. 2020, MNRAS, 498, 3852, doi: 10.1093/mnras/staa2636

Benson, A. J., Bower, R. G., Frenk, C. S., et al. 2003, ApJ, 599, 38, doi: 10.1086/379160

Best, P. N., & Heckman, T. M. 2012, MNRAS, 421, 1569, doi: 10.1111/j.1365-2966.2012.20414.x

Best, P. N., Kauffmann, G., Heckman, T. M., et al. 2005a, MNRAS, 362, 25, doi: 10.1111/j.1365-2966.2005.09192.x

Best, P. N., Kauffmann, G., Heckman, T. M., & Ivezić, Ž. 2005b, MNRAS, 362, 9, doi: 10.1111/j.1365-2966.2005.09283.x

Best, P. N., von der Linden, A., Kauffmann, G., Heckman, T. M., & Kaiser, C. R. 2007, MNRAS, 379, 894, doi: 10.1111/j.1365-2966.2007.11937.x

Bianconi, M., Smith, G. P., Haines, C. P., et al. 2018, MNRAS, 473, L79, doi: 10.1093/mnrasl/slx167

Bond, J. R., Kofman, L., & Pogosyan, D. 1996, Nature, 380, 603, doi: 10.1038/380603a0

Boselli, A., Fossati, M., & Sun, M. 2022, A&ARv, 30, 3, doi: 10.1007/s00159-022-00140-3

Bowen, I. S. 1927, Nature, 120, 473, doi: 10.1038/120473a0

Bower, R. G., Benson, A. J., & Crain, R. A. 2012, MNRAS, 422, 2816, doi: 10.1111/j.1365-2966.2012.20516.x

Bradley, L., Sipőcz, B., Robitaille, T., et al. 2024, astropy/photutils: 1.13.0, 1.13.0, Zenodo, doi: 10.5281/zenodo.12585239

Brinchmann, J., Charlot, S., Heckman, T. M., et al. 2004, arXiv e-prints, astro, doi: 10.48550/arXiv.astro-ph/0406220

Bruno, L., Venturi, T., Dallacasa, D., et al. 2024, A&A, 690, A329, doi: 10.1051/0004-6361/202451515

Cautun, M., van de Weygaert, R., Jones, B. J. T., & Frenk, C. S. 2014, MNRAS, 441, 2923, doi: 10.1093/mnras/stu768

Chiaberge, M., Gilli, R., Lotz, J. M., & Norman, C. 2015, ApJ, 806, 147, doi: 10.1088/0004-637X/806/2/147

Choque-Challapa, N., Smith, R., Candlish, G., Peletier, R., & Shin, J. 2019, MNRAS, 490, 3654, doi: 10.1093/mnras/stz2829

Christensen, C. R., Davé, R., Governato, F., et al. 2016, ApJ, 824, 57, doi: 10.3847/0004-637X/824/1/57

Cluver, M. E., Jarrett, T. H., Hopkins, A. M., et al. 2014, ApJ, 782, 90, doi: 10.1088/0004-637X/782/2/90

Cohn, J. D. 2012, MNRAS, 419, 1017, doi: 10.1111/j.1365-2966.2011.19756.x

Combes, F. 2017, Frontiers in Astronomy and Space Sciences, 4, 10, doi: 10.3389/fspas.2017.00010

Condon, J. J. 1992, ARA&A, 30, 575, doi: 10.1146/annurev.aa.30.090192.003043

Cornwell, D. J., Aragón-Salamanca, A., Kuchner, U., et al. 2023, MNRAS, 524, 2148, doi: 10.1093/mnras/stad1949

Cornwell, D. J., Kuchner, U., Gray, M. E., et al. 2024, MNRAS, 527, 23, doi: 10.1093/mnras/stad3205

Cornwell, D. J., Kuchner, U., Aragón-Salamanca, A., et al. 2022, MNRAS, 517, 1678, doi: 10.1093/mnras/stac2777

Cortese, L., Catinella, B., & Smith, R. 2021, PASA, 38, e035, doi: 10.1017/pasa.2021.18

Cowie, L. L., & McKee, C. F. 1975, A&A, 43, 337

Cox, T. J., Jonsson, P., Somerville, R. S., Primack, J. R., & Dekel, A. 2008, MNRAS, 384, 386, doi: 10.1111/j.1365-2966.2007.12730.x

Davis, M., & Geller, M. J. 1976, ApJ, 208, 13, doi: 10.1086/154575

Dekel, A., & Silk, J. 1986, ApJ, 303, 39, doi: 10.1086/164050

Di Matteo, P., Combes, F., Melchior, A. L., & Semelin, B. 2007, A&A, 468, 61, doi: 10.1051/0004-6361:20066959

Dolag, K., Meneghetti, M., Moscardini, L., Rasia, E., & Bonaldi, A. 2006, MNRAS, 370, 656, doi: 10.1111/j.1365-2966.2006.10511.x

Donahue, M., & Voit, G. M. 2022, Phys. Rep., 973, 1, doi: 10.1016/j.physrep.2022.04.005

Dressler, A. 1980, ApJ, 236, 351, doi: 10.1086/157753

Dressler, A., & Gunn, J. E. 1983, ApJ, 270, 7, doi: 10.1086/161093

Duncan, K. J., Sabater, J., Röttgering, H. J. A., et al. 2019, A&A, 622, A3, doi: 10.1051/0004-6361/201833562

Ebeling, H., Stephenson, L. N., & Edge, A. C. 2014, ApJ, 781, L40, doi: 10.1088/2041-8205/781/2/L40

Eckert, D., Jauzac, M., Shan, H., et al. 2015, Nature, 528, 105, doi: 10.1038/nature16058

Ehlert, S., Allen, S. W., Brandt, W. N., et al. 2013, MNRAS, 428, 3509, doi: 10.1093/mnras/sts288

Ehlert, S., von der Linden, A., Allen, S. W., et al. 2014, MNRAS, 437, 1942, doi: 10.1093/mnras/stt2025

Ehlert, S., Allen, S. W., Brandt, W. N., et al. 2015, MNRAS, 446, 2709, doi: 10.1093/mnras/stu2091

Ellison, S. L., Patton, D. R., Mendel, J. T., & Scudder, J. M. 2011, MNRAS, 418, 2043, doi: 10.1111/j.1365-2966.2011.19624.x

Ellison, S. L., Patton, D. R., Simard, L., et al. 2010, MNRAS, 407, 1514, doi: 10.1111/j.1365-2966.2010.17076.x

Erben, T., Schirmer, M., Dietrich, J. P., et al. 2005, Astronomische Nachrichten, 326, 432, doi: 10.1002/asna.200510396

Fabian, A. C. 1999, MNRAS, 308, L39, doi: 10.1046/j.1365-8711.1999.03017.x

—. 2012, ARA&A, 50, 455, doi: 10.1146/annurev-astro-081811-125521

Farouki, R., & Shapiro, S. L. 1981, ApJ, 243, 32, doi: 10.1086/158563

Fassbender, R., Šuhada, R., & Nastasi, A. 2012, Advances in Astronomy, 2012, 138380, doi: 10.1155/2012/138380

Feretti, L., Giovannini, G., Klein, U., et al. 1998, A&A, 331, 475, doi: 10.48550/arXiv.astro-ph/9712041

Finoguenov, A., Briel, U. G., & Henry, J. P. 2003, A&A, 410, 777, doi: 10.1051/0004-6361:20031319

Fujita, Y. 2004, PASJ, 56, 29, doi: 10.1093/pasj/56.1.29

Gaibler, V., Khochfar, S., Krause, M., & Silk, J. 2012, MNRAS, 425, 438, doi: 10.1111/j.1365-2966.2012.21479.x

Garon, A. F., Rudnick, L., Wong, O. I., et al. 2019, AJ, 157, 126, doi: 10.3847/1538-3881/aaff62

Gavazzi, G., Cortese, L., Boselli, A., et al. 2003, ApJ, 597, 210, doi: 10.1086/378264

Gendron-Marsolais, M., Kraft, R. P., Bogdan, A., et al. 2017, ApJ, 848, 26, doi: 10.3847/1538-4357/aa8a6f

Gilmour, R., Best, P., & Almaini, O. 2009, MNRAS, 392, 1509, doi: 10.1111/j.1365-2966.2008.14161.x

Gonzalez, A. H., Sivanandam, S., Zabludoff, A. I., & Zaritsky, D. 2013, ApJ, 778, 14, doi: 10.1088/0004-637X/778/1/14

Gordon, Y. A., Pimbblet, K. A., Owers, M. S., et al. 2018, MNRAS, 475, 4223, doi: 10.1093/mnras/sty115

Gull, S. F., & Northover, K. J. E. 1973, Nature, 244, 80, doi: 10.1038/244080a0

Gunn, J. E., & Gott, J. Richard, I. 1972, ApJ, 176, 1, doi: 10.1086/151605

Gürkan, G., Hardcastle, M. J., Smith, D. J. B., et al. 2018, MNRAS, 475, 3010, doi: 10.1093/mnras/sty016

Haggar, R., Gray, M. E., Pearce, F. R., et al. 2020, MNRAS, 492, 6074, doi: 10.1093/mnras/staa273

Haggar, R., Kuchner, U., Gray, M. E., et al. 2023, MNRAS, 518, 1316, doi: 10.1093/mnras/stac2809

Haines, C. P., Pereira, M. J., Sanderson, A. J. R., et al. 2012, ApJ, 754, 97, doi: 10.1088/0004-637X/754/2/97

Haines, C. P., Pereira, M. J., Smith, G. P., et al. 2015, ApJ, 806, 101, doi: 10.1088/0004-637X/806/1/101

Haines, C. P., Finoguenov, A., Smith, G. P., et al. 2018, MNRAS, 477, 4931, doi: 10.1093/mnras/sty651

Hardcastle, M. J., Williams, W. L., Best, P. N., et al. 2019, A&A, 622, A12, doi: 10.1051/0004-6361/201833893

Hardcastle, M. J., Horton, M. A., Williams, W. L., et al. 2023, A&A, 678, A151, doi: 10.1051/0004-6361/202347333

Harrison, C. M., & Ramos Almeida, C. 2024, Galaxies, 12, 17, doi: 10.3390/galaxies12020017

Hashiguchi, A., Toba, Y., Ota, N., et al. 2023, PASJ, 75, 1246, doi: 10.1093/pasj/psad066

Heckman, T. M., & Best, P. N. 2014, ARA&A, 52, 589, doi: 10.1146/annurev-astro-081913-035722

Helsdon, S. F., & Ponman, T. J. 2000, MNRAS, 315, 356, doi: 10.1046/j.1365-8711.2000.03396.x

Herpich, F., Mateus, A., Stasińska, G., Cid Fernandes, R., & Vale Asari, N. 2016, MNRAS, 462, 1826, doi: 10.1093/mnras/stw1742

Hickox, R. C., Jones, C., Forman, W. R., et al. 2009, ApJ, 696, 891, doi: 10.1088/0004-637X/696/1/891

Ho, L. C., Filippenko, A. V., & Sargent, W. L. W. 1997, ApJS, 112, 315, doi: 10.1086/313041

Hopkins, P. F., Cox, T. J., Hernquist, L., et al. 2013, MNRAS, 430, 1901, doi: 10.1093/mnras/stt017

Hou, A., Parker, L. C., & Harris, W. E. 2014, MNRAS, 442, 406, doi: 10.1093/mnras/stu829

Hough, T., Cora, S. A., Haggar, R., et al. 2023, MNRAS, 518, 2398, doi: 10.1093/mnras/stac3209

Hubble, E. P. 1926, ApJ, 64, 321, doi: 10.1086/143018

Hurier, G., Adam, R., & Keshet, U. 2019, A&A, 622, A136, doi: 10.1051/0004-6361/201732468

Ishibashi, W., & Fabian, A. C. 2012, MNRAS, 427, 2998, doi: 10.1111/j.1365-2966.2012.22074.x

Jaffé, Y. L., Verheijen, M. A. W., Haines, C. P., et al. 2016, MNRAS, 461, 1202, doi: 10.1093/mnras/stw984

Jaffé, Y. L., Poggianti, B. M., Moretti, A., et al. 2018, MNRAS, 476, 4753, doi: 10.1093/mnras/sty500

Jäntschi, L., & Bolboacă, S. D. 2018, Mathematics, 6, doi: 10.3390/math6060088

Kauffmann, G., Heckman, T. M., & Best, P. N. 2008, MNRAS, 384, 953, doi: 10.1111/j.1365-2966.2007.12752.x

Kauffmann, G., White, S. D. M., Heckman, T. M., et al. 2004, MNRAS, 353, 713, doi: 10.1111/j.1365-2966.2004.08117.x

Kauffmann, G., Heckman, T. M., Tremonti, C., et al. 2003a, MNRAS, 346, 1055, doi: 10.1111/j.1365-2966.2003.07154.x

Kauffmann, G., Heckman, T. M., White, S. D. M., et al. 2003b, MNRAS, 341, 33, doi: 10.1046/j.1365-8711.2003.06291.x

Kennicutt, Robert C., J. 1998, ARA&A, 36, 189, doi: 10.1146/annurev.astro.36.1.189

Kesebonye, K. C., Hilton, M., Knowles, K., et al. 2023, MNRAS, 518, 3004, doi: 10.1093/mnras/stac3293

Kewley, L. J., Dopita, M. A., Sutherland, R. S., Heisler, C. A., & Trevena, J. 2001, ApJ, 556, 121, doi: 10.1086/321545

Kormendy, J., & Richstone, D. 1995, ARA&A, 33, 581, doi: 10.1146/annurev.aa.33.090195.003053

Koulouridis, E., & Bartalucci, I. 2019, A&A, 623, L10, doi: 10.1051/0004-6361/201935082

Koulouridis, E., Gkini, A., & Drigga, E. 2024, A&A, 684, A111, doi: 10.1051/0004-6361/202348212

Kuchner, U., Aragón-Salamanca, A., Pearce, F. R., et al. 2020, MNRAS, 494, 5473, doi: 10.1093/mnras/staa1083

Kuchner, U., Aragón-Salamanca, A., Rost, A., et al. 2021, MNRAS, 503, 2065, doi: 10.1093/mnras/stab567

Lacerna, I., Rodriguez, F., Montero-Dorta, A. D., et al. 2022, MNRAS, 513, 2271, doi: 10.1093/mnras/stac1020

Larson, R. B. 1974, MNRAS, 169, 229, doi: 10.1093/mnras/169.2.229

Larson, R. B., Tinsley, B. M., & Caldwell, C. N. 1980, ApJ, 237, 692, doi: 10.1086/157917

Lau, E. T., Kravtsov, A. V., & Nagai, D. 2009, ApJ, 705, 1129, doi: 10.1088/0004-637X/705/2/1129

Lewis, I., Balogh, M., De Propris, R., et al. 2002, MNRAS, 334, 673, doi: 10.1046/j.1365-8711.2002.05558.x

Lopes, P. A. A., Ribeiro, A. L. B., & Brambila, D. 2024, MNRAS, 527, L19, doi: 10.1093/mnrasl/slad134

Lovisari, L., Ettori, S., Gaspari, M., & Giles, P. A. 2021, Universe, 7, 139, doi: 10.3390/universe7050139

Lusetti, G., de Gasperin, F., Cuciti, V., et al. 2024, MNRAS, 528, 141, doi: 10.1093/mnras/stad3962

Mac Low, M.-M., & Ferrara, A. 1999, ApJ, 513, 142, doi: 10.1086/306832

Makino, J., & Hut, P. 1997, ApJ, 481, 83, doi: 10.1086/304013

Manzer, L. H., & De Robertis, M. M. 2014, ApJ, 788, 140, doi: 10.1088/0004-637X/788/2/140

Marshall, M. A., Shabala, S. S., Krause, M. G. H., et al. 2018, MNRAS, 474, 3615, doi: 10.1093/mnras/stx2996

Martizzi, D., Vogelsberger, M., Artale, M. C., et al. 2019, MNRAS, 486, 3766, doi: 10.1093/mnras/stz1106

McGee, S. L., Balogh, M. L., Bower, R. G., Font, A. S., & McCarthy, I. G. 2009, MNRAS, 400, 937, doi: 10.1111/j.1365-2966.2009.15507.x

McNamara, B. R., & Nulsen, P. E. J. 2007, ARA&A, 45, 117, doi: 10.1146/annurev.astro.45.051806.110625

Merritt, D. 1984, ApJ, 276, 26, doi: 10.1086/161590

Mihos, J. C., & Hernquist, L. 1994, ApJ, 431, L9, doi: 10.1086/187460

Mingo, B., Croston, J. H., Hardcastle, M. J., et al. 2019, MNRAS, 488, 2701, doi: 10.1093/mnras/stz1901

Mo, W., Gonzalez, A., Stern, D., et al. 2018, ApJ, 869, 131, doi: 10.3847/1538-4357/aaef83

Molnar, S. M., Hearn, N., Haiman, Z., et al. 2009, ApJ, 696, 1640, doi: 10.1088/0004-637X/696/2/1640

Moore, B., Katz, N., Lake, G., Dressler, A., & Oemler, A. 1996, Nature, 379, 613, doi: 10.1038/379613a0

Morganti, R. 2017, Frontiers in Astronomy and Space Sciences, 4, 42, doi: 10.3389/fspas.2017.00042

Mukhanov, V. F., & Chibisov, G. V. 1981, Soviet Journal of Experimental and Theoretical Physics Letters, 33, 532

Mulchaey, J. S., Davis, D. S., Mushotzky, R. F., & Burstein, D. 1996, ApJ, 456, 80, doi: 10.1086/176629

Murray, N., Quataert, E., & Thompson, T. A. 2005, ApJ, 618, 569, doi: 10.1086/426067

O'Dea, C. P. 1985, ApJ, 295, 80, doi: 10.1086/163351

O'Dea, C. P., Sarazin, C. L., & Owen, F. N. 1987, ApJ, 316, 113, doi: 10.1086/165183

Oemler, Augustus, J. 1974, ApJ, 194, 1, doi: 10.1086/153216

O'Neill, B. J., Jones, T. W., Nolting, C., & Mendygral, P. J. 2019a, ApJ, 887, 26, doi: 10.3847/1538-4357/ab4efa

—. 2019b, ApJ, 884, 12, doi: 10.3847/1538-4357/ab40b1

Oppenheimer, B. D., Babul, A., Bahé, Y., Butsky, I. S., & McCarthy, I. G. 2021, Universe, 7, 209, doi: 10.3390/universe7070209

Ostriker, J. P., & Hausman, M. A. 1977, ApJ, 217, L125, doi: 10.1086/182554

O'Sullivan, E., Ponman, T. J., Kolokythas, K., et al. 2017, MNRAS, 472, 1482, doi: 10.1093/mnras/stx2078

Park, C., Choi, Y.-Y., Vogeley, M. S., et al. 2007, ApJ, 658, 898, doi: 10.1086/511059

Peluso, G., Vulcani, B., Poggianti, B. M., et al. 2022, ApJ, 927, 130, doi: 10.3847/1538-4357/ac4225

Peng, Y.-j., Lilly, S. J., Kovač, K., et al. 2010, ApJ, 721, 193, doi: 10.1088/0004-637X/721/1/193

Penzias, A. A., & Wilson, R. W. 1965, ApJ, 142, 419, doi: 10.1086/148307

Péroux, C., & Howk, J. C. 2020, ARA&A, 58, 363, doi: 10.1146/annurev-astro-021820-120014

Pintos-Castro, I., Yee, H. K. C., Muzzin, A., Old, L., & Wilson, G. 2019, ApJ, 876, 40, doi: 10.3847/1538-4357/ab14ee

Poggianti, B. M., Smail, I., Dressler, A., et al. 1999, ApJ, 518, 576, doi: 10.1086/307322

Poggianti, B. M., Jaffé, Y. L., Moretti, A., et al. 2017a, Nature, 548, 304, doi: 10.1038/nature23462

Poggianti, B. M., Moretti, A., Gullieuszik, M., et al. 2017b, ApJ, 844, 48, doi: 10.3847/1538-4357/aa78ed

Postman, M., & Geller, M. J. 1984, ApJ, 281, 95, doi: 10.1086/162078

Ramatsoku, M., Serra, P., Poggianti, B. M., et al. 2019, MNRAS, 487, 4580, doi: 10.1093/mnras/stz1609

Reiprich, T. H., Basu, K., Ettori, S., et al. 2013, Space Sci. Rev., 177, 195, doi: 10.1007/s11214-013-9983-8

Ricarte, A., Tremmel, M., Natarajan, P., & Quinn, T. 2020, ApJ, 895, L8, doi: 10.3847/2041-8213/ab9022

Rihtaršič, G., Biffi, V., Fabjan, D., & Dolag, K. 2024, A&A, 683, A57, doi: 10.1051/0004-6361/202347444

Roberts, I. D., & Parker, L. C. 2017, MNRAS, 467, 3268, doi: 10.1093/mnras/stx317

Roberts, I. D., van Weeren, R. J., McGee, S. L., et al. 2021a, A&A, 652, A153, doi: 10.1051/0004-6361/202141118

—. 2021b, A&A, 650, A111, doi: 10.1051/0004-6361/202140784

Ruderman, J. T., & Ebeling, H. 2005, ApJ, 623, L81, doi: 10.1086/430131

Russell, H. R., Lopez, L. A., Allen, S. W., et al. 2024, Universe, 10, 273, doi: 10.3390/universe10070273

Sabater, J., Best, P. N., & Argudo-Fernández, M. 2013, MNRAS, 430, 638, doi: 10.1093/mnras/sts675

Sabater, J., Best, P. N., Hardcastle, M. J., et al. 2019, A&A, 622, A17, doi: 10.1051/0004-6361/201833883

Sakelliou, I., & Merrifield, M. R. 2000, MNRAS, 311, 649, doi: 10.1046/j.1365-8711.2000.03079.x

Salerno, J. M., Muriel, H., Coenda, V., et al. 2022, MNRAS, 517, 4515, doi: 10.1093/mnras/stac2980

Sandage, A., Freeman, K. C., & Stokes, N. R. 1970, ApJ, 160, 831, doi: 10.1086/150475

Schawinski, K., Thomas, D., Sarzi, M., et al. 2007, MNRAS, 382, 1415, doi: 10.1111/j.1365-2966.2007.12487.x

Schirmer, M. 2013a, ApJS, 209, 21, doi: 10.1088/0067-0049/209/2/21

—. 2013b, THELI GUI: Optical, near- & mid-infrared imaging data reduction, Astrophysics Source Code Library, record ascl:1308.013

Seyfert, C. K. 1943, ApJ, 97, 28, doi: 10.1086/144488

Shimwell, T. W., Röttgering, H. J. A., Best, P. N., et al. 2017, A&A, 598, A104, doi: 10.1051/0004-6361/201629313

Shimwell, T. W., Tasse, C., Hardcastle, M. J., et al. 2019, A&A, 622, A1, doi: 10.1051/0004-6361/201833559

Shimwell, T. W., Hardcastle, M. J., Tasse, C., et al. 2022, A&A, 659, A1, doi: 10.1051/0004-6361/202142484

Silk, J., & Rees, M. J. 1998, A&A, 331, L1, doi: 10.48550/arXiv.astro-ph/9801013

Silverman, J. D., Mainieri, V., Lehmer, B. D., et al. 2008, ApJ, 675, 1025, doi: 10.1086/527283

Smith, D. J. B., Haskell, P., Gürkan, G., et al. 2021, A&A, 648, A6, doi: 10.1051/0004-6361/202039343

Springel, V., Frenk, C. S., & White, S. D. M. 2006, Nature, 440, 1137, doi: 10.1038/nature04805

Stephens, M. A. 1974, Journal of the American Statistical Association, 69, 730, doi: 10.1080/01621459.1974.10480196

Stroe, A., & Sobral, D. 2015, MNRAS, 453, 242, doi: 10.1093/mnras/stv1555

Stroe, A., Sobral, D., Röttgering, H. J. A., & van Weeren, R. J. 2014, MNRAS, 438, 1377, doi: 10.1093/mnras/stt2286

Stroe, A., Sobral, D., Dawson, W., et al. 2015, MNRAS, 450, 646, doi: 10.1093/mnras/stu2519

Tanimura, H., Aghanim, N., Kolodzig, A., Douspis, M., & Malavasi, N. 2020, A&A, 643, L2, doi: 10.1051/0004-6361/202038521

Terni de Gregory, B., Feretti, L., Giovannini, G., et al. 2017, A&A, 608, A58, doi: 10.1051/0004-6361/201730878

Treister, E., Schawinski, K., Urry, C. M., & Simmons, B. D. 2012, ApJ, 758, L39, doi: 10.1088/2041-8205/758/2/L39

van Dokkum, P. G., Franx, M., Fabricant, D., Kelson, D. D., & Illingworth, G. D. 1999, ApJ, 520, L95, doi: 10.1086/312154

van Haarlem, M. P., Wise, M. W., Gunst, A. W., et al. 2013, A&A, 556, A2, doi: 10.1051/0004-6361/201220873

Von Der Linden, A., Best, P. N., Kauffmann, G., & White, S. D. M. 2007, MNRAS, 379, 867, doi: 10.1111/j.1365-2966.2007.11940.x

Walker, S., Simionescu, A., Nagai, D., et al. 2019, Space Sci. Rev., 215, 7, doi: 10.1007/s11214-018-0572-8

Wen, Z. L., & Han, J. L. 2015, ApJ, 807, 178, doi: 10.1088/0004-637X/807/2/178

Wen, Z. L., Han, J. L., & Liu, F. S. 2012, ApJS, 199, 34, doi: 10.1088/0067-0049/199/2/34

Werner, N., Finoguenov, A., Kaastra, J. S., et al. 2008, A&A, 482, L29, doi: 10.1051/0004-6361:200809599

Werner, S. V., Hatch, N., Muzzin, A., et al. 2021, in Galaxy Cluster Formation II, 20, doi: 10.5281/zenodo.4974454

Wetzel, A. R., Cohn, J. D., & White, M. 2009a, MNRAS, 395, 1376, doi: 10.1111/j.1365-2966.2009.14424.x

—. 2009b, MNRAS, 394, 2182, doi: 10.1111/j.1365-2966.2009.14488.x

Wetzel, A. R., Tinker, J. L., Conroy, C., & van den Bosch, F. C. 2013, MNRAS, 432, 336, doi: 10.1093/mnras/stt469

—. 2014, MNRAS, 439, 2687, doi: 10.1093/mnras/stu122

White, M., Cohn, J. D., & Smit, R. 2010, MNRAS, 408, 1818, doi: 10.1111/j.1365-2966.2010.17248.x

Wilkie, D. 1983, Journal of the Royal Statistical Society Series C: Applied Statistics, 32, 311

Williams, W. L., Hardcastle, M. J., Best, P. N., et al. 2019, A&A, 622, A2, doi: 10.1051/0004-6361/201833564

Wright, E. L., Eisenhardt, P. R. M., Mainzer, A. K., et al. 2010, AJ, 140, 1868, doi: 10.1088/0004-6256/140/6/1868

York, D. G., Adelman, J., Anderson, John E., J., et al. 2000, AJ, 120, 1579, doi: 10.1086/301513

Zabludoff, A. I., & Mulchaey, J. S. 1998, ApJ, 498, L5, doi: 10.1086/311312